On the Atomistic Simulation Approach Towards the Estimation of the Polymer/Solvent Mutual Diffusion Coefficient

by

Abolfazl Noorjahan

A thesis submitted in partial fulfillment of the requirements for the degree of

Doctor of Philosophy

in

Chemical Engineering

Department of Chemical and Materials Engineering

University of Alberta

Abstract

With increasing computational power, the multi scale simulation of materials is getting more possible. To show the ability of this method to address macro scale problems, in this work, the problem of polymer/solvent mutual diffusion was selected based on its scientific and industrial significance. Poly(vinyl alcohol) (PVA) was selected as the polymeric medium and water, ethanol and benzene as typical solvents. After careful formulation of the problem of mutual diffusion, the target variables were reduced to self diffusion coefficient of the solvent and Flory-Huggins interaction parameter of the binary system. Then, using extensive molecular dynamics simulations, the well-known OPLS-AA force field was validated for the simulation of PVA by benchmarking its predictions against a few of interesting parameters of pure PVA, namely the specific volume, glass transition temperature, Hildebrand solubility parameter and heat capacity. The results showed that the OPLS-AA force field was able to reproduce specific volumes, thermal expansion coefficients, glass transition temperatures and solubility parameters of the PVAs with different tacticities over a wide range of temperatures (200-550 K). For the heat capacities, 300% overestimations were obtained. Such overestimations were reduced significantly to about 30% by applying the quantum correction method.

It is well-known that properties of PVA in the pure and solution states depend largely on the hydrogen bonding networks formed. In the context of molecular simulation, such networks are handled through the Coulombic interactions. Therefore, a good set of partial atom charges (PACs) for simulations involving PVA is highly desirable. As the original PACs in OPLS-AA have been parameterized for small molecular species (ethanol), they need to be systematically validated for PVA macromolecule. Accordingly, the PACs for PVA were calculated using a few commonly used population analysis schemes with a hope to identify an accurate set of PACs for PVA monomers. To evaluate the quality of the calculated parameters, we have benchmarked their predictions for free energy of solvation (FES) in selected solvents by molecular dynamics simulations against the ab initio calculated val-

ues. Selected solvents were water, ethanol and benzene as they covered a range of size and polarity. The best candidate for PVA/solvent simulation was found to be PACs by Merz-Singh-Kollman which will serve future simulations for the prediction of the PVA/solvent Flory-Huggins interaction parameter.

In an attempt to provide more insight into the diffusion mechanism of solvents in PVA matrix, molecular dynamics simulation was used to study the diffusion of two selected penetrants, water and benzene, in PVA over a wide range of temperatures and concentrations. To help understand the effect of free volume on the diffusion behavior of water and benzene, we used the technique of Voronoi tessellation to determine key characteristics of free volume redistribution. In the case of water, we showed that it was the free volume redistribution frequency that led to an observation, previously reported in the literature, that the self-diffusion coefficient of water increases with increasing water concentration despite the fact that increase in water concentration decreases the mean fractional free volume in PVA. In the case of benzene (non-polar) diffusing in PVA (polar), we demonstrated that the failure of the Macki-Meares model was not entirely due to the dissimilarity between the intermolecular interactions. Rather, one of the reasons was the inability of the benzene molecules to break the hydrogen bonds between the PVA chains which are essential to increase the polymer segments mobility.

Based on the mechanism found, the free volume model was selected as the best candidate for describing the diffusion of small molecules in polymers. However, the experimental procedure for parameterizing the model is not trivial and in fact extremely time consuming. Accordingly, following the best practice in the literature, we carried out isobaric-isothermal molecular dynamics simulations to generate thermodynamic data of a few selected polymer/solvent systems and used the data to parameterize the corresponding Sanchez-Lacombe equation of state (SLEOS). The characteristic parameters of the SLEOS were then used in the parameterization of lattice free volume (LFV) model so that diffusivity of the solvents in the polymers were then calculated. Owing to its consideration of glass transition temperature effects, LFV model was more successful in correlation of the self diffusion data the Mackie-Meares model.

Preface

Chapter 5 of this thesis was published as **A. Noorjahan, and P. Choi**, "**Thermodynamic Properties of Poly(vinyl alcohol) with Different Tacticities Estimated from Molecular Dynamics Simulation**", *Polymer*, vol. 54(2013), 4212-4219. I was responsible for the data collection and analysis as well as the manuscript composition. Chapter 6 of this thesis has been accepted for publication as **A. Noorjahan, and P. Choi**, "**Effect of partial atomic charges on the calculated free energy of solvation of poly(vinyl alcohol) in selected solvents**", *Journal of Molecular Modeling*. I was responsible for the data collection and analysis as well as the manuscript composition. Chapter 7 of this thesis was published (In Press) as **A. Noorjahan, and P. Choi**, "**Effect of free volume redistribution on the diffusivity of water and benzene in poly(vinyl alcohol)**", *Chemical Engineering Science*. I was responsible for the data collection and analysis as well as the manuscript composition. Chapter 8 of this thesis has been accepted for publication as **A. Noorjahan, and P. Choi**, "**Prediction of self diffusion coefficients of selected solvents in poly(vinyl alcohol) using lattice-free volume theory**", *Polymer*. I was responsible for the data collection and analysis as well as the manuscript composition. Chapter 9 of this thesis was published as **A. Noorjahan, X. Tan, Q. Liu, M.R. Gray, and P. Choi**, "**Study of Cyclohexane Diffusion in Athabasca Asphaltenes**", *Energy&Fuels*, vol. 28, issue 2(2014), 1004-1011. I was responsible for the data collection and analysis as well as the manuscript composition. Dr. Xiaoli Tan assisted with the data collection and contributed to manuscript composition. Dr. Murry Gray assisted with the data collection and contributed to manuscript composition and edits. In all the aforementioned publications Dr. Phillip Choi contributed to manuscript composition and edits.

To my dear wife **Fatemeh**, for all her supports.

Acknowledgements

I would like to thank **Dr. Phillip Choi** who passionately helped me pursue what I had in mind and prepared a stress free environment to work in. I would also like to thank **Dr. Tian Tang** and **Dr. Murry R. Gray** for all those great things I learnt from them. Financial support from the **Advanced Foods and Materials Network** is gratefully acknowledged. I am also grateful for the financial support provided by the **Institute for Oil Sands Innovation (IOSI) at the University of Alberta**. This research has been enabled by the use of **WestGrid** computing resources, which are funded in part by the **Canada Foundation for Innovation**, **Alberta Innovation** and **Science, BC Advanced Education**, and the participating research institutions. WestGrid equipment is provided by IBM, Hewlett Packard and SGI.

Contents

List of Figures

List of Tables

Chapter 1

Motivation

There is no doubt that solving a problem without any simplification has been in great interest for scientists or engineers. Despite all the progress in science and computation power, solving any physical problem by the direct application of the Schrodinger's equation is still a fantasy due to numerous practical and theoretical issues (at least not till the quantum computer era). The most important prohibitive factor is the computational resources required for first principle calculation of any type. Accordingly, in the past couple decades, beside the continuum (macro) scale modeling, three different micro scale simulation methods have been emerged for addressing materials simulation (see figure 1.1): quantum mechanical approach with explicit consideration of the electrons, molecular dynamics with atomistic resolution and meso-scale modeling which groups a collection of atoms to speed up the calculations. The spacial resolution and time span of each simulation approach is limited with a wide gap between them. However, as the computational resources have become more available, the gap between these approaches is bridged effectively with multi-scale simulation approaches where output of one level of calculation is fed to upper level and so on. In this approach, one can benefit from high resolution of micro-scale modeling to parametrize a macro-scale model or compensate experimental weaknesses to gain better understanding of the problem in hand. Study of the polymeric materials and their behavior under different conditions is one of the most challenging problems which has been the center of many multi-scale simulation works during the past couple decades.

Polymeric materials have been known for quiet a long time and without doubt synthetic polymers play a major role in every aspect of everyday life. One of the most fundamental properties of these macromolecules is their tune-ability. A macromolecule with the same chemical formulation can exhibit a variety of properties, simply by changing the molecular weight of the chain, adding some branches to the back-bone or even subjected the polymer to a series of heating/cooling processes. It was this fact that opens windows to scientists to make new polymer-based materials with the desired properties. Every now and then, a claim of finding a new material with numerous medical, scientific or industrial applications

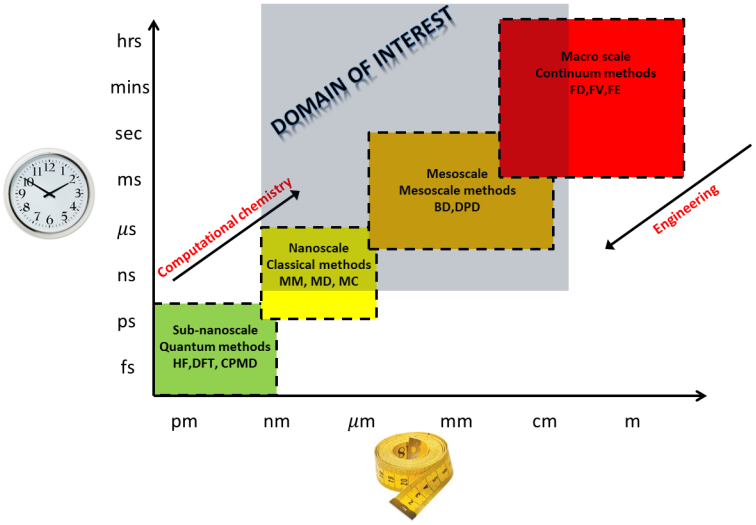

Figure 1.1: Time and length scale of material computer simulation.

is all over the news. But what we don't hear much about is the story of those costly and unsuccessful trials and errors in the lab prior to the great discovery. Is there anyway to guide those studies toward the final destiny with less pain? How about doing some computer simulation on the idea before putting it on the test in the lab? (see figure 1.2)

Far before availability of computers with enough computational power, theoretical modeling was the first choice to study materials. Theoretical models developed in that period are still great predictive tools. But every theory comes with its own weaknesses and simplifications. Theoretical modeling of the polymeric materials witnessed numerous successful but incomplete theories like entanglement and tube theory, free volume theory, lattice thermodynamic and etc. Despite the beauty and success rate of these models, their application for new materials is quiet a cumbersome task due to lack of required parameters. The synthesis of the polymer for experimental parametrization of the models is redundant, as in that case many required properties of the polymer could be measured directly. But how this gap can be filled in a timely and cost effective way? The answer is the "multi-scale computer simulation".

The art of computer simulation is in its early stage and still many more elaborations are required to make it practical for prediction of the properties of materials without any help from experimental data. In hope to put one step forward in this area and in this work we tried to apply multi-scale modeling approach to a polymer which has been studied experimentally and theoretically before. The main output of this work will be fine tunning of the contemporary methods of simulation and of the produced data. Beside that, results generated in this work will provide better understanding of the selected polymer with the

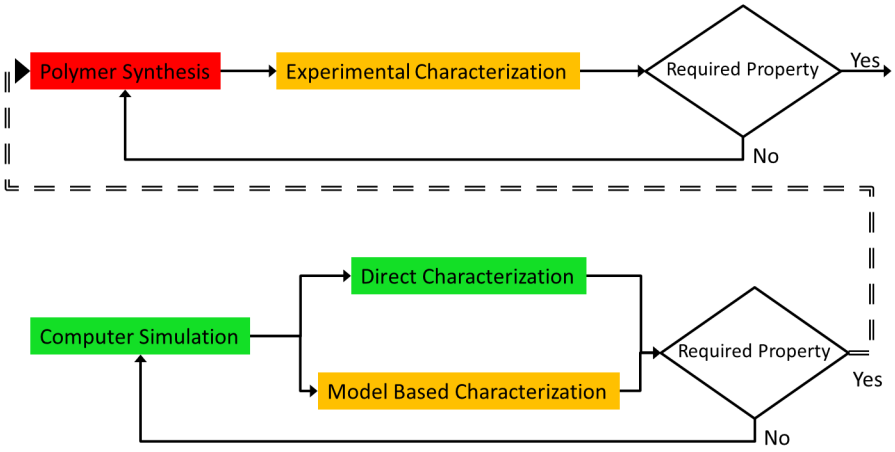

Figure 1.2: By providing prior information using computer simulation, number of times that costly experimental procedures repetition can be reduced largely.

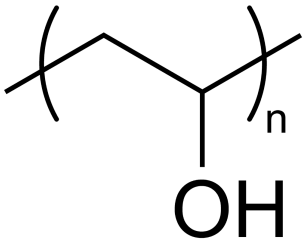

Figure 1.3: PVA repeating unit.

help of atomistic resolution of molecular dynamics.

Before rushing to any simulation, a proper choice for polymer under study is essential. The best candidate would be a polymer with available experimental data. Also, a specific problem should be chosen to work on with major scientific and industrial application. After a comprehensive review of the literature available, poly(vinyl alcohol) (PVA) was selected as the candidate polymer and mutual diffusion of the polymer/solvent as the problem of interest. The reason for such choices is explained in the next section.

1.1 Poly(vinyl alcohol)

For the case study, we have selected the poly(vinyl alcohol) (see figure 1.1 and 1.4) which has numerous applications in different fields of science and technology. Depending on the molecular weight and processing method, PVA shows numerous interesting properties like[2–4]:

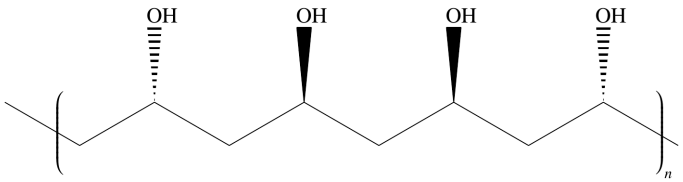

Figure 1.4: PVA monomer has a chiral center, so PVA has three possible stereoregular conformation namely: Atactic, Isotactic and Syndiotactic.

- Film-forming capability
- Gas barrier (due to small, dense and closely packed monoclinic crystallite)
- Highly hydrophilic
- Excellent chemical stability
- Non-toxic
- Non-carcinogenic
- Bio-adhesive
- Easy to process
- Low price (than other competitor polymers)
- Immiscibility with most organic compounds including hydrophilic solvents such as ethanol or acetic acid
- Flexible
- Transparent
- Toughness

based on above properties, PVA has been gradually used in a variety of applications such as [2–7]:

- Drug encapsulation and delivery
- Active membrane in pervaporation separation
- Barrier film for food packaging

- Contact lenses
- Composite materials
- Metal nano-particles stabilization
- Hydrogel in textile sizing and finishing agent
- Emulsifier
- Photosensitive coating
- Adhesives for paper, wood, textiles, leather
- Lining for artificial hearts

1.2 Polymer/solvent mutual diffusion

To optimize the performance of PVA in many of the aforementioned applications, a molecular level understanding of the diffusion behavior of low molecular weight substances, water in particular, in PVA is crucial. For example, in pervaporation separation (see figure 1.5) of solvent mixtures using PVA membrane the diffusion process governs the efficiency of separation [2]. In food packaging (see figure 1.6), the diffusion of water changes the film barrier properties and even a small amount of water is hesitated [7]. In drug delivery devices (see figure 1.7), release of drug is tuned by adjusting water uptake by PVA matrix or in contact lenses (see figure 1.8) the rate of oxygen diffusion (essential for eyes) is regulated by water content which is itself affected by diffusion rate of water in the matrix. Accordingly, prediction of mutual diffusion coefficient of PVA/solvent mixtures is highly desirable. So, having a powerful tool to predict the mutual diffusion coefficient of solvents in PVA is selected as major focus of this work.

1.3 Experimental validation of results

On the experimental side of the work, we were planing to use an Intelligent Mass Gravimetric Analyzer (IGA) for very accurate measurements of the mutual diffusion coefficient of solvent in PVA (for details see chapter 9). Although we were not able to start the planned experimental work, in the process of learning to use the IGA machine, we came a cross another industrial important problem as we were working on the asphaltenes materials from oil sands industry, very close to what would happen to PVA. These byproducts of oil-sands extraction are highly polar macromolecules resembling the situation we would face in the case of PVA. To show that how the experimental results on mass uptake/release could assist to derive the mutual diffusion coefficient of macromolecule/solvent system experimentally, at the very last chapter of this work we will present some of the published work in this area.

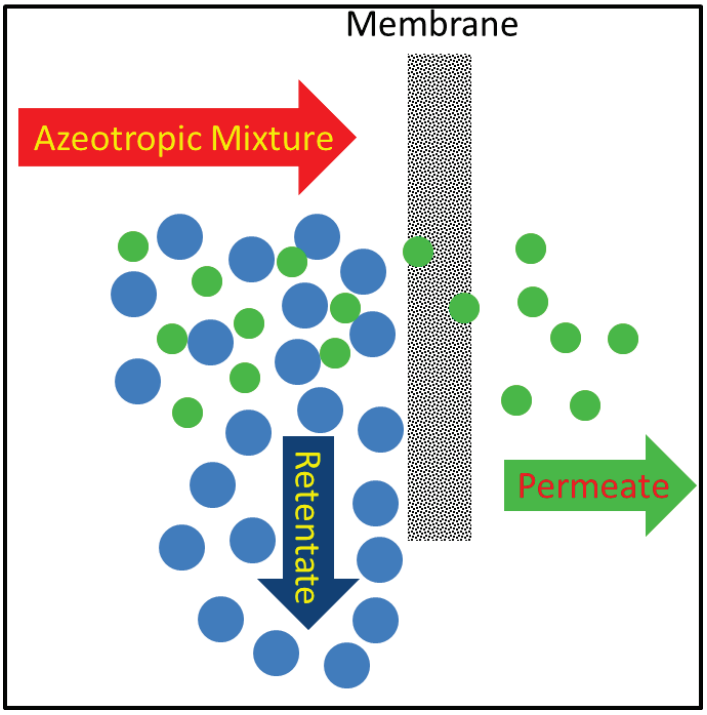

Figure 1.5: Schematic of pervaporation separation.

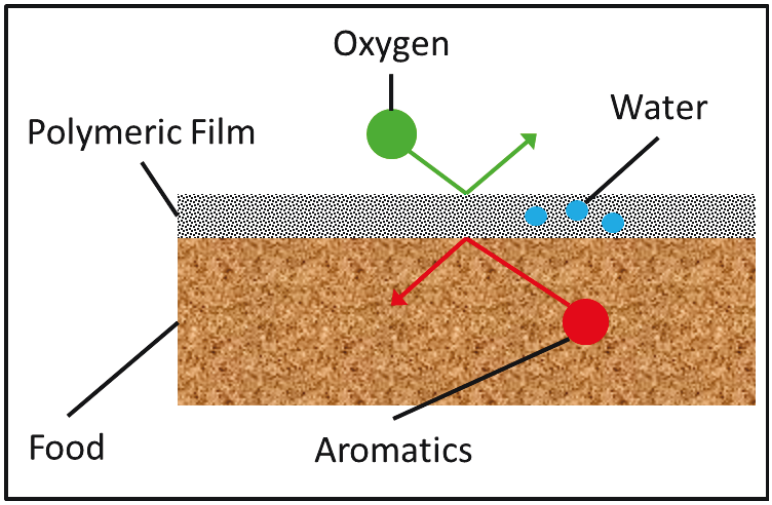

Figure 1.6: Schematic of polymer film around food.

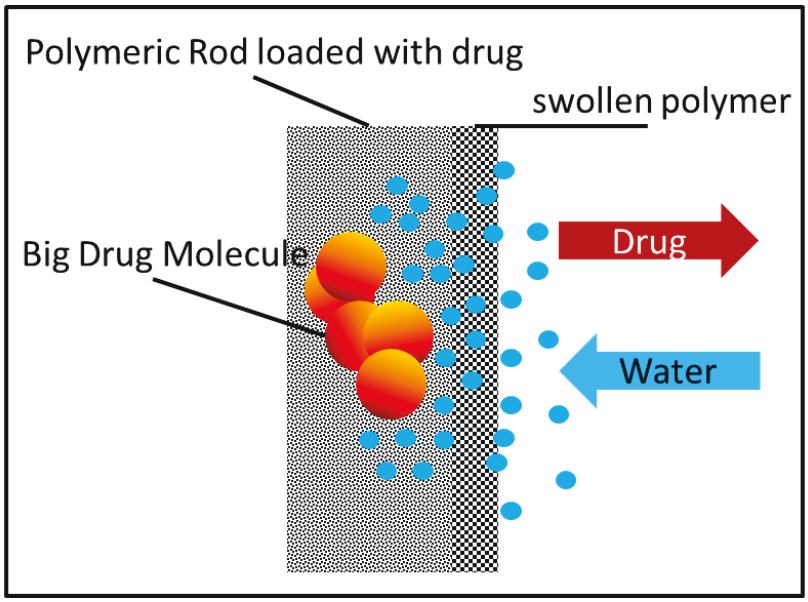

Figure 1.7: Schematic of a polymeric rod used for drug delivery.

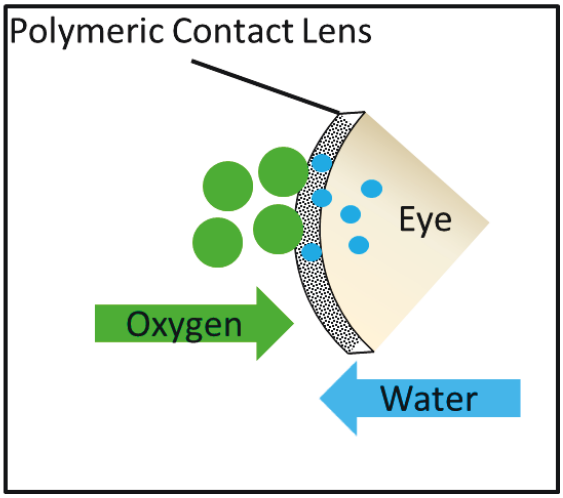

Figure 1.8: Schematic of contact lenses.

1.4 Objectives Summary

- Theoretical formulation of mutual diffusion in polymer/solvent systems.
- Validation of the MD force field for both pure PVA and PVA/solvent systems.
- Estimation of solvent self diffusion coefficients in PVA/solvent systems.
- Determination of the diffusion mechanism.
- Parametrization of the candidate models for the prediction of the solvent self diffusion coefficient.
- Estimation of the thermodynamic factor and mutual diffusion coefficients in PVA/solvent systems.
- Experimental evaluation of the mutual diffusion in PVA/solvent systems.
- Validation of the MD results by comparing with experimental data.

Chapter 2

Introduction

In this chapter, the problem of mutual diffusion of polymer/solvent systems will be mathematically formulated using the non-linear thermodynamic theory. Then, the problem is reduced to finding the key underlying parameters, self diffusion of solvent in polymer and the Flory-Huggins interaction parameter, using the Onsager analysis. The underlying theory for the calculation of each parameter will also be discussed. Finally, Voronoi tessellation will be presented as an efficient and simple method to characterize the free volume associated with molecules in systems of interest.

2.1 Theory of diffusion in polymers

2.1.1 Fick's formulation of diffusion

The concept of mass transfer had not been totally understood by 1850. Earlier in 1830's a chemist named Thomas Graham published several batches of data with regard to the rate of mass transfer and concentration but unfortunately without any attempt to mathematically model the phenomenon [8]. Later, in 1855, Adolf Fick, using these published data, made an analogy between mass transfer and heat conduction. He followed the Fourier heat conduction model and proposed his famous model for mass diffusion:

$$J = -D\nabla_x(C) \tag{2.1}$$

$$\nabla_t(C) = \nabla_x.(-J) \tag{2.2}$$

where t and x represent temporal and spatial coordinates, respectively. C is concentration and D is Fick's or mutual diffusion coefficient (For an explanatory discussion on differences between mutual and self diffusion coefficient see appendix A). While later on in 20 century, it was found that the true driving force for the mass transfer is chemical potential, these equations are still applicable in many practical problems with an acceptable accuracy.

2.1.2 Non-equilibrium thermodynamic formulation of diffusion

According to the general idea of non-equilibrium thermodynamics, each transport phenomenon can be considered as a transport driven by a driving force and a resistance opposing the transport (or transport coefficient). The idea behind this is based on the experimental observations of kinetics and is outside the scope of equilibrium thermodynamics. Empirically, the flux J is linearly proportional to the driving force f [9]:

$$J = L \times f \tag{2.3}$$

where L, the transport coefficient, is a proportionality constant (which can be scalar or tensorial depending on the system under consideration). As we discussed before, In the simplest case, it can be assumed that the driving force of diffusion is the concentration gradient and the coefficient L is the Fick's diffusion coefficient. Applying the postulates of non-equilibrium thermodynamics to the diffusion problem, it has been found [9] that the general form of molar diffusion flux in a non-equilibrium system (under mechanical equilibrium) for component i is:

$$J_i = -\sum_{i=1}^{N} L_{ij} \left(\nabla_T \mu_j - F_j \right) - \frac{L_{ij}}{T} \nabla T \tag{2.4}$$

where μ_j is the chemical potential of component j, F_j is the external force on component j, T is the temperature and N is the number of components. Now if we limit our analysis to binary mixtures in the thermal equilibrium without any external force acting on the system, Eq.2.4 reduces to:

$$J_i = -\sum_{i=1}^{2} L_{ij} \nabla_T \mu_j \tag{2.5}$$

and to evaluate this equation, the phenomenological coefficients L_{ij} and chemical potential of each component in the mixture are required.

2.1.3 Onsager analysis

Every molecular system has vacancy spaces between its molecules, space which is not occupied by molecules or atoms (see figure 2.1). As molecular species are moving in a mixture, these vacancies also move. Considering these vacancies, the flux of different chemical species in the system is given by:

$$\bar{J}_i = \sum_{j=1}^{N} L_{ij} \bar{X}_j + L_{iv} \bar{X}_v \tag{2.6}$$

where N is number of species in the system and v identifies the vacancy and L_{ij} are phenomenological Onsager coefficients. The generalized driving force for the flux of mass, $\bar{X}_j$, is generally given by Eq.2.4 and $\bar{X}_v$ is the chemical potential of the vacancies to be defined

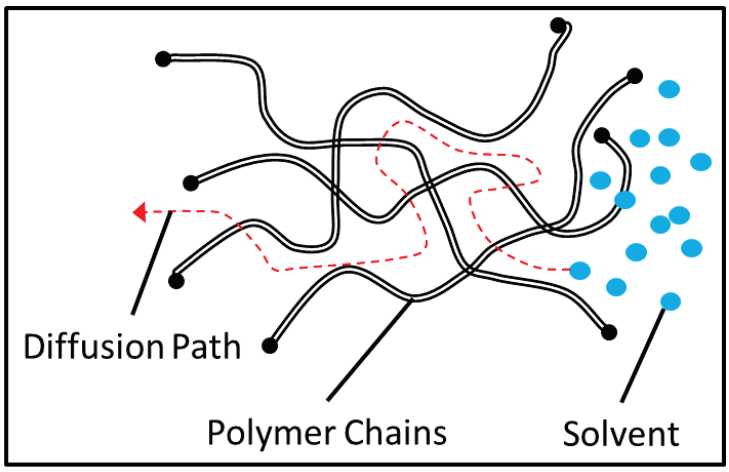

Figure 2.1: Representation of solvent molecules using the vacancies in the polymeric matrix to diffuse.

later. If the total volume of the system assumed to be constant, then the net flux in the system will be zero:

$$\sum_{i=1}^{N} \bar{J}_i + \bar{J}_v = 0 \tag{2.7}$$

This equation simply implies that the fluxes of different species are not independent. Using this equation, Onsager showed that the matrix of phenomenological coefficients L_{ij} obeys a simple rule which is known as Onsager reciprocal relations:

$$L_{ij} = L_{ji} \tag{2.8}$$

assuming that chemical potential of the vacancies is zero and using the Gibbs-Duhem relation, it can be shown that for a binary mixture of A and B:

$$J_A = \left(L_{AA} - L_{AB} \frac{x_A}{x_B} \right) \nabla \mu_A \tag{2.9}$$

Here, the definition the chemical potential is:

$$\mu_i = \mu_i^0 + kTln(\gamma_i x_i) \tag{2.10}$$

where x_i and γ_i are the mole fraction and activity coefficient of species i and μ_i^0 is the reference chemical potential. Accordingly, we have:

$$\nabla \mu_i = \frac{kT}{x_i} \nabla x_i + \frac{kT}{\gamma_i} \frac{\partial \gamma_i}{\partial x_i} \nabla x_i \tag{2.11}$$

Now, if we insert Eq.2.11 in Eq.2.9 and replace x_A with $\frac{C_A}{n}$ we have:

$$J_A = -D_A \nabla C_A \tag{2.12}$$

when D_A is mutual diffusion coefficient of A in B and is[10]:

$$D_A = \frac{kT}{n}\left(\frac{L_{AA}}{x_A} - \frac{L_{AB}}{x_B}\right)\left(1 + \frac{\partial ln\gamma_A}{\partial lnx_A}\right) \tag{2.13}$$

2.1.4 The Darken equation

Generally, the self diffusion coefficient can be considered as the Boltzmann factor (kT) times a constant. Accordingly, we can say (for detail you can see [11]):

$$D_{sA} = kT\left(\frac{L_{AA}}{C_A} + \frac{L_{BA}}{C_B}\right) \tag{2.14}$$

where D_{sA} is the self diffusion coefficient of A (in the density of mixture). So, the Eq.2.13 can be written as:

$$D_A = D_{sA}\left(1 + \frac{\partial ln\gamma_A}{\partial lnx_A}\right) \tag{2.15}$$

Using this definition, and applying the constraint in Eq. 2.6, Darken [10] related the mutual diffusion coefficient to self diffusion coefficient of components involved:

$$D = (x_B D_{sA} + x_A D_{sB})\left(1 + \frac{\partial ln\gamma}{\partial lnx}\right) \tag{2.16}$$

which was later extended to polymer mixtures and solutions by Hartley and Crank [12]. A close look at Eq. 2.16 reveals that for calculation of the mutual diffusion coefficient of a polymer/solvent system, there is a need to calculate the self diffusion coefficient of each of the components as well as a thermodynamic factor (or free energy). According to experimental results, it is well known that self diffusion of polymer segments (especially for high molecular weight chains) is negligible and only self diffusion of the solvents under study is required. So, in the upcoming section, we will review the theory required for the calculation and modeling of the solvent self diffusion and a thermodynamic model to predict the free energy of the system.

2.1.5 Flory-Huggins theory

The thermodynamics of polymer/solvent systems is well explained in the mean-field theory. The theory is an extension of the lattice fluid theory originally developed to explain the miscibility of two low molecular weight liquids. The simplest version of this lattice chain theory is generally referred to as the FloryHuggins mean-field theory. The mean-field theory for the polymer solutions compares the free energy of the polymer/solvent system before mixing and that after mixing. According to the Flory-Huggins theory, the Gibbs free energy of the mixture is:

$$\Delta G = nk_BT\left(\frac{\phi}{N_A} + \frac{1-\phi}{N_B}ln(1-\phi) + \phi(1-\phi)\chi\right) \tag{2.17}$$

Where n is total number of lattice sites, k_B is Boltzmann constant, ϕ is polymer volume fraction and χ is the Flory-Huggins interaction parameter. Using this equation, the mutual diffusion coefficient of solvent in a polymer solution can be obtained:

$$D_A = B_{AA}\phi\frac{\partial\mu_A}{\partial\phi} = kTB_{AA}\left(\frac{1-\phi}{N_A} + \frac{\phi}{N_B} - 2\chi\phi(1-\phi)\right) \tag{2.18}$$

where kTB_{AA} is the equivalent of the solvent self diffusion in the system:

$$D_{sA} = kTB_{AA} = \frac{kT}{N_A\eta} \tag{2.19}$$

where N_A and η are parameters related to the size of the solvent and viscosity of the system. Eq. 2.18 shows how the Flory-Huggins interaction parameter,χ, is the only parameter required to estimate the thermodynamic factor required to calculate the mutual diffusion coefficient.

2.1.6 The Free volume theory

According to the prediction of the transition state theory, the self diffusion of molecules in the liquid state is proportional to the inverse of the viscosity of the system. On the other hand, experimentally, it is known that viscosity of glass forming liquids undergoes a drastic change approaching its glass transition temperature. Accordingly, Cohen and Turnbull [13] proposed the free volume theory as an successor of the transition state theory to incorporate the glass transition effect on self diffusion of glass forming liquids:

$$D_s = ga^*u\exp\left(-\frac{\gamma\nu^*}{\nu_f}\right) \tag{2.20}$$

where g is a geometric factor; γ is a numerical factor introduced to correct for overlap of free volume; ν_f is average molecular free volume; ν^* is minimum required free volume for successful jump of diffusant; a^* approximately equals the molecular diameter; and u is gas kinetic velocity. Despite the initial belief, the greatest impact of this theory has been on describing mass transfer in concentrated polymeric solutions as well as simple liquids.

The formalism, as originally developed, provides a relationship between the system free volume and the self diffusion coefficient D_s for a one-component liquid. This relation can be readily be extended to describe the self diffusion of a single species in a binary mixture:

$$D_{s1} = D_{01}\exp\left(-\frac{\gamma\bar{\nu}_1^*}{\bar{\nu}_f}\right) \tag{2.21}$$

where D_{01} is the temperature-independent constant. Unlike the solution of hard sphere liquids, in the solution containing macromolecules, preparation of the enough volume for jump of the entire chain together is not possible. However, individual chain can be considered as multiple jumping units (polymer segments). Accordingly, Vrentas and Duda count number of jumping unit as follow:

$$\bar{\nu}_f = \frac{\hat{\nu}_f}{\frac{\omega_1}{M_1} + \frac{\omega_2}{M_2}} \tag{2.22}$$

where $\hat{\nu}_f$ is the specific hole free volume of a liquid with a weight fraction ω_i of species i, and with jumping unit molecular weights of M_i. Note that M_i for simple molecule is the entire molecular weight of the component but in the case of polymer chain is a small fraction of the total chain molecular weight. Accordingly, the solvent self diffusion in a polymer solution is given by:

$$D_{s1} = D_{01} \exp\left(-\frac{\gamma(\omega_1 \hat{\nu}_1^* + \omega_2 \xi \hat{\nu}_2^*)}{\hat{\nu}_f}\right) \tag{2.23}$$

where $\hat{\nu}_1^*$ is the specific hole free volume of component i required for a diffusive step and $\xi = \frac{\bar{\nu}_1^*}{\bar{\nu}_2^*}$. The most important parameter in the above equation is the free volume, $\hat{\nu}_f$, which should be defined for polymer solutions. Vrentas and Duda defined this parameter as follows:

$$\hat{\nu}_f = \omega_1 K_{11}(K_{21} - T_{g1} + T) + \omega_2 K_{12}(K_{22} - T_{g2} + T) \tag{2.24}$$

For polymer solutions, K_{11} and K_{21} are free volume parameters for the solvent, while K_{12} and K_{22} are free volume parameters for the polymer. T_{gi} and $_i$ are glass transition temperature and mass fraction of each component.

2.1.7 Statistical mechanics of self diffusion

The very basic equation used in the calculation of the self-diffusion coefficient of particles in molecular dynamics simulation is the so called "Einstein" equation. Since the first attempt by Einstein, there has been several other approaches by others which make the theory more elaborate. Beside the original argument and the approach by Smoluchowski (for details see [14]) which suffers from several unjustified assumptions, there is the proof by Paul Langevin which is much simpler and complete. Here, a brief summary of the theory is given (for more complete discussion see [15]).

Let us consider the motion of a Brownian particle in fluid. On average, the motion is governed by the Newtonian dynamics under friction, $m\dot{v} = -\gamma v$, where γ is the friction coefficient. However, this equation, leading to the continuous decay of the particle's velocity, holds only on the average. In order to describe the erratic motion of the particle, resulting from random, uncompensated impacts of the molecules of surrounding fluid, we have to introduce additional, fluctuating force $\xi(t)$. We assume only that this force has a zero mean (so that it does not lead to the net motion on average), and that it is independent on x, which reflects the homogeneity of the whole system. This results in the following equation:

$$m\dot{v} = -\gamma v + \xi(t) \tag{2.25}$$

The first task will be to find the mean square displacement of the particle. Let us now multiply both sides of the above equation by $x(t)$ and use the evident fact that $x\dot{v} = x\ddot{x} = \frac{d}{dt}(x\dot{x}) - \dot{x}^2$. So:

$$m\frac{d}{dt}(x\dot{x}) = m\dot{x}^2 - \gamma x\dot{x} + x\xi \tag{2.26}$$

By averaging this equation over the realization of the process and dividing both parts of the equation by m:

$$\frac{d}{dt}\langle x\dot{x}\rangle = \langle \dot{x}^2\rangle - \frac{\gamma}{m}\langle x\dot{x}\rangle + \frac{1}{m}\langle x\xi\rangle \tag{2.27}$$

The last mean value vanishes due to the (assumed) independence of x and ξ and due to the fact that the mean value of ξ is zero. Moreover, by use of the equipartition theorem, the mean squared velocity of the particle in our one-dimensional model fulfills the relation $\frac{m\dot{x}^2}{2} = \frac{k_B T}{2}$. Therefore,

$$\langle \dot{x}^2\rangle = \frac{k_B T}{m} \tag{2.28}$$

Accordingly,

$$\frac{d}{dt}\langle x\dot{x}\rangle = -\frac{\gamma}{m}\langle x\dot{x}\rangle + \frac{k_B T}{m} \tag{2.29}$$

Assuming that the initial particle's position is taken to be at the origin of coordinates, we have $\langle x(0)\dot{x}(0)\rangle = 0$. Under this initial condition, Eq. 2.29 can be easily solved and yields:

$$\langle x(t)\dot{x}(t)\rangle = \frac{k_B T}{\gamma}\left[1 - e^{(-\frac{\gamma}{m}t)}\right] \tag{2.30}$$

Considering that $\langle x(t)\dot{x}(t)\rangle = \frac{1}{2}\frac{d}{dt}\langle x^2(t)\rangle$, the mean square displacement of the particle can be found by an additional integration of above Eq 2.30:

$$\langle x^2(t)\rangle = 2\frac{k_B T}{\gamma}\left[t - \frac{m}{\gamma}\left(1 - e^{(-\frac{\gamma}{m}t)}\right)\right] \tag{2.31}$$

and for large time the leading term corresponds to:

$$\langle x^2(t)\rangle = 2\frac{k_B T}{\gamma}t = 2tD_{Einstein} \tag{2.32}$$

which simply indicates that self-diffusion coefficient of the Brownian particle is equal to one half of its mean square displacement (in 3 dimensional space, the coefficient is 6 rather than 2). But, as usually the particles in short time scale shows ballistic motions and in some cases due to the cage effect, a plateau in mean square displacement appears. In practice, the slope of the linear part of the mean square displacement versus time plot is used for the evaluation of the self diffusion coefficient.

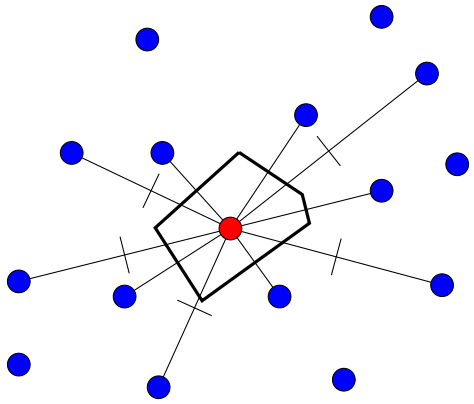

Figure 2.2: 2 dimensional representation of the normal Voronoi tessellation. Note to the bisector lines which are not in the Voronoi cell due to long distance. In 3 dimension the lines will be replaced by planes and eventual Voronoi cell is a polyhedron rather than polygon.

2.1.8 Voronoi tessellation

Considering a set of centroid points in space, Voronoi tessellation at its very basic form divides the space in a way that each point is enclosed in a potion of space. Each enclosing portion or region, called a Voronoi cell, is a polyhedron, which can be considered the influence zone of the point around which the cell is drawn. If there is an atom at that point, the volume of its Voronoi cell is the volume available to the atom. Voronoi tessellation has so many specific applications in computational chemistry like[16]: computation of atom and residue volumes, modeling of protein packing, computation of empirical potentials, study of voids and cavities, molecular dynamics and other novel applications.

A Voronoi cell is the region of space comprising points that are closer to the centroid (atoms) of the cell than to any other centroid. The cell is built by constructing the planes bisecting the lines drawn from the centroid to each of the other centroids (for a 2 dimensional representation see figure 2.2) and selecting the smallest polyhedron formed by these planes.

While the normal Voronoi tessellation works fine for the size-less or same-size points (atoms), for systems with diverse size, the allocation based on bisectors is not enough. To address this problem, Richards [17] proposed to introduce weights when drawing the planes of the Voronoi construction based on the atom size. This method, denoted as Richards' method B, has been widely used in the literature. But unfortunately, it lacks mathematical exactness, with some volume being lost between cells, as the dividing planes no longer intersect at common points (see figure 2.3).

To resolve this problem, this approach was refined by Gellatly and Finney [18] where they defined a rigorous weighted Voronoi construct in which radical planes are used to

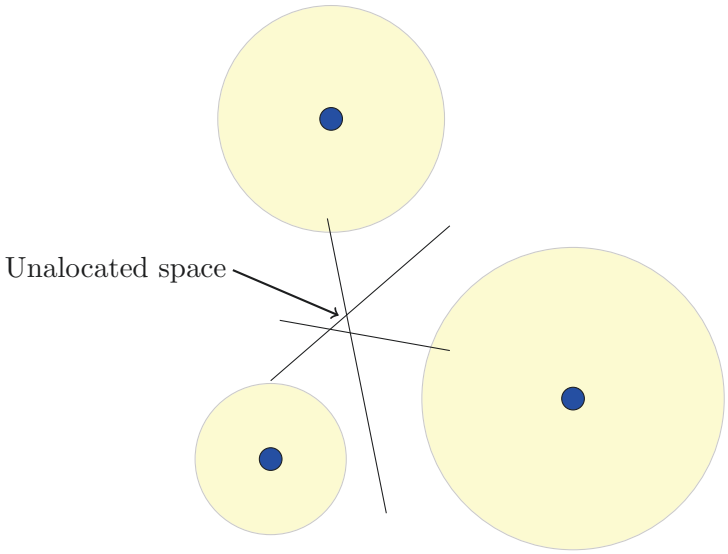

Figure 2.3: Richards' method B deficiency in allocation of space.

replace the bisecting planes and/or linear weighting of the space. In this method, which is known as Laguerre (radical) polyhedral decomposition, a point x belongs to the generalized Voronoi cell of particle i, if[19]:

$$d(x, x_i)^2 - r_i^2 < d(x, x_j)^2 - r_j^2 \quad \forall j \neq i \tag{2.33}$$

where r_i are the radii of the particles, x_i the position of the particle center, and $d(x, x_i)$ is the distance between x and x_i.

2.2 Conclusion

The problem of determining the mutual diffusion coefficients of polymer/solvent systems was reduced to finding the self diffusion coefficient of the components involved (Eq. 2.16). But as the self diffusion coefficients of macromolecules are usually orders of magnitude smaller than those of the solvent molecules, there is no need to evaluate the self diffusion coefficients of macromolecules. The other important part is the thermodynamic factor in Eq. 2.16, which can be evaluated using the Flory-Huggins theory by calculating the interaction parameter χ (Eq. 2.17). Calculation of the self diffusion coefficients and Flory-Huggins interaction parameter are the major focus of this study, and will be throughly discussed in the upcoming chapters.

Chapter 3

Molecular dynamics

3.1 Molecular dynamics

As we will discuss in Chapter 4, theoretically, it is possible to describe every system of interest on the ab initio level of calculation. Although ab initio calculations are very accurate, its computation cost gets prohibitively high by the size of the system. The next higher level of description, which in the following we will refer to as the atomistic level, can be reached by discarding the electronic degrees of freedom and replacing their interactions by effective coarsegrained interactions between the nuclei, expressed via classical potentials. In this picture, the motions of the atoms are treated classically, and their trajectory is propagated deterministically or stochastically through phase space, spanned by the respective particles degrees of freedom.

3.1.1 Molecular dynamics formalism

To explain this picture in more detail, let us in the following consider a system of N particles, which is described by the following Hamiltonian:

$$H(r,p) = \sum_{i=1}^{N} \frac{p_i^2}{2m_i} + \Phi(r) \tag{3.1}$$

where the first and second term represent the kinetic and potential energy, respectively. The variables $r = (r_1, ..., r_N)$ and $p = (p_1, ..., p_N)$ denote the sets of atomic positions and momenta, while m_i is the mass of the i_{th} atom. For an atomic system, the potential energy, $\Phi(r)$, consists of a set of equations that empirically describe bonded and non-bonded interactions between atoms. Such energy functions together with the set of their empirical parameters are referred to as the force field (for details of the force field used in this study see section 3.1.6). The potential energy $\Phi(r)$ is generally approximated by invoking the pair wise approximation, where many-body effects are partially included in the effective pair potential $\Phi_{ij}^{eff}(r_{ij})$. In the absence of any external field, the potential energy can then

be written as:

$$\Phi(r) \approx \sum_{i}^{N} \sum_{j>i}^{N} \Phi_{ij}^{eff}(r_{ij}) \tag{3.2}$$

where $r_{ij} = r_i r_j$ is the distance between particles i and j. The sum over atomic pairs comprise effective interactions between bonded and non-bonded atoms. A MD simulation is conducted by numerically integrating in time (t) Hamilton's equations of motion:

$$\frac{dp_i}{dt} = -\frac{\partial H(r,p)}{\partial r_i} \tag{3.3}$$

$$\frac{dr_i}{dt} = \frac{\partial H(r,p)}{\partial p_i} \tag{3.4}$$

for each of the N particles of the system. In three dimensions, this represents a set of $6N$-first-order differential equations, which are integrated numerically by subjecting them to the initial set of particle positions and momenta as well as periodic boundary conditions, to reduce the influence of the finite size effects. The resulting trajectory must be representative and evolve a sufficiently long time in phase space, to fulfill the quasi-ergodic theorem, expressed by:

$$O_{obs} = \langle O \rangle_{ens} = \lim_{t \to \infty} \langle O \rangle_t \tag{3.5}$$

where O_{obs} is the macroscopic physical quantity and $\langle O \rangle_{ens}$ is the corresponding ensemble average, while $\langle O \rangle_t$ is the time-average of the observable O over time.

3.1.2 Time integration

At the very heart of the MD simulation, beside the calculation of the potential energy and forces, there is a time integrator and its accuracy determins the quality of the results. Although there are numerical methods out there like predictor-corrector or velocity Verlet algorithms, in all the simulations done in this work, the well-known leap-frog algorithm was used. The leap-frog algorithm uses positions r at time t and velocities v at time $t - \frac{1}{2}\Delta t$. it updates positions and velocities using the forces $F(t)$ determined by the positions at time t using the following relations:

$$v(t + \frac{1}{2}\Delta t) = v(t - \frac{1}{2}\Delta t) + \frac{\Delta t}{m} F(t) \tag{3.6}$$

and

$$r(t + \Delta t) = r(t) + \Delta t v(t + \frac{1}{2}\Delta t) \tag{3.7}$$

3.1.3 Temperature control

MD in its very nature gives rise to the micro canonical ensemble (with constant number of particles, volume and energy, NVE). To control the temperature of the system some modifications, either in simulation procedure or Hamiltonian itself, is required. In this work, we used the Berendsen heat bath [20] for equilibration simulations and Nose-Hoover method [21] for cases when dynamics of the system was investigated (e.g., calculation of diffusion coefficient). A summary of both methods is presented here.

Berendsen Thermostat

The idea behind the Berendsen algorithm is to use an first-order kinetics (connected to an external bath with given temperature T_0) to correct the current temperature. It can be summarized as:

$$\frac{dT}{dt} = \frac{T_0 - T}{\tau} \tag{3.8}$$

where τ is the time constant of decay of T toward T_0. The Berendsen thermostat abolishes the fluctuations of the kinetic energy, which means that the sampling will be incorrect. This error scales with $1/N$, so this algorithm can be safely applied to large systems (except fluctuation properties like heat capacity). This is the reason why the Berendsen algorithm is only used for equilibration simulations only.

Nose-Hoover Thermostat

Unlike the Berendsen weak-coupling, extended ensemble approaches like Nose-Hoover method can probe a correct canonical ensemble. In this approach, the systems Hamiltonian is extended by introducing a thermal reservoir and a friction term in the equations of motion. The friction force is proportional to the product of each particle's velocity and a friction parameter,ξ. This friction parameter (or heat bath variable) is a fully dynamic quantity with its own momentum (p_ξ) and equation of motion. The time derivative is calculated from the difference between the current kinetic energy and the reference temperature. In this formulation, the particles' equations of motion are replaced by:

$$\frac{d^2 r_i}{dt^2} = \frac{F_i}{m_i} - \frac{p_\xi}{Q}\frac{dr_i}{dt} \tag{3.9}$$

where the equation of motion for the heat bath parameter ξ is:

$$\frac{dp_\xi}{dt} = (T - T_0) \tag{3.10}$$

The strength of the coupling is determined by the constant Q. The conserved quantity for the Nose-Hoover equations of motion is not the total energy, but rather:

$$H = \sum_{i=1}^{N} \frac{p_i}{2m_i} + \Phi(r_1, ..., r_N) + \frac{p_\xi^2}{2Q} + N_f k_B T \xi \tag{3.11}$$

where N_f is the total number of degrees of freedom.

The Nose-Hoover extended ensemble approach can be non-ergodic by itself, meaning that only a subsection of phase space is ever sampled, even if the simulations were to run for infinitely long time. For this reason, the Nose-Hoover chain approach was developed, where each of the Nose-Hoover thermostats has its own parameters. In the limit of an infinite chain of thermostats, the dynamics are guaranteed to be ergodic which is obviously impractical. Using just a few chains can greatly improve the ergodicity, so in this work 10 chains has been used. Readers are referred to GROMACS manual [22, 23] for the detail of the derivation of equations and implementation of chain Nose-Hoover algorithm.

3.1.4 Pressure control

The idea of weak-coupling and extended-ensemble can also be applied to controlling the pressure of the system by coupling the system to a pressure bath. The Berendsen algorithm that scales coordinates and box vectors every step was used for fast equilibration of the systems occasionally and the extended-ensemble Parrinello-Rahman [20] approach was used for preserve the dynamics of the system.

3.1.5 Periodic boundary condition

Ideally, a MD simulation should be performed on a very large system to reduce the effect of the box edge on the system properties on average. As always, there is a limitation for system size, due to computational costs, periodic boundary conditions (PBC) are classically applied to minimize the edge effects [24]. In this case, the atoms of the system to be simulated are put into a space-filling box, which is surrounded by translated copies of itself (see Figure 3.1). Although this way the unwanted effect of the boundaries is removed, another artifact, namely the artifact of periodic conditions, is introduced to the system. While such boundary conditions perfectly suit the simulation of crystalline materials, in the case of non-crystalline materials, periodicity by itself causes errors (Particles correlation with their own periodic image). Fortunately, there is a way to reduce this error by comparing several system sizes and selecting a minimum size for the system. Accordingly, in almost all the analysis done in this work, the effect of system size was checked to find error introduced by periodicity, if any.

Also, when PBCs are used, care should be taken not to violate the minimum image convention. Non-bonded interactions are cut-off at some specific distance which is usually selected independent of the box size to adjust the accuracy of the calculations. In general,

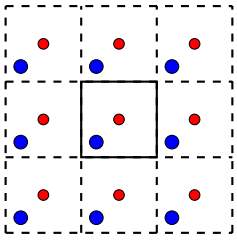

Figure 3.1: Periodic boundary condition representation in 2D space. The solid rectangle is the primary box and the 8 other dashed boxes are periodic images.

the box size should be at least twice of the cut-off distance used [24]. Otherwise, particles start to interact (different from correlation in motion discussed above) with their own periodic image directly which does not have physical equivalent.

3.1.6 Force field

In all simulations done in this work, the OPLS-AA [25] was used for the calculation of the interactions between atoms in the system. Accordingly, the discussion on the formalism of the MD force field is limited to those used in the OPLS-AA. For the detail of the parameters used, rereads are referred to the GROMACS manual[22, 23].

The potential functions in the OPLS-AA force field can generally be divided to two distinct sub-groups:

- Non-bonded
  - Dispersive Van der Waals interactions which are modeled by Lennard-Jones (12-6).
  - Electro-static interactions which are modeled by Coulomb law.
- Bonded:
  - Covalent bond-stretching which is modeled by classical harmonic oscillator.
  - Angle-bending which is modeled by classical harmonic oscillator.
  - Proper dihedrals which is modeled by Recaert-Belmann model.
  - Improper dihedrals which is modeled by Ryckaert-Belleman model.

Lennard-Jones

A commonly used two-parameter potential model for describing non-bonded interactions between a pair of neutral atoms is the Lennard-Jones 6-12 potential:

$$\Phi_{LJ}(r_{ij}) = 4\epsilon \left[\left(\frac{\sigma_{ij}}{r_{ij}} \right)^{12} - \left(\frac{\sigma_{ij}}{r_{ij}} \right)^{6} \right] \tag{3.12}$$

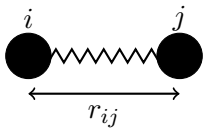

Figure 3.2: Schematic representation of two bonded atoms.

where ϵ represents the potential well depth and σ is the pair separation at zero energy. In the OPLS-AA force field, the geometric average is used as the combination rule which reads:

$$\sigma_{ij} = \sqrt{\sigma_{ii}\sigma_{jj}} \quad and \quad \epsilon_{ij} = \sqrt{\epsilon_{ii}\epsilon_{jj}} \tag{3.13}$$

Coulomb interactions

The Coulomb interaction between two charged particles is given by:

$$\Phi_C(r_{ij}) = \frac{1}{4\pi\varepsilon_0}\frac{q_i q_j}{\varepsilon_r r_{ij}} \tag{3.14}$$

where ε_0 and ε_r are the free space and relative permittivity and q_i is the partial atomic charge of particle i.

Bond-stretching

The bond stretching between two covalently bonded atoms i and j is represented by a harmonic potential:

$$\Phi_b(r_{ij}) = \frac{1}{2}k^b_{ij}(r_{ij} - b_{ij}) \tag{3.15}$$

where k^b_{ij} is the force constant and b_{ij} is the equilibrium bond length.

Angle-bending

The bond-angle vibration between a triplet of atoms $i-j-k$ is represented by a harmonic potential on the angle θ_{ijk} :

$$\Phi_a(\theta_{ijk}) = \frac{1}{2}k^\theta_{ijk}(\theta_{ijk} - \theta^0_{ijk})^2 \tag{3.16}$$

where k^θ_{ijk} is the force constant and θ^0_{ijk} is the equilibrium bond angle.

Proper dihedrals

For the normal dihedral interaction, the OPLS-AA force field uses a function based on the expansion in powers of $\cos\phi$ (the so-called Ryckaert-Belleman potential):

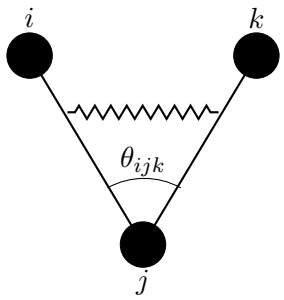

Figure 3.3: Schematic representation of bond-angle between three bonded atoms.

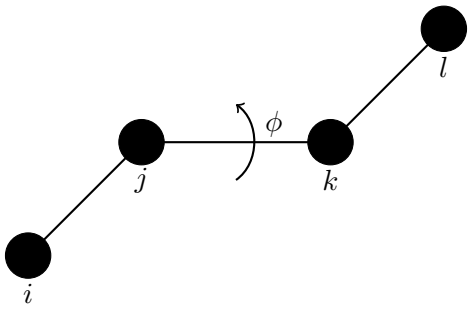

Figure 3.4: Schematic representation of dihedral-angle between four bonded atoms.

$$\Phi_d(\phi_{ijkl}) = \sum_{n=0}^{5} C_n \left(cos(\phi - 180)\right)^n \tag{3.17}$$

1-4 interactions and exclusions

Atoms within a molecule that are close by, i.e. atoms that are covalently bonded, or linked by one or two atoms are called first neighbors, second neighbors and third neighbors, respectively (see Figure 3.5). Since the interactions of atom i with atoms $i+1$ and $i+2$ are mainly quantum mechanical, they can not be modeled by a Lennard-Jones potential. Instead, it is assumed that these interactions are adequately modeled by a harmonic bond term (i and $i+1$) and a harmonic angle term (i and $i+2$). The first and second neighbors (atoms $i+1$ and $i+2$) are therefore excluded from the Lennard-Jones interaction list of atom i. For third neighbors ($i+3$), the normal Lennard-Jones repulsion is sometimes still too strong, which means that when applied to a molecule, the molecule would deform or break due to the internal strain. This is especially the case for carbon-carbon interactions in a cis-conformation. Therefore, for these cases in the OPLS-AA force field, the Lennard-Jones and Coulombic interactions are scaled down by a fudge factor of 0.5, which is implemented by keeping a separate list of 1-4 and normal parameters.

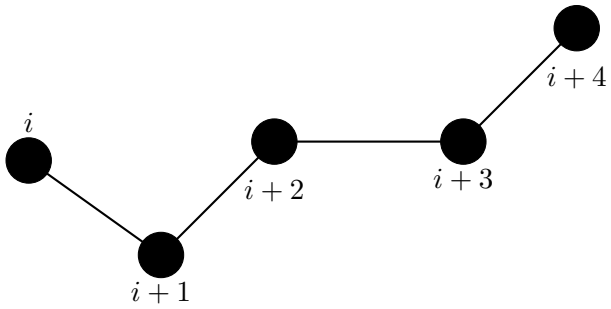

Figure 3.5: Schematic representation of bond-angle between three bonded atoms.

3.2 Calculation of free energy of solvation-Slow growth method

In Chapter 6 free energy of solvation for oligomers of PVA in water was calculated using MD simulation[1]. In this section, the theory behind the calculation is explained. Free energy differences between two different states of the system can be calculated by the slow-growth method. The method requires a simulation during which the Hamiltonian of the system changes slowly from that describing one state (A) to that describing the other state (B). The change must be so slow that the system remains in equilibrium during the process. If that requirement is fulfilled, the change is reversible and a slow-growth simulation from B to A will yield the same results (but with a different sign) as a slow-growth simulation from A to B. The required modification of the Hamiltonian H is realized by making H a function of a coupling parameter λ:$H = H(p, q, \lambda)$ in such way that $H_{\lambda=0}$ describes the state B, in our case oligomers in vacuum, and $H_{\lambda=1}$ describes the state A, in our case solvated oligomers.

The Gibbs free energy G is related to the partition function Δ of an NPT ensemble, which is assumed to be the equilibrium ensemble generated by a MD simulation at constant pressure and temperature:

$$G(\lambda) = -k_B T ln\Delta \tag{3.18}$$

where Δ is:

$$\Delta = \frac{1}{N!h^{3N}} \int\int\int e^{-\frac{H(p,q,\lambda)}{k_B T}}\, dp\, dq\, dV \tag{3.19}$$

where h is Planck's constant. These integrals over the phase space cannot be evaluated from a simulation, but it is possible to evaluate the derivative with respect to λ as an ensemble average:

[1]Note that free energy of solvation for PVA oligomer also was calculated on the ab initio level. But as the detail of the method applied is out of the scope of this work, the theory behind the calculation is not discussed. Readers are referred to a great review by Tomasi et al. [26] for a through discussion on the theory of quantum mechanical continuum solvation models

$$\frac{dG}{d\lambda} = \frac{\int\int \frac{\partial H}{\partial \lambda} e^{-\frac{H(p,q,\lambda)}{k_B T}}\, dp\, dq}{\int\int e^{-\frac{H(p,q,\lambda)}{k_B T}}\, dp\, dq} = \langle \frac{\partial H}{\partial \lambda} \rangle_{NPT\lambda} \tag{3.20}$$

The difference in free energy between A and B can be determined by integrating the derivative over λ:

$$G^B(p,T) - G^A(p,T) = \int_0^1 \langle \frac{\partial H}{\partial \lambda} \rangle_{NPT\lambda} d\lambda \tag{3.21}$$

Theoretically, it is possible to integrate Eq. 3.21 in one simulation over the full range from A to B. However, for large changes, insufficient sampling can be expected. So we determined the value of $\langle \frac{\partial H}{\partial \lambda} \rangle$ accurately at a number of well-chosen intermediate values of λ. This way each simulation equilibrated first following by a production simulation of sufficiently long. While we used the thermodynamic integration scheme to show the concept of calculation, the total free energy change is actually determined by using of Bennett's Acceptance Ratio [27] for transformation from state A to state B.

Chapter 4

Density functional theory

4.1 Introduction

At the very heart of the computational chemistry or modeling of the materials, the only important factor which defines the quality of the results is the way that interaction between particles (electrons, atoms or molecules) is defined. In the MD calculation, as we discussed in Chapter 3, these interactions are described in the realm of classical dynamics using very basic definitions like harmonic oscillator or torsion angle constraints which are known as force fields. While a well parametrized force field can predict certain properties of the system correctly, there comes other properties which can be certainly out of reach for them either due to insufficiency of the formalism of the force field or quality of the parameters. Accordingly, revisiting of the force fields is inevitable from time to time. As we will discuss later in Chapters 5 and 6, on several occasions, we used first principle calculations to modify and/or to confirm the quality of the OPLS-AA force field.

For all the first principle calculations we did, a variant of density functional theory (DFT) was used. We also used the Hartree-Fock (HF) formalism occasionally to double check the accuracy of the results. In this chapter, a brief introduction of the DFT is provided; readers are referred to elsewhere [28–35] for an introductory discussion on quantum mechanics, HF calculation and its application.

Since its appearance, DFT, owing to its usage of plane wave approximation, was mostly used in the study of periodic systems and crystals. It was until recently that chemists successfully adopted a variant of DFT which is now widely used for the simulation of energy surfaces of molecular systems[31, 36]. In this chapter, the basic concepts underlying density functional theory and outline the features that have lead to its wide spread adoption will be discussed.

4.2 Schrodinger Equation

The fundamental question of the (any) electronic structure calculation method is the calculation of the ground state energy of a collection of atoms which requires to solve the Schrodinger equation. The time independent and non-relativistic form of Schrodinger equation after applying the Born-Oppenheimer approximation is:

$$\hat{H}\Psi(r_1, r_2, ..., r_N) = E\Psi(r_1, r_2, ..., r_N) \tag{4.1}$$

where Ψ is the wave function, r_i are the spatial coordinates and E is the energy (eigen value). The Hamiltonian operator, H, has three terms namely the kinetic energy, the interaction with the external potential and the electron-electron interaction which are shown in Equation 4.2 respectively:

$$\hat{H} = -\frac{1}{2}\sum_{i}^{N}\nabla_i^2 + \hat{V}_{ext} + \sum_{i<j}^{N}\frac{1}{|r_i - r_j|} \tag{4.2}$$

The external potential of interest for simulation of materials under normal conditions without any external interference is simply the interaction of the electrons with the atomic nuclei:

$$\hat{V}_{ext} = -\sum_{\alpha}^{N_{atom}}\frac{Z_\alpha}{|r_i - R_\alpha|} \tag{4.3}$$

Here, r_i is the coordinate of electron i and the charge on the nucleus at R_α is Z_α. Note that in order to simplify the notation and to focus on the discussion of the main features of DFT, the spin coordinate is omitted. Equation 4.1 is solved for a set of Ψ subjected to the constraint that the Ψ are antisymmetric (they change sign if the coordinates of any two electrons are interchanged). The lowest energy eigenvalue, E_0, is the ground state energy and the probability density of finding an electron with any particular set of coordinates $\{r_i\}$ is $|\Psi|^2$.

Note that any state of the system specified by an arbitrary Ψ (not necessarily one of the eigenfunctions of Equation 4.1) has an average total energy which is the expectation value of H as follows:

$$E[\Psi] = \int \Psi^* \hat{H}\Psi dr = \langle\Psi|\hat{H}|\Psi\rangle \tag{4.4}$$

Note that to emphasis that energy is a functional of wave function, we have used the notation $[\Psi]$. According to the variational theorem [36], the lowest possible energy,E_0, corresponds to the ground state, $[\Psi_0]$, which translates to:

$$E[\Psi] \geq E_0 \tag{4.5}$$

The ground state wave function and energy may be determined by searching all possible wave functions for the one that minimizes the total energy. Conventionally, solving the Schrodinger equation and determine the 3N dimensional wave function is the subject of the HF method and is quiet costly in computation sense. There is a smarter way to bypass this cost by using the concept of electron density which is the topic of the DFT.

4.3 DFT formalism

Based on the fact that Hamiltonian operator in Equation 4.2 only involves on the coordinates of one or two electrons only, there is no need of knowing the $3N$ dimensional wave function to compute the total energy. Knowledge of the probability of finding an electron at r_1 and an electron at r_2 is sufficient. To make the discussion easier we define a second order density matrix,P_2, as follows:

$$P_2(r_1', r_2'; r_1, r_2) = \frac{N(N-1)}{2} \int \Psi^*(r_1', r_2', ..., r_N')\Psi(r_1, r_2, ..., r_N)dr_3 dr_4 ... dr_N \tag{4.6}$$

The diagonal elements of P_2, often referred to as the two-particle density matrix or pair density, are:

$$P_2(r_1, r_2) = P_2(r_1, r_2; r_1, r_2) \tag{4.7}$$

This is the required two electron probability function to define all two particle operators. The first order density matrix is defined in a similar manner and may be written in terms of P_2 as:

$$P_1(r_1'; r_1) = \frac{2}{N-1} \int P_2(r_1', r_2; r_1, r_2)dr_2 \tag{4.8}$$

Given P_1 and P_2 the total energy is determined exactly:

$$E = tr\left(\hat{H}\hat{P}\right) = \int \left[\left(-\frac{1}{2}\nabla_1^2 - \sum_{\alpha}^{N_{atom}} \frac{Z_\alpha}{|r_1 - R_\alpha|} \right) P_1(r_1', r_1) \right]_{r_1 = r_1'} dr_1 + \int \frac{1}{|r_1 - r_2|} P_2(r_1, r_2)dr_1 dr_2 \tag{4.9}$$

Now, it is clear that the diagonal elements of the first and second order density matrices completely determine the total energy. Accordingly, The solution of the full Schrodinger equation for Ψ is not required. It is just required to determine the P_1 and P_2 which reduces the number of dimensions from $3N$ to 6. Note that there is no direct way to minimize the $E(P_1, P_2)$ to find the ground state solution, as it occurs that final density matrices are not legal (they can not fulfill antisymmetric Ψ requirement).

4.3.1 The Hohenburg-Kohn Theorems

In the process of making the equation 4.9 applicable for the calculation of the ground state energy, Hohenburg and Kohn proved two theorems as follows:

- The electron density determines the external potential (to within an additive constant).
- For any positive definite trial density, ρ_t, such that $\int \rho_t(r)dr = N$ then $E[\rho_t] \geq E_0$.

The first statement implies that the electron density uniquely determines the Hamiltonian operator (Eq 4.2) and all material properties consequently. This is direct result of the fact that Hamiltonian is specified by the external potential and the total number of electrons, N, which can be computed from the density simply by integration over all space. For the detail of the proof of this theorem and its generalization to degenerates states readers are referred to original work of Hohenburg and Kohn [37] and work of Levy [38].

The proof of second theorem is straightforward. From the first theorem, we know that the trial density determines a unique trial Hamiltonian (H_t) and thus wave function (Ψ_t). So:

$$E[\rho_t] = \langle \Psi_t | H | \Psi_t \rangle \geq E_0 \tag{4.10}$$

which follows immediately from the variational theorem of the Schrodinger equation (Eq 4.5).

The two theorems lead to the fundamental statement of density functional theory:

$$\delta \left[E[\rho] - \mu(\int \rho(r)dr - N) \right] = 0 \tag{4.11}$$

The above statement ensures that the density corresponding to the minimum of some functional $E[\rho]$ (ground state) contains the correct number of electrons. The Lagrange multiplier of this constraint is the electronic chemical potential μ. This discussion simply clarifies that there is a universal functional $E[\rho]$ (we don't know it yet) which can be inserted into the above equation and minimized to obtain the exact ground state density and energy.

4.3.2 Energy functional

From the form of the Schrodinger equation (Eq 4.1), we can see that the energy functional contains three terms: the kinetic energy, the interaction with the external potential and the electron-electron interaction and so we may write the functional respectively as:

$$E[\rho] = T[\rho] + V_{ext}[\rho] + V_{ee}[\rho] \tag{4.12}$$

The interaction with the external potential is trivial:

$$V_{ext}[\rho] = \int \hat{V}_{ext}\rho(r)dr \tag{4.13}$$

The kinetic and electron-electron functionals are unknown. The direct minimization of the energy would be possible only if a proper estimation to these functionals could be found which is the place of debate after introduction of the DFT. Kohn and Sham proposed the following approach to approximating the kinetic and electron-electron functionals [39]. They introduced a fictitious system of N noninteracting electrons to be described by a single determinant wave function in N orbitals ϕ. In this system the kinetic energy and electron density are known exactly from the orbitals:

$$T_s[\rho] = -\frac{1}{2}\sum_{i}^{N}\langle\phi_i|\nabla^2|\phi_i\rangle \tag{4.14}$$

Here, the suffix emphasizes that this is not the true kinetic energy but is that of a system of non-interacting electrons, which reproduce the true ground state density. So, we have:

$$\rho(r) = \sum_{i}^{N}|\phi_i|^2 \tag{4.15}$$

The construction of the density explicitly from a set of orbitals ensures that it is legal (it can be constructed from an asymmetric wave function). Also, a significant component of the electron-electron interaction will be the classical Coulomb interaction

$$V_H[\rho] = \frac{1}{2}\int\frac{\rho(r_1)\rho(r_2)}{|r_1 - r_2|}dr_1dr_2 \tag{4.16}$$

So, the energy functional can be rearranged as:

$$E[\rho] = T_s[\rho] + V_{ext}[\rho] + V_H[\rho] + E_{xc}[\rho] \tag{4.17}$$

where we have introduced the exchange-correlation functional:

$$E_{xc}[\rho] = (T[\rho] - T_s[\rho]) + (V_{ee}[\rho] - V_H[\rho]) \tag{4.18}$$

E_{xc} is simply the sum of the error made in using a non-interacting kinetic energy and the error made in treating the electron-electron interaction classically. Writing the functional (Eq 4.17) explicitly in terms of the density built from noninteracting orbitals (Eq 4.16) and applying the variational theorem (Eq 4.11) we find that the orbitals, which minimize the energy, satisfy the following set of equations:

$$\left[-\frac{1}{2}\nabla^2 + v_{ext}(r)\int\frac{\rho(r')}{|r - r'|}dr' + v_{xc}(r)\right]\phi_i(r) = \varepsilon_i\phi_i(r) \tag{4.19}$$

In which a local multiplicative potential which is the functional derivative of the exchange correlation energy with respect to the density has been introduced:

$$v_{xc}(r) = \frac{\delta E_{xc}[\rho]}{\delta \rho} \tag{4.20}$$

This set of non-linear equations (the Kohn-Sham equations) describes the behavior of non-interacting electrons in an effective local potential. For the exact functional, and thus exact local potential, the orbitals yield the exact ground state density via Equation 4.15 and exact ground state energy via Equation 4.17. These Kohn-Sham equations have the same structure as the Hartree-Fock equations with the non-local exchange potential replaced by the local exchange-correlation potential. The Kohn-Sham approach achieves an exact correspondence of the density and ground state energy of a system consisting of non-interacting Fermions and the real many body system described by the Schrodinger equation.

The correspondence of the charge density and energy of the many-body and the non-interacting system is only exact if the exact functional is known. In this sense, Kohn-Sham density functional theory is an empirical methodology (there is no way to determine the exact functional). However, the functional is universal it does not depend on the materials being studied. For any particular system we could, in principle, solve the Schrodinger equation exactly and determine the energy functional and its associated potential. This, of course, involves a greater effort than a direct solution for the energy. Nevertheless, the ability to determine exact properties of the universal functional in a number of systems allows excellent approximations to the functional to be developed and used in unbiased and thus predictive studies of a wide range of materials. For this reason, the approximations of DFT are often referred to as ab initio or first principles methods.

The computational cost of solving the Kohn-Sham equations (Equation 4.19) scales formally as N^3 (due to the need to maintain the orthogonality of N orbitals) but in current practice this is dropping towards N^1 through the exploitation of the locality of the orbitals. For calculations in which the energy surface is the quantity of primary interest, DFT offers a practical and potential highly accurate alternative to the wave function methods. In practice, the utility of the theory rests on the approximation used for $E_{xc}[\rho]$. For the sake of completeness, one of the simplest way to approximate $E_{xc}[\rho]$, the Local Density Approximation (LDA), is discussed in the next section and for more elaborate methods, readers are referred to elsewhere[31, 36].

4.3.3 Local Density Approximation (LDA)

Generating proper approximation for $E_{xc}[\rho]$ is still an active field of research. Different flavors of functional have been generated which can be applied to any particular study more or less. But careful investigation of results is the only way to judge the success of the applied approximation.

The very basic idea of DFT came from a very specific example, the homogeneous electron gas. In this system, the electrons are subject to a constant external potential and thus the charge density is constant. Thus, a single number (electron density $r = \frac{N}{V}$) defines the system. Long time before introducing the DFT, Thomas and Fermi studied the homogeneous electron gas and showed that orbitals of the system are, by symmetry, plane waves. So, if the electron-electron interaction is approximated by the classical Hartree potential (that is exchange and correlation effects are neglected) then the total energy functional can be readily computed. Under these conditions, the dependence of the kinetic and exchange energy on the density of the electron gas can be extracted and expressed in terms of a local functions of the density. This suggests that in the inhomogeneous system, we might approximate the functional as an integral over a local function of the charge density. Using the kinetic and exchange energy densities of the non-interacting homogeneous electron gas this leads to:

$$T[\rho] = 2.87 \int \rho^{\frac{5}{3}}(r)dr \tag{4.21}$$

and

$$E_x[\rho] = 0.74 \int \rho^{\frac{4}{3}}(r)dr \tag{4.22}$$

These results are highly suggestive of a representation for E_{xc} in an inhomogeneous system. The local exchange correlation energy per electron might be approximated as a simple function of the local charge density ($\varepsilon_{xc}(\rho)$). That is, an approximation of the form:

$$E_{xc}[\rho] \approx \int \rho(r)\varepsilon_{xc}(\rho(r))dr \tag{4.23}$$

An obvious choice is then to take $\varepsilon_{xc}(\rho)$ to be the exchange and correlation energy density of the uniform electron gas of density ρ (this is the LDA). Within the LDA, $\varepsilon_{xc}(\rho)$ is a function of only the local value of the density. It can be separated into exchange and correlation contributions as follows:

$$\varepsilon_{xc}(\rho) = \varepsilon_x(\rho) + \varepsilon_c(\rho) \tag{4.24}$$

The Dirac form can be used for ε_x (Eq 4.22);

$$\varepsilon_x(\rho) = -C\rho^{\frac{1}{3}} \tag{4.25}$$

where constant C serves to generalize the answer from those of the homogeneous electron gas. The functional form for the correlation energy density, ε_c, is unknown and has been simulated for the homogeneous electron gas in numerical quantum Monte Carlo calculations which yield essentially exact results. The resultant exchange correlation energy has been fitted by a number of analytic forms all of which yield similar results in practice and are

collectively referred to as LDA functionals.

The LDA has proven to be a remarkably fruitful approximation. Properties such as structure, vibrational frequencies, elastic moduli and phase stability (of similar structures) are described reliably for many systems. However, in computing energy differences between rather different structures, the LDA can have significant errors. For instance, the binding energy of many systems is overestimated (typically by 20-30 %) and energy barriers in diffusion or chemical reactions may be too small or absent. As it was discussed before, the DFT theory and LDA approximation of exchange correlation function originated from study of the homogeneous electron gas system followed by crystalline silicon structure. These systems are, having a smooth change in gradient of the charge density, are different from organic materials with known sharp changes in the charge density in the space. Accordingly, several hybrid exchange correlation functions developed to consider such sharp changes. A hybrid exchange-correlation functional is usually constructed as a linear combination of the HartreeFock exact exchange functional and any number of exchange and correlation explicit to density functionals. One of the most popular hybrid functionals is the Becke, three-parameter, Lee-Yang-Parr (B3LYP) functional [40]:

$$E_{xc}^{B3LYP} = E_x^{LDA} + 0.20(E_x^{HF} - E_x^{LDA}) + 0.72(E_x^{GGA} - E_x^{LDA}) + E_c^{LDA} + 0.81(E_c^{GGA} - E_c^{LDA}) \tag{4.26}$$

where subscript x and represents the exchange and correlation functionals, respectively and super scripts HF and GGA represents the HartreeFock and generalized gradient approximation. Note that for all DFT calculations in this work the Gaussian09 package [41] [42] was used.

4.4 Population analysis and partial atomic charges

Unlike many other properties, atomic charge is a quantity which is not rigorously defined in quantum mechanics [43]. Usually, calculation of atomic charges is a post processing calculation after achieving the required energy convergence and there are numerous methods to do such calculation. In Chapter 6 we have used some of these methods to derive the atomic charges of PVA oligomers under different conditions. Among all these methods, the Merz-Singh-Kollman (MSK) [43, 44] scheme yielded much more promising results. Accordingly, a brief introduction of the method is presented here.

The basic idea behind the MSK method is to reproduce the molecular electrostatic potential (ESP) around the molecule under study which can be calculated as a quantum mechanical observable. In the MSK method atomic charges are fitted to reproduce the

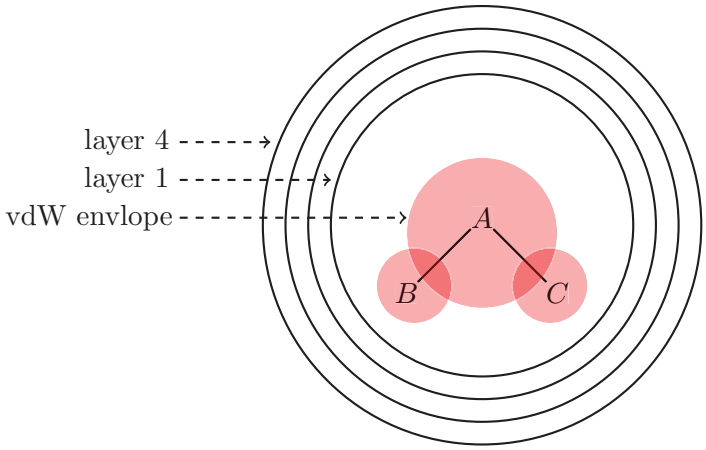

Figure 4.1: Schematic representation of the MSK scheme.

molecular electrostatic potential (ESP) at a number of points around the molecule [43, 44]. As a first step of the fitting procedure, the ESP is calculated at a number of grid-points located on several layers around the molecule (see figure 4.1). The layers are constructed as an overlay of vdW spheres around each atom. All points located inside the vdW volume are discarded. Best results are achieved by sampling points not too close to the vdW surface and the vdW radii are therefore modified through scaling factors [43, 44]. The smallest layer is obtained by scaling all radii with a factor of 1.4. After evaluating the ESP at all valid grid points located on all four layers, atomic charges are derived that reproduce the ESP as closely as possible. The only additional constraint in the fitting procedure is that the sum of all atomic charges equals that of the overall charge of the system. The Charges derived in this way don't necessarily reproduce the dipole moment of the molecule. The MSK charge fitting scheme can be modified in the following way in order to improve its numerical accuracy:

- Using more than four layers of points which is necessary for systems with diffusive orbitals.
- Using more grid points per layer which is necessary for highly polarized molecules.

Charges calculated using the MSK scheme show a similarly small dependence on the computational method and basis sets employed.

4.5 Quantum harmonic oscillator

In Chapter 5, we will use the quantum harmonic oscillator to quantum modify the classical heat capacity. Here, a brief derivation of the equations is presented. The Hamiltonian for a one dimensional quantum harmonic oscillator is defined as:

$$\hat{H} = -\frac{\bar{h}}{2m}\frac{\partial^2}{\partial x^2} + \frac{1}{2}m\omega^2 x^2 \tag{4.27}$$

So, the Schrodinger equation is:

$$i\bar{h}\frac{\partial \Psi}{\partial t} = \hat{H}\Psi \tag{4.28}$$

Separating the time dependent part by the separation of variable, the stationary Schrodinger equation of this system is [29]:

$$[\frac{\bar{h}}{2m}\frac{d^2}{dx^2} + \frac{1}{2}m\omega^2 x^2]\psi(x) = E\psi(x) \tag{4.29}$$

where the $\psi(x)$ is the time independent wave function as follows:

$$\Psi(x,t) = \psi(x)e^{-iEt/\bar{h}} \tag{4.30}$$

Solving Equation 4.29, the energy eigenvalues of harmonic oscillator with classical angular frequency ω are given by:

$$E_n = (n + \frac{1}{2})\bar{h}\omega \quad with \quad n = 0, 1, 2, 3, ... \tag{4.31}$$

The partition function for this system is then:

$$Z = \sum_0^\infty e^{-\beta E_n} = e^{-\frac{1}{2}\beta\bar{h}\omega}\sum_0^\infty e^{(-n\beta\bar{h}\omega)} \tag{4.32}$$

where β is simply the $\frac{1}{k_b T}$. Sum of the infinite geometric series in Eq 4.32 is easily calculated to be:

$$Z = \frac{e^{-\frac{1}{2}\beta\bar{h}\omega}}{1 - e^{(-\beta\bar{h}\omega)}} \tag{4.33}$$

also from section 2.1.7 we know that:

$$\langle E\rangle = -\frac{\partial ln Z}{\partial \beta} \quad and \quad C_v = \frac{\partial\langle E\rangle}{\partial T} \tag{4.34}$$

so putting the Z from Equation 4.33 into Equation 4.34, the quantum weight function for C_v in Chapter 5 is[45]:

$$W_{cv} = \frac{(\beta\bar{h}\omega)^2 e^{\beta\bar{h}\omega}}{(1 - e^{\beta\bar{h}\omega})^2} \tag{4.35}$$

Chapter 5

PVA melt simulation and force field validation

5.1 Introduction

Owing to its film-forming property, barrier properties, hydrophilicity and excellent chemical stability [2], poly(vinyl alcohol) (PVA) has been gradually used in a variety of applications such as drug encapsulation and delivery, composite materials, metal nano-particles stabilization [6] and active separation layers of pervaporation membranes [3], to name a few.

Like many other vinyl polymers, PVA exists in three possible stereomers (i.e., atactic, syndiotactic and isotactic). Due to its manufacturing process, commercial PVA is usually in the atactic form [5, 46–48]. However, detailed information about the tacticity of a PVA sample can be established by nuclear magnetic resonance (NMR) spectroscopy [5]. It is well known that physical properties of vinyl polymers (e.g., glass transition temperature) depend on their tacticity [49]. It is expected that PVA has no exception [5]. However, results reported in this work seem not to support such an expectation. It has also been reported that PVA, even in its atactic form, is a semicrystalline polymer with a moderate level of crystallinity but its crystal structure has not yet been completely established because of its complicated structure and hydrogen bonding capability [50].

There exist quite a few reports on the use of molecular dynamics (MD) simulation to study PVA. These include its chain dynamics, interactions between PVA and various solvents and other polymers, PVA hydrogels and so on [6, 47, 51–53]. The force field used in majority of these studies were developed by Muller-Plathe et al. [48]. The COMPASS force field was also used [54–56]. Although most of these authors have been able to obtain good agreement with experiment for pure PVA, it is inconvenient to study new systems of interest involving both PVA and molecules of different types as re-parameterization is required. Obviously, using a force field that is optimized for PVA and a wide variety of

A modified version of this chapter was published: "Thermodynamic Properties of Poly(vinyl alcohol) with Different Tacticities Estimated from Molecular Dynamics Simulation",A. Noorjahan, P. Choi, Polymer 54 (2013) 4212-4219.

compounds would be beneficial. Another issue of the aforementioned works is that small system size and/or short chains, as probably constrained by the computer resources available at the time, were used. In some cases, chains contained only up to 10 monomers [6] were used. While this is acceptable for the calculation of certain thermodynamic properties (e.g., specific volume), it is not the case for conformational sensitive properties (e.g., solubility parameter). In such cases, longer chains are needed. However, when longer chains are used, proper equilibration before MD simulation becomes an issue.

In light of the previous simulation works and taking the advantage of the computer resources available to the authors, we carried out a comprehensive set of MD simulations on PVA with different tacticities using the OPLS-AA force field to calculate a few key thermodynamic properties over a wide temperature range (200-550 K) encompassing both the glass transition and melting temperatures of PVA. The OPLS-AA force field was chosen as it is optimized for a variety of biomolecules and organic solvents. To address the equilibration issue, we used a relaxation strategy proposed by Belmares et al. [57]. The tacticity is of interest in the present work as its effect on properties of PVA has not been fully addressed in the simulation literature yet although Fossheim [49] did some work in this area.

5.2 Molecular Dynamics Simulation

In this work, GROMACS 4.5.5 [58–62] was used to perform all MD simulations using the OPLS-AA force field [25] as implemented in GROMACS (For detail of the atom type setting for PVA see Appendix B). However, in one simulation, we used OPLS-AA parameters with the partial atomic charges taken from the COMPASS force field [54] in order to compare our results with those of Wu [63]. In the preliminary work, we used other force fields including Amber [64] and force field parameters derived by Muller et al. [48] and found that the OPLS-AA [25] yielded results that are most comparable to those of experiments. Also the comparison between the present work and that of Wu [63] suggests that the OPLS-AA results are comparable to those of using the COMPASS [54] force field if not better. We are confident in the force field we chose. We used Nose-Hoover thermostat [21] with a time constant of 0.2 ps and Parrinello-Rahman barostat [65] with a time constant of 2 ps to control the temperature and pressure of the model systems, respectively. In all simulations, the time step used was 1 fs and the sampling time was 1 ps unless otherwise stated. A cut-off distance of 1 nm was used for all non-bonded interactions except for those simulations using a single short chain where a cut-off distance of 0.6 nm was used to prevent the violation of minimum image convention. We used Particle Mesh Ewald (PME) for the long range Coulombic interactions [60]. We also applied the pressure correction to retrieve the correct density of the system as pointed out by Wu [63]. For detail of the pressure correction method readers can refer to GROMACS manual [22]. All properties were calculated over the temperature range of 200 to 550 K with an interval of 10 K and the simulation time used was 100 ns excluding equilibration phase, which varied between

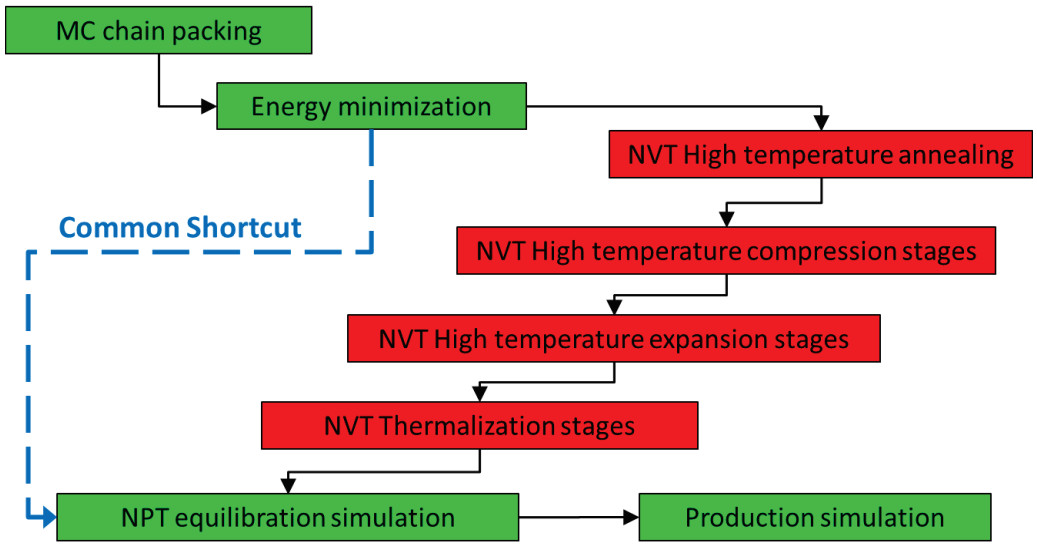

Figure 5.1: Flowchart of steps used during annealing.

60 to 100 ns. To decide whether a system has been equilibrated or not, we compared the energy, specific volume and solubility parameter of the system in 10 ns intervals. When the difference was less than recommended margins, it was concluded that equilibration was achieved. Since simulation of polymeric systems is usually non-ergodic [66], average on several different initial configurations were used to generate better estimate of properties. At totally 21 different temperatures ranging from 300 to 510 K (7 temperatures randomly selected from each stereomers), simulations were extended to 500 ns and beyond to check if system properties underwent further changes. Once again, we compared the specific volume, solubility parameter and conformational properties of the systems in the first and last 100 ns and no significant differences were found, suggesting that production simulations would generate reliable statistics after equilibration (60-100 ns simulations).

5.2.1 High Temperature Equilibration

It is well known that polymer relaxation is a slow process relative to small molecules and usually occurs in time scales beyond the capability of the MD simulation. Accordingly, MD simulation of polymeric systems is not ergodic and only a portion of the phase space close to the initial configuration is sampled [66]. In general, using well-relaxed chains as the initial structures for the corresponding MD simulations is crucial for accurate prediction of the equilibrium properties of polymers. To generate well-relaxed chains, we have followed the protocol proposed by Belmares et al. [57] with some modifications as follows (see figure 5.1):

1. All PVA chains (atactic, syndiotactic and isotactic) were generated using the polymer builder toolbox in Materials Studio 4.0 [67]. For all atactic chains, tacticity has been

assigned randomly with chiral inversion probability of 50 % (i.e., the ratio of meso diads to racemo diads is 50%). This random assignment of the tacticity, as mentioned by Rossinsky et al. [6], is consistent with commercial PVA chains formed by free radical polymerization. The connections for all isotactic and syndiotactic chains were head-to-tail. This is justified by the experimental findings of Flory et.al. [68] in which they showed that depending on the temperature of the polymerization, the percentage of the head-to-head connection of the PVA monomers varies between 1% (at 298 K) to 2% (at 385 K). End groups for all chains were CH_3. Chains generated were then assembled in a cubic simulation cell subjected to three dimensional periodic boundary conditions at half of the target density (maximum experimental value reported at 300 K) using the Monte Carlo method developed by Theodorou and Suter [69] as implemented in the amorphous builder module of Materials Studio. A short energy minimization was done to remove all close contacts within the cell afterwards.

2. In the next step, all simulation cells were annealed according to protocol proposed by Belmares et al. [57]. During annealing, the target density was chosen to be 1310 kg/m^3 [5, 70–74]. Starting with cells generated in Materials Studio with density of 655 kg/m^3, we compressed each cell to 125% of the target density and then expanded them toward the target density. Both compression and expansion were stage wise processes in which each stage consisted of a 5000 steps of energy minimization followed by a 100 ps of MD simulation in NVT ensemble at 800 K. The expansion/compression process was performed in a stepwise fashion by imposing a sudden change in volume on the system in each step. Equilibration on the expanded/compressed system was done using the NVT ensemble. Starting from 50% of the target density, we compressed each simulation cell 15% of the target density in five steps until the density was 125% of the target density. Afterward, we expanded the simulation cell in five steps with each step with 5% reduction in density till the target density was reached.

3. After annealing, each cell was cooled in a step wise process. Starting from 800 K, each cell was cooled down by 10 K and MD simulation was carried out for 100 ps in a NVT ensemble. At the final step of each simulation, a snapshot has been saved as relaxed chain at that temperature. This step wise process repeated down to 200 K. As the goal of this section is to produce an initial structure at each temperature, the system was cooled as slowly as possible where the time constant of thermostat (which controls the velocity of cooling) was chosen to be 5 ps which is higher than normal 0.2 ps used in production simulations.

4. Upon generation of the relaxed structures at each temperature, each simulation cell went through a compression, in a NPT ensemble, to reach equilibrium. We considered several properties of the system (energy, specific volume and solubility parameter) as criteria for equilibrium. The equilibration time for different temperatures varied

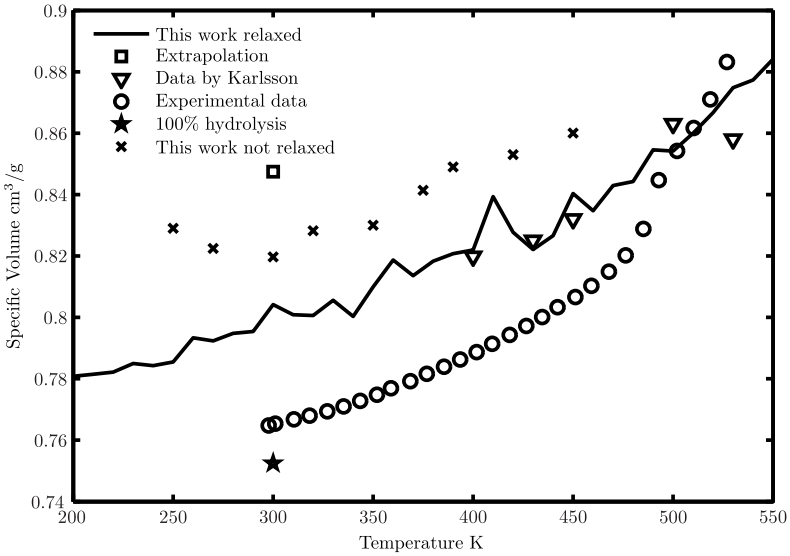

Figure 5.2: Comparison of specific volumes of PVA from different works. Data for 100% hydrolysis retrieved from [73].

between 60 to 100 ns.

5.3 Results and Discussion

5.3.1 Effect of Equilibration

To demonstrate the effect of the high temperature annealing on the simulation results, we also simulated the same atactic PVA chains without annealing and compared their properties with those of annealed ones. Figure 5.2 for instance compares the specific volumes of the PVA with and without high temperature relaxation at different temperatures. It is obvious that the computed specific volumes with the high temperature relaxation are lower (i.e., closer to the experimental values) than those without (see [75]). As shown in Figure 5.3, the fast relaxation can be attributed to higher number of torsional transitions and less number of hydrogen bonds at higher temperatures. The comparison to the data of other researchers shown in the Figure 5.2 will be discussed in detail in the specific volume section.

Note that the annealing procedure is also critical for polymer/solvent systems. It is believed that solvents act as plasticizer and help polymer chains to relax faster. To put that on test, we repeated the work of Wu [63] with and without annealing. Annealing was done after the addition of water. These systems include 20 wt% water at different temperatures. We used the TIP4P [76, 77] model for water to have comparable results with those of Wu. The results are shown in Figure 5.4 along with data reported by Wu [63][1]. As you can see even in the presence of 20 wt% of water relaxed systems adopted

For summary of the sensitivity analysis done on the system see Appendix E

[1]Wu reported in his work that there was a problem using OPLS-AA original partial atomic charges for

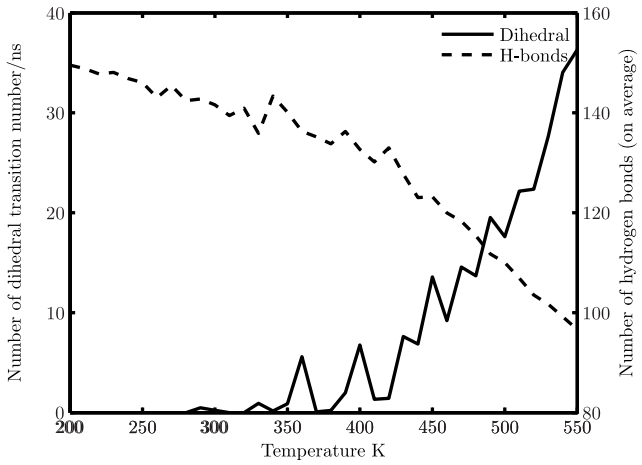

Figure 5.3: Comparison of number of dihedral transition (for the whole chain) and average number of hydrogen bonds (for the whole chain) at different temperatures. The hydrogen bonding definition (acceptor-donor distance and angle) is from [51].

lower specific volumes and the oscillation below the T_g vanished. Note that the effect of water as plasticizer was pronounced in the reduction of time required for system to reach equilibrium which was 30 ns. So it can be concluded that annealing of the chains can affect the volumetric properties of the polymeric systems even in the presence of plasticizers, especially at $T < T_g$.

5.3.2 Effect of System Size

There is no doubt that molecular simulation results are size dependent. Usually larger systems are required to reduce the size effects. In the current study, there are two ways to increase the size of the system. One is to increase the number of chains in the simulation box while the other to use a single chain with high degree of polymerization (DP). We calculated the solubility parameters using both approaches to identify the optimal size of the system for the calculation of other properties.

Table 5.1 summarizes the calculated solubility parameters for systems with different sizes. It is obvious that chains with 400 monomers yield results that are closer to the experimental values. All other smaller systems yielded results that are significantly higher than the experiment. Also, it was observed that systems with higher DP showed lower fluctuations in density which has been reported previously by Rigby and Roe [78]. These

simulation of the PVA and partial atomic charges of the COMPASS force field was used. But as we did not find any problem using the original OPLS-AA charges, we did all simulations with the original partial atomic charge values given by the OPLS-AA. To compare our results with those of Wu, we have also simulated all systems using the partial atomic charges from the COMPASS force field as well. According to our results, both set of charges yielded the same average value for density. The only difference observed was a slightly more fluctuations associated with the density when the COMPASS charges were used. Also it came to our attention that using the COMPASS charges, there was a 10% reduction in number of hydrogen bonds in the system.

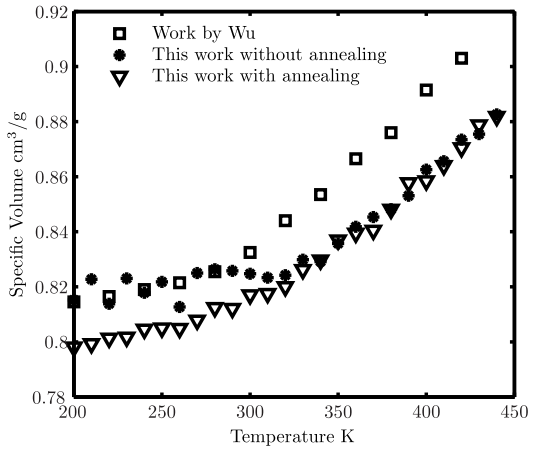

Figure 5.4: Specific volumes of the PVA/water mixture (20wt% water)

results indicated that one chain of DP400 yielded reliable statistics. The other concern was the value of the cut-off distance itself (1 nm is the value that are mostly used by other researchers). But it has been suggested in the literature that in some cases, the Coulombic potentials may not converge (e.g. see [79–81]). To estimate the effect of the conventional 1 nm cut-off distance which has been implemented in most of the simulation literature of PVA, we have simulated 10 different atactic DP400 systems with two longer cut-off distances (1.1 nm and 1.5 nm). We found that the effect on average density was not significant (except slightly less fluctuations) and solubility parameter was changed less than 0.7% for systems with cut-off of 1.1 nm. Increasing cut-off to 1.5 nm did not improve the results. In other words, a cut-off distance of 1 nm seems to be sufficient.

Table 5.1: Solubility parameter for systems with different size at 300 K

Tacticity	n[a]*DP[b]	δ[c] (MPa)$^{0.5}$	Cut-off (nm)	NIC[d]
Atactic	1*50	31.1±0.9	0.6	10
Atactic	4*50	29.3±0.4	1	1
Atactic	8*50	29.2±0.3	1	1
Atactic	1*200	28.7±0.3	1	5
Atactic	1*400	25.0±0.1	1	5
Isotactic	1*50	30.6±1.2	0.6	10
Isotactic	1*400	27.3±0.2	1	5
Syndiotactic	1*50	28.9±0.4	0.6	10
Syndiotactic	1*400	26.4±0.1	1	5

[a] Number of chains.
[b] Degree of polymerization.
[c] Solubility parameter. Its experimental value for PVA is 25-26 (MPa)$^{0.5}$ [73].
[d] Number of initial configurations.

5.3.3 Specific Volume

Following the annealing protocol and recommendations from previous sections, we have simulated PVA chains (DP400) for 100 ns after complete equilibration. Specific volumes for all stereomers of PVA at different temperatures are plotted in Figure 5.5. Despite minor differences below the glass transition temperature (see section 5.3.5 for more discussion), which is 350 K, specific volumes of chains with different tacticities showed no significant differences. Isotactic and syndiotactic chains show slightly lower specific volumes than the atactic chains below the glass transition temperature. Radial distribution functions of oxygen atoms in the system (not shown) did not show any sign of crystallization in the systems. Accordingly, differences in specific volumes of stereomers are not attributed to difference in crystallinity. A likely explanation is the difference between their hydrogen bonding capabilities and/or intrinsic local order in the isotactic and syndiotactic chains due to their all head-to-tail connectivities.

Average specific volume of all stereomers has been plotted in Figure 5.2 along with experimental data reported by Walsh and Zuller [74] and data reported by Karlsson et al. [47] at elevated temperatures (using the force field parameters developed by Muller et al. [48]). As can be seen, specific volumes at higher temperatures show a good agreement with experimental data while at lower temperatures significant deviations are apparent. The deviations are partly due to the absence of crystalline phase and are more pronounced below the melting temperature. It is worth noting that the simulation times used were not long enough to allow crystallization to occur. It is known from experiment that density of the PVA (g/cm^3) correlates with its degree of crystallinity as follows [5]:

$$\rho = 1.269 * (\frac{1.345}{1.345 - 7.6 * 10^{-4} * (crystalinity\%)}) \tag{5.1}$$

The above equation along with the absence of crystalline phase in the simulation systems explains the overestimation of the specific volume below the T_m.
Karlsson et al. [47] without annealing obtained much higher values for specific volume in the first attempt using parameters developed by Muller et. al [48] (not shown). To get better estimation of the specific volume, they reduced the size of oxygen atoms in the system and their reported value has been shown in Figure 5.2. As you can see, our data are comparable with their reported value (there is no significant difference between OPLS-AA force field parameters and those reported by Muller et. al originally). Also, using the linear functionality of the specific volume and inverse of number of monomers, first reported by Leute et al. [82], Rossinsky et al. [6] extrapolated the specific volume of PVA from DP=10 to infinite chain length at 300 K. Their result shows 6% error with respect to experimental data and 4% comparing to our values. This simply means that using the linear functionality suggested above overestimates the specific volume while using longer chains one can obtain much smaller values.

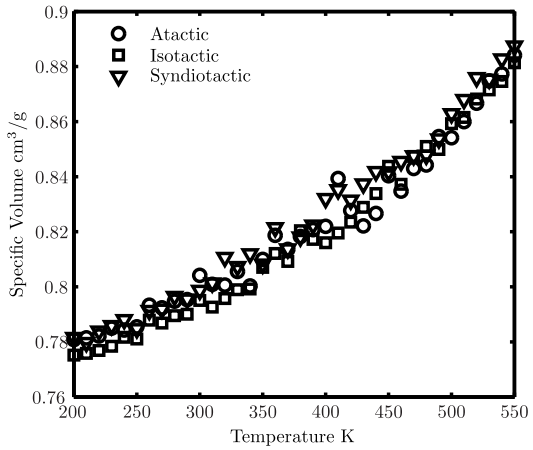

Figure 5.5: Comparison of specific volumes of PVA with different tacticities

5.3.4 Thermal expansion coefficient

Having the specific volumes over a broad range of temperatures, it is possible to calculate the thermal expansion coefficient of PVA. The volume expansion coefficient is defined as:

$$\alpha = \frac{1}{V_0}(\frac{\partial V}{\partial T})_P \tag{5.2}$$

where V, T and P are volume, temperature and pressure of the box respectively and V_0 is a reference volume. At each temperature calculated specific volume has been used as V_0 at that temperature. Assuming an isotropic system, linear coefficient of thermal expansion is 1/3 of the volume expansion coefficient. Calculated values of α and its average experimental values has been shown in Figure 5.6. These values show great agreement with experimental data reported in [73] which is direct results of using long enough chain along with appropriate force field parameters.

5.3.5 Glass Transition temperature

Using temperature dependency of specific volume (Figure 5.7), we have estimated glass transition temperatures for PVA with different tacticities to be 350 K which has great agreement with experimental values reported. Experimentally, T_g of PVA has been reported to be in the range of 325.5 to 375 K [72, 73, 83–86] depending on sample used and experimental procedure applied. In the process of calculation of T_g (see Figure 5.7) specific volume data was grouped into three parts that correspond to three temperature ranges. The first two parts are related to glassy and rubbery regions and the data in the highest temperature range was excluded to identify the T_g. Note that sudden jump in thermal expansion coefficients,

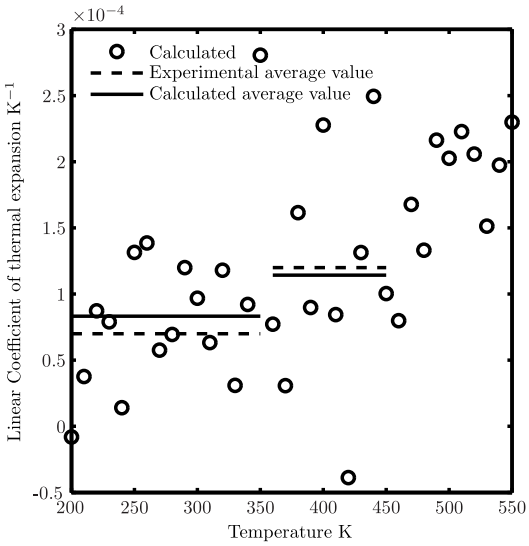

Figure 5.6: Coefficient of linear thermal expansion of PVA

as plotted in Figure 5.6, shows this transition better. The only simulation result on T_g of PVA, that the authors are aware of, is reported to be 385 K by Pan et al. [52].

Using the specific volume data for PVA/water mixture (20 wt% water), we also calculated the glass transition temperature of the mixture to be 320 K and 290 K for non-relaxed and relaxed systems. The difference between the two systems agrees with our expectation that the annealed systems show lower glass transition temperatures (see [75]). One the other hand, adding a plasticizer, water, reduces the T_g comparing to pure PVA which has been reported both experimentally [87] and by simulation [63] previously. The experimental value for T_g of this mixture has been reported to be 233 K [88].

5.3.6 Solubility Parameters

One of the basic properties of polymers that has been usually used to predict the compatibility of polymer blends and solutions is the Hildebrand solubility parameter. The solubility parameter of a polymer is defined as the square root of its cohesive energy density in the amorphous state at room temperature [73]. The easiest way to measure the cohesive energy density is based on the enthalpy of evaporation of the material. But, as polymers cannot be evaporated, indirect methods have been used [73]. Unfortunately, these experimental methods are difficult to control and results vary depending on the experimental procedures.

The basic method for the calculation of the solubility parameter (see [89]) is based on the calculation of the cohesive energy density from MD trajectories and application of equation

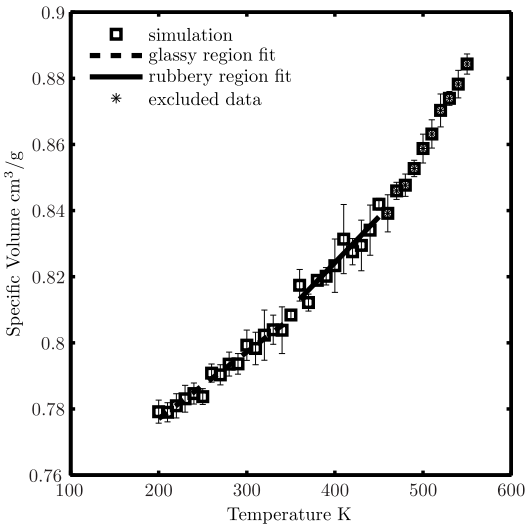

Figure 5.7: Temperature dependence of specific volume of PVA, averaged over different tacticities.

5.3:

$$\delta = \sqrt{\frac{\Delta E}{V}} \tag{5.3}$$

But to obtain accurate results, some care should be taken in the calculation of the cohesive energy from MD trajectories. The change in cohesive energy is defined as the difference between the non-bonded energy in the condensed and gas phases. Here, the calculation of the non-bonded energy in the gas phase, as Choi et al. mentioned in their work [90], can cause a problem as conformations of polymer chains in the gas phase are different from those used in the condensed state. To overcome this problem, we applied the procedure proposed by Belmares et al. [57] and just considered those conformations in the gas phase which have happened in the liquid phase simulation. Accordingly, we have calculated the solubility parameter using equation 5.4:

$$\delta = \sqrt{\frac{\sum_{i=1}^{n} \langle E_i^k - E_c^k / n \rangle}{N_0 \langle V_c \rangle}} \tag{5.4}$$

Where in this equation N_0 is Avogadro's number, V_c is the volume of the box, n is the number of molecules in the box, E_i is the energy of the polymer chain in the gas phase, and E_c is the non-bonded energy of the system in the condensed phase. The parameter k represents different components of the non-bonded potential energy and can be used to separate the components of the Hildebrand solubility parameter to Hansen solubility parameters, if needed. The only difference between our method and the method of Goddard et al. is that all production simulations has been done in NPT ensemble instead of NVT. The reason for this is, as Choi et al. [89] mentioned, to capture the energy changes due

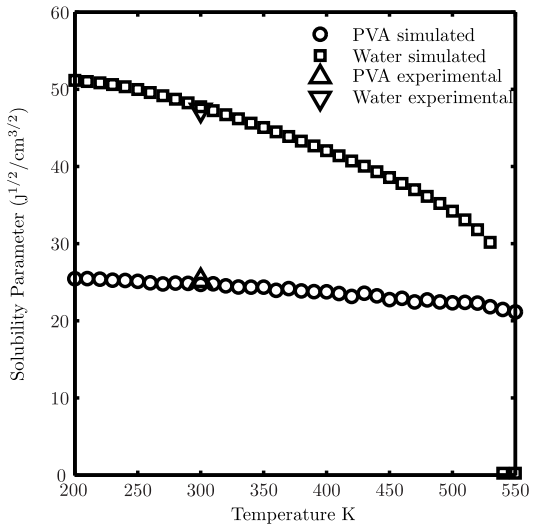

Figure 5.8: Comparison of computed Hildebrand solubility parameters of PVA with those of water.

to thermal expansion at different temperatures. Also this way, V_c can be directly obtained from simulation results and no priori experimental data will be necessary.

Figure 5.8 shows the calculated values of the solubility parameters of PVA and water (TIP4P). As you can see, the calculated solubility parameters for both PVA and water are in good agreement with experimental data at 300 K. Karlsson et al. [47] calculated the solubility parameter of PVA chains to be 22.5 $(\text{MPa})^{0.5}$ at 300 K while our value, 25 $(\text{MPa})^{0.5}$, is in good agreement with experimental values of 25-26 $(\text{MPa})^{0.5}$ [73]. This difference is partly due to the difference in force field parameters and chain lengths between the two works and more importantly the relaxation of the chains. It is unclear whether Karlsson et al. relaxed their model chains prior to production simulation. Given that solubility parameter decreases with increasing chain length of a polymer [73], and that the chain length used in the work of Karlsson et. al was 145 monomers, the value reported by them would have been lower if they had used longer chains in their work.

As expected, with increase of temperature the solubility parameter of both water and PVA decrease [73] and this is more pronounced in the case of water (For effect of degree of hydrolysis on Hildebrand solubility parameter see appendix C). The reason for this is that higher number of hydrogen bonds in water weaken as temperature increases. Experimentally, it is known that PVA and water are miscible at temperatures around 370 K and higher. But direct comparison of the Hildebrand solubility parameter for them does not confirm this, as the difference is very high even at very high temperatures. The more elaborate way to assess the compatibility is via the Flory-Huggins interaction parameters

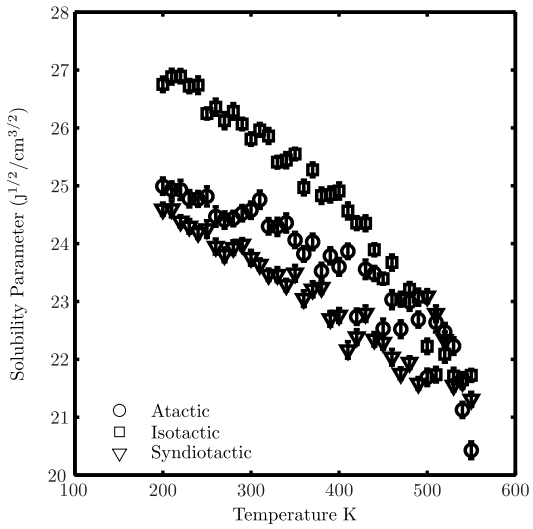

Figure 5.9: Computed Hildebrand solubility parameters of PVA with different tacticities.

which will be discussed in detail in our upcoming publication.

It is known that solubility of PVA in water varies with its tacticity. Experimental results indicate that partially syndiotactic chains are usually less soluble in water than isostatic chains and highly syndiotactic chains are almost insoluble in water [91]. The atactic chains usually show solubility parameters between isotactic and highly syndiotactic chains [5]. Comparison of solubility parameters of PVA stereomers in Figure 5.9 shows that MD results are consistent with this observation qualitatively as the isotactic chains have higher solubility parameters (more soluble in water) and atactic chains have middle solubility parameters while purely syndiotactic chain shows lowest solubility parameter. But as we mentioned before Hildebrand solubility parameter is not a good measure of solubility for system with hydrogen bonding capability and further analysis using the Flory-Huggins interaction parameter is required.

5.3.7 Heat capacity

Heat capacity, a measure of the required energy to increase the temperature of a unit amount of material, can be directly calculated from MD simulation with two different approaches. In the first method, a system is simulated at several different temperatures and heat capacity can then be calculated as the ensemble (time) average of change in total energy of the system with respect to temperature as shown in the following equation [24]:

$$C_V = \langle \frac{dE}{dT} \rangle_V \tag{5.5}$$

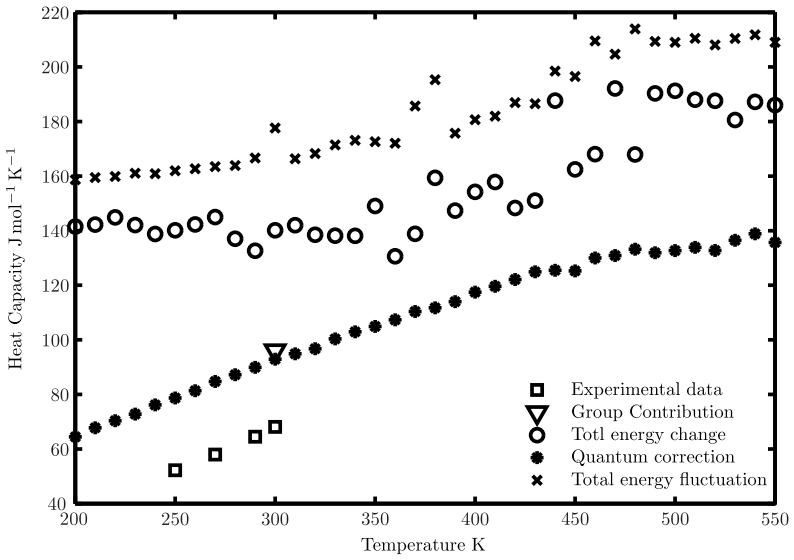

Figure 5.10: Heat capacity of the PVA. Experimental values from [73]. Note that the heat capacity of the polymers is conventionally reported per monomer.

where C_V is the constant volume heat capacity, E is the total energy of the system and T is absolute temperature. The other direct method for the calculation of heat capacity using MD data involves the use of energy fluctuations at constant temperature which is formulated as follows [24]:

$$C_V = \frac{\langle E^2 \rangle - \langle E \rangle^2}{k_B \langle T \rangle^2} \tag{5.6}$$

where k_B is the Boltzmann's constant. Note that as the value of the PV is negligible compared to total energy (incompressible material), the enthalpy and internal energy are almost identical and so the C_V and C_P. The heat capacity calculated using equations 5.5 and 5.6 is shown in Figure 5.10. Comparing to the experimental values reported for PVA, it is clear that both methods dramatically overestimate (a factor of 3) the heat capacity.

The above results are somewhat expected. Apart from statistical issues, there is a more profound reason (which both low and high molecular weight liquids share) for the overestimation of the heat capacity. In such complex systems, there are some relevant quantum effects involved that should be included in the calculations [92]. Berens et al. were the first researchers who considered these quantum mechanical effects in MD simulation [45]. They have developed a method to systematically calculate the thermodynamic properties using quantum harmonic oscillator approximation for every degree of freedom in the system. This assumption works well for solids, e.g. see [93]. According to the authors [45], the velocity spectrum of a molecular system is defined as:

$$S(\nu) = 4\pi\beta \sum_{j=1}^{3N} m_j \langle D[V_j(t)] \rangle \tag{5.7}$$

Where:

$$D[V_j(t)] = \frac{1}{2\pi} \lim_{\tau \to \infty} \left| \int_{-\tau}^{\tau} dt \exp(-i2\pi\nu t) V_j(t) \right|^2 \tag{5.8}$$

and the heat capacity (constant volume) can be calculated using the quantum harmonic oscillator approximation as follows:

$$C_v = k_B \int_0^{\infty} d\nu S(\nu) W(\nu) \tag{5.9}$$

where the quantum correction weight function, W, is:

$$W(\nu) = \left(\frac{u^2 e^u}{(1 - e^u)^2} \right) \tag{5.10}$$

in which u is:

$$u = \beta h \nu \tag{5.11}$$

and $\beta = 1/k_B T$ and h is the Planc's constant.

However, applying the method to glass forming liquids (like PVA) is not very suitable. Nonetheless, we have applied this method to calculate the heat capacity of the PVA and the results are shown in Figure 5.10. These results are based on 100 ps simulation of well equilibrated systems with a time step of 0.1 fs (for detail see [94, 95]). This result indicates that including the quantum correction strongly improves the prediction over the classical methods but the problem of overestimation still exists. As you can see at 300 K, value calculated using the method of Berens et al. coincide with the group contribution theory prediction[71, 73]. So the values of the C_P reported in Figure 5.10 can easily be used for prediction of the heat capacity of the PVA chains with different degrees of polymerization at different temperatures up to the group contribution accuracy. Our calculations showed that contribution of each monomer to the total density of state (DOS), regardless of its position on the chain, is almost identical. Another interesting fact is that the change in slope of the C_P Vs. T is strongly correlated with number of dihedral transitions shown in Figure 5.3. The slope is reduced around the 450 K where vibrations of the dihedral angles are taken over by free rotations.

Surprisingly, there exist no significant differences in the heat capacity of PVA with different tacticities. This is because the heat capacity is mainly related to the degrees of

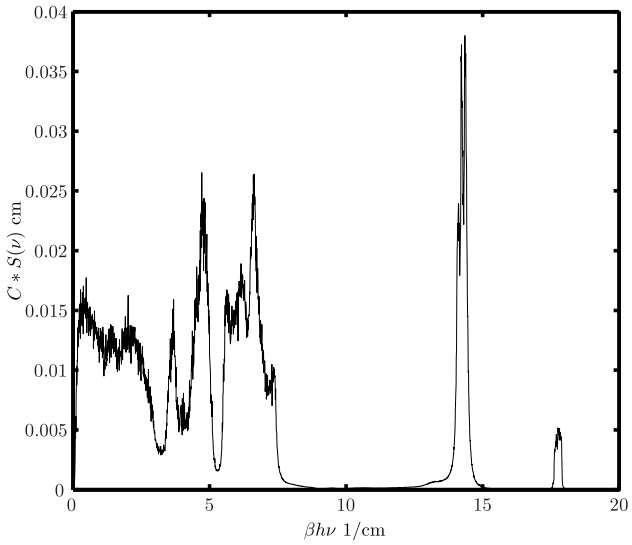

Figure 5.11: Velocity spectrum of one monomer of PVA (averaged over all monomers). Vertical axis is C (speed of light) multiplied by the DOS and the horizontal axis is the frequency scaled by βh

freedom of vibrations which are identical in all types of chains.

Recently Goddard et al. [94, 95] introduced the so-called two phase thermodynamic (2PT) model, which is a modification of the method of Berens, to obtain better estimation of the DOS for the glass forming liquids. In this method, the DOS of liquids is divided to two distinct portions of gas and solid like. Accordingly, the heat capacity is estimated by applying the method of Berens et al. to the solid like portion of the DOS. This method has been successfully applied to several different systems, including Lennard-Jones particles [94] and real liquids of low molecular weights [95, 96], without significant deviations from experimental values [96]. The main idea of this method is based on the analogy of the DOS at low frequency to that of gas like materials. Unfortunately, in the case of the high molecular weight polymeric systems, the correction calculated via 2PT model is negligible as the zero frequency motion of the monomers (their self-diffusion coefficient) is very small as can be seen in Figure 5.11 (refer to [94, 95] for the details of calculations). As zero frequency DOS is related to the self-diffusion coefficient of each monomer, we tried to estimate its value from self-diffusion value obtained from 500 ns trajectories but failed (as original 100 ps trajectories are too short to capture monomers self-diffusion). It seems that the 2PT correction for polymer segments is negligible. This means that the way the gas phase DOS is estimated should be changed to remove its exclusive dependency on zero frequency DOS. Otherwise, a totally new approach is required.

5.4 Conclusion

The high temperature annealing seems to generate representative conformations of PVA. Using the OPLS-AA force field allowed us to reproduce experimental specific volume of the PVA over the temperature range of 200 to 550 K. As crystallization is a slow process and could not be mimicked in the MD simulation, no crystallization was observed. The simulation also provided good predictions of the solubility parameters and the glass transition temperature of PVA. It is noteworthy that the glass transition temperature of PVA is insensitive to its tacticity in MD simulation. We showed that for high density PVA classical methods overestimate the heat capacity. We used the quantum correction to obtain better estimation of the heat capacity. We showed that the 2PT method is not applicable to the PVA and a new method is needed to correct the quantum effects for polymeric materials. Comparing the properties of the different PVA stereomers, it has been found that they show differences in their solubility parameters but share the same specific volume, thermal expansion coefficient, glass transition temperature and heat capacity.

Chapter 6

Free energy of solvation and Force field modification

6.1 Introduction

Poly(vinyl alcohol) (PVA) and its blends with other polymers and composites filled with fibers are found in numerous technological applications[2–5, 7]. To process the materials, solvent is usually needed. Water is the only known practical solvent for PVA but it only works over a limited range of temperatures. Solvent mixtures containing a significant amount of water are also used[97]. Despite the presence of the hydroxyl moiety, both vinyl alcohols (e.g., ethanol) and carboxylic acids (e.g., acetic acid), are known to be immiscible with PVA[98]. This implies that identifying new solvents for PVA based on the idea of matching chemical functional groups is not as fruitful as one might expect. Nevertheless, being able to find solvents other than water is desirable for some applications of PVA in which PVA involves in reactions to form water-insoluble derivatives[97].

Owing to the cost and time consuming nature of experimental procedures, molecular dynamics (MD) simulation seems to be a cost effective, viable alternative to design solvents of interest[53, 57, 99–104]. It is well-known that accuracy of the MD simulation is mostly dictated by the quality of the force field used. A well parameterized force field can accurately reproduce experimental measurements in a much efficient fashion. Needless to say, before doing any extensive simulations on any polymer/solvent sets, checking the accuracy of the force field adopted is an essential step.

Most of the known properties of PVA are attributed to its strong hydrogen bonding network[2–4, 6, 48, 53, 56, 87, 88, 105–114]. Obviously, introducing solvent molecules into the polymeric matrix will disturb such network. Interactions between PVA and solvent

A modified version of this chapter has been accepted for publication in Journal of Molecular Modeling:"Effect of partial atomic charges on the calculated free energy of solvation of poly(vinyl alcohol) in selected solvents"

molecules are affected by both the size of the solvent molecules (breaking hydrogen bonds) and the ability of the hydrogen bonding network to accommodate the solvent molecules. For example, in the case of water, its small size and strong hydrogen bonding capability are both in favor of mixing. Keeping this in mind, an accurate prediction of the hydrogen bonding interactions in any PVA/solvent systems is crucial.

In the context of MD, hydrogen bonds are usually handled through the Coulombic interaction. As a result, partial atomic charges (PACs) become the tuning parameters. To have an accurate prediction of the hydrogen bonding interaction, a set of well-tunned PACs are required. The process of tuning PACs in a force field is not a trivial task even for small molecules[25, 115, 116]. A common practice for developing a force field for polymers is to optimize the PACs to reproduce key properties of small molecule analogs[25] and then to extend the results to the corresponding polymeric systems. However, there is no guarantee that the optimized PACs based upon the small molecule analogs are able to reproduce the properties of the polymers where conformation and tacticity also play a major role [117]. Accordingly, in this work, we replaced the empirical optimization of PACs by using quantum mechanically derived electrostatic potentials fitted to selected point charge models[116].

There exist several conventional methods that can be used to derive PACs directly using the electron density obtained from ab initio calculations [118]. To select the best PAC set for PVA, we have benchmarked the free energy of solvation (FES) for PVA oligomers in selected solvents calculated from MD simulation using PAC sets obtained from various point charge models against the ab initio calculated values (for flowchart of calculation steps see figure 6.1). To capture the effect of tacticity, we have repeated the calculations for long enough PVA oligomers with different tacticities (atactic, isotactic and syndiotactic). Solvents used in this study were water, ethanol and benzene. They were chosen as they have different sizes and hydrogen bonding capabilities. In this work, we retrieved all bonded and non-bonded parameters except PACs from the original OPLS-AA force field. As in our previous work [119] we showed that the OPLS-AA force field can reproduce properties of PVA in its pure state reasonably well. Effects of chain conformation and tacticity [117] on the PACs were studied in this work. Here, we identified a set of PACs for PVA which can reasonably predict the interactions between PVA and the selected solvents. Another major contribution of this work is the identification of a point charge model for the calculation PACs compatible with the OPLS-AA force field for similar systems when proper values are missing.

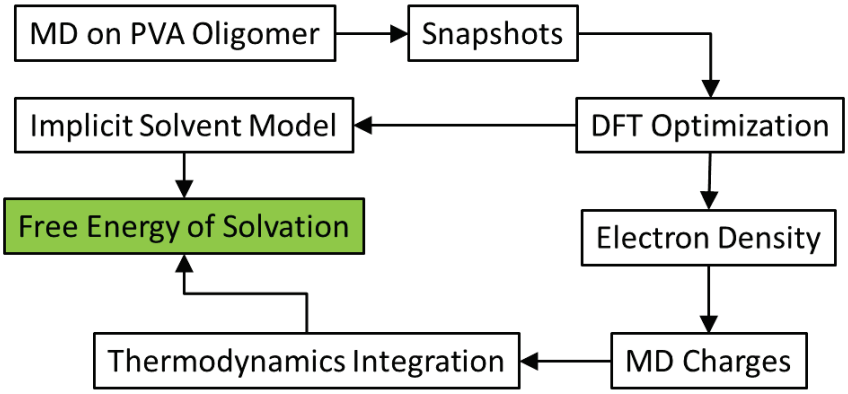

Figure 6.1: Flowchart of calculation steps for validation of the partial charges.

6.2 PVA oligomers

All oligomers used in this study had 10 repeating units capped with two methyl groups. This size was selected as a compromise between the computation cost of ab initio calculations and capturing the tacticity effect without any significant end effects. All calculations in this study repeated for isotactic, syndiotactic and atactic PVA (with 50% chance of chiral center inversion). Similar to previously reported work [68], all monomer connectivities are head-to-tail.

To create the required structures for calculations, a chain with the tacticity of interest was created using the Amorphous Builder module in Materials Studio 5.01 [67] at very low density (vacuum). In the next step, this chain went through a geometry optimization using the original OPLS-AA parameters in GROMACS to remove close contacts, if any. This was followed by an equilibration MD simulation in vacuum at 400 K. Finally, a short,5 ns, simulation at 400 K in vacuum was performed on the chain and snapshots were saved every 100 ps (a total of 50 different snapshots saved for each chain). All ab initio and MD calculations were repeated for every snapshot created here to capture the effect of conformational changes on the calculated properties as per the method of [120, 121]. For the calculation of FES at the ab initio level, an implicit solvent model (see the section on the Calculation of FES) was used. At the MD level, each oligomer was mixed with 1000, 400 and 231 molecules of water, ethanol and benzene, respectively, in a three-dimensional periodic box. These numbers were determined by trial and error to keep number of solvent molecules and the system size effect on the calculated FES at the minimum simultaneously.

6.3 ab initio Calculation

6.3.1 Calculation of PACs

For all ab initio calculations, we used the Gaussian09 package [41] and the level of theory used was UB3LYP/6-31G* [42]. It was used previously in the calculation of partial atomic charges used in the AMBER force field [115, 116] but is different from that (RHF/6-31G*) used in the development of the original OPLS-AA force field [25]. Having the basis set (energy) converged for a molecular system, a few selected population analysis methods were used to calculate the PACs. In this study, we used the Mulliken Population Analysis (MPA)[122], Natural Population Analysis (NPA)[123], Merz-Singh-Kollman (MSK) [43, 44], Atoms In Molecules (AIM) [124] and Hirshfeld [125–128] methods. All aforementioned methods are incoporated in the Gaussian09 package except the AIM method that we used the "Bader Charge Analysis" code [115] for the post processing of the data. It is worth mentioning that to obtain accurate results, cube files generated by Gaussian09 were exported with fine meshing. In addition, as other researchers suggested [118], we used 2,000 points for each atom when the MSK scheme was used. The following summarizes the procedure for the calculation of PACs.

- First, PACs were calculated for all snapshots created by the 5 ns MD simulations in vacuum. The level of theory for this calculations was UB3LYP/6-31G*. Note that it has been reported that PACs calculated using UB3LYP/6-31G* are very close to the results of high quality ab initio calculations[118]. These values will be used to discern the effect of geometry optimization.

- Then, using the same level of theory, all snapshots have been geometry optimized in vacuum and PACs were calculated for these optimized structures.

- Finally, each oligomer (snapshot) was solvated in implicit solvent (either water, ethanol or benzene) using the Polarizable Continuum Model using the integral equation formalism variant (IEFPCM)[129] method. Then, using converged basis sets in implicit solvent environment, PACs were calculated again.

The SCF convergence criteria were set to 10^{-n} for the root mean square changes in the elements of the density matrix between two successive cycles with n being 8 for the calculation of SCF energies, gradients and second derivatives. The criteria for the convergence of the geometry optimization were set as follows; 0.00045 and 0.0003 ($E_\mathrm{h}\, {a_0}^{-1}$) for maximum force and the root mean square of the forces, respectively; 0.0018 and 0.0012 (a_0) for the maximum displacement and the root mean square of displacements, respectively.

6.3.2 Calculation of free energy of solvation

For the calculation of free energy of solvation, the IEFPCM method available in the Gaussian09 package was used. For the topological model we used the UAKS which has been obtained from united atom topological model applied on radius optimized for the PBE1PBE/6-31G* level of theory. The electrostatic scaling factor was chosen to be 1.2 as suggested by Wen et al.[130]. The free energy of solvation was calculated simply by subtracting the free energy of each oligomer in vacuum from that in the solvated state. Solvents considered for this work were water, ethanol and benzene. Note that as Wen et al. [130] previously mentioned and our results confirmed, the geometry optimization in the solvated state is not necessary as changes in both geometry and energy are insignificant.

6.4 Molecular dynamics simulation

In this work, we used GROMACS 4.5.5 [58–62] for carrying out all MD simulations. We used the OPLS-AA force field [25] to describe the intra and intermolecular interactions of ethanol, benzene and PVA except the PACs of PVA. For water molecules, the TIP4P model developed by Jorgensen et al. [76, 77] and SPC [131] models were used while all bonds were constrained using the SHAKE algorithm [132] unless otherwise stated.

In all simulations, the Berendsen thermostat/barostat [20] with a time constant of 0.2/1 ps were used to control the temperature/pressure of the simulation box. FES at MD level was calculated at 300 K. Given the short length of the oligomers and plasticization effect of the solvent, this temperature was enough to capture essential conformational changes of the oligomers although there is a high chance of missing conformations with high energy barriers [133, 134]. Newton equations of motion were integrated using the leap-frog algorithm [135] with a time step of 2 fs along with a sampling time of 1 ps. The cut-off distance of the non-bonded interactions was set to 1.1 nm and the Particle Mesh Ewald (PME)[136] method was used for handling the long range Coulombic interactions. The long range dispersion energy and pressure corrections were applied to retrieve the correct density values of the systems.

6.4.1 Slow-growth calculation of the free energy of solvation

For the calculation of FES via MD simulation, we have used the slow-growth coupled with the thermodynamic integration method in the GROMACS package. This method requires a simulation during which the Hamiltonian of the system changes slowly from state A, a solvated chain, to that describing the pure solvent, state B. The required modification of the Hamiltonian, H, is realized by making H a function of a coupling parameter

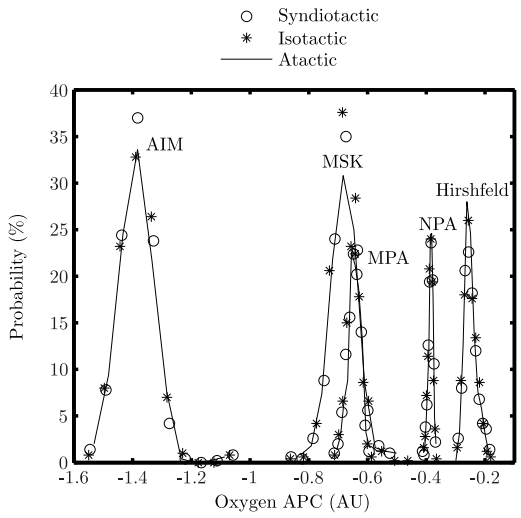

Figure 6.2: Probability distribution of the PAC of the oxygen atom in PVA with different tacticities as calculated by different population analysis methods.

λ:$H = H(p, q; \lambda)$ in such a way that $\lambda = 0$ describes state A and $\lambda = 1$ describes state B. It is known that the change in the system, between states A and B, must be so slow that the system remains in equilibrium [23]. Accordingly, the path between states A and B has been split to 201 intermediate states for proper sampling. These steps are related to gradual removing of the Coulombic and vdW interaction of the chain from the Hamiltonian, each of them in 100 steps (for a typical graph of changes in free energy see the appendix G). At each step, we simulated the system for 1 ns to obtain proper sampling of the conformational changes in the chain. After determining the Hamiltonian, the total free energy change was then calculated by the Multiple Bennett's Acceptance Ratio (MBAR) [27].

6.5 Results and discussion

6.5.1 Atomic partial charges

We collected a total of 292,500 PAC data points for all the systems in this study. Upon careful analysis such data, several interesting facts emerged and are summarized as follows:

- PACs on the monomers are independent of their positions in the backbone. Therefore, PAC for each atom was averaged over all atoms of the same type in all monomers and over 50 snapshots (i.e., an average over 500 PAC values for each atom). Figure 6.2 shows the distribution of the PACs for the oxygen atom as calculated using different population analysis methods before the geometry optimization. As one can see, the distribution is rich enough to produce meaningful averages for each method and tacticity of interest.

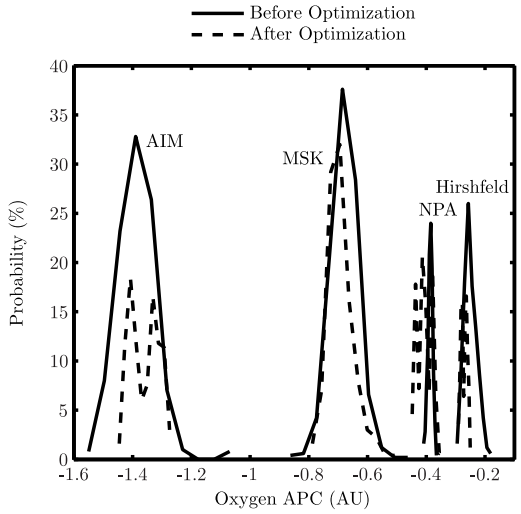

Figure 6.3: Probability distribution of the PAC of the oxygen atom in isotactic PVA as calculated with different methods.

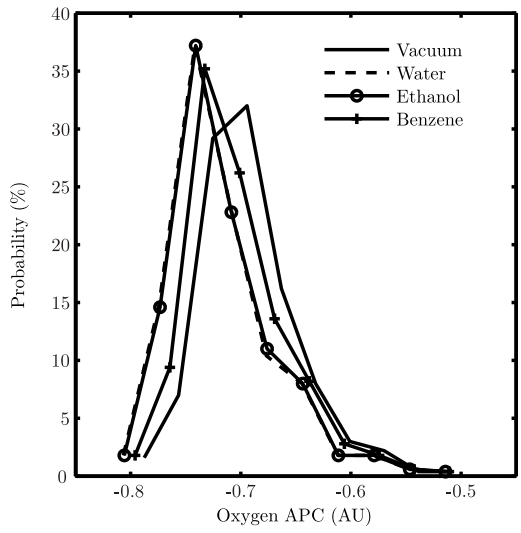

Figure 6.4: Probability distribution of the PAC of the oxygen atom in solvated isotactic PVA as calculated by the MSK method.

- Since the snapshots were taken directly from MD simulations, this means that atomic positions were not at the lowest energy state. Figure 6.3 compares the PACs before (Figure 6.2) and after geometry optimization. Here, MPA results are not shown for better clarity. As can be seen, all PAC distributions shift slightly. Also, except the MSK method, all other methods show multiple peaks which make determining a unique PAC for each atom more complicated. This observation occurs to other types of atoms too. While MPA results are not sensitive to the geometry optimization, the maximum relative change in the average values of other methods were around 40% except NPA (500%). We believe that by a short energy minimization of snapshots at the MD level (keeping the dihedral angles constrained to avoid any change in the chain conformation) the computationally expensive step of ab initio geometry optimization could be bypassed.

- Comparing the PACs for atoms in oligomers with different tacticities revealed that there was no significant differences between calculated PACs. This holds true for all values before and after optimization and even the solvated systems. Based on this result, we can confidently conclude that all the differences between PVA with different tacticities is attributed to their different hydrogen bonding networks and not by any difference in their hydrogen bonding strength.

- In Figure 6.4 we have compared the PACs for the oxygen atoms in isotactic PVA in vacuum and in three different solvents as calculated by the MSK method. As it has been reported before [130], our results indicate that there is a minor shift in the PACs in solvents compared to those calculated in the vacuum (the degree of shift is correlated with the polarity of the solvent). Likewise, the same trend was observed for other calculated PACs (for detail of the deviations from PACs of optimized structures in vacuum, see the appendix F). While the sensitivity of PACs from all methods are around 10% (relatively), the AIM results showed 125% change respect to optimized values in vacuum. But as environment dependent parameters are not practical for MD simulations and average values are not that different, in this work we used the optimized PACs and ignored the solvent effect.

Table 6.1: PACs of PVA calculated using different population analysis methods. Note that after averaging the data small changes (third significant digit) has been made in the values for some atoms to make the sum of the PACs for each monomer zero. For the corresponding standard errors of values reported here, see Table F.2 in the appendix F

Atom	OPLS-AA	MPA	NPA	MSK	AIM	Hirshfeld
H[a]	0.06	0.149	0.029	0.081	0.019	0.039
H[a]	0.06	0.149	0.029	0.081	0.019	0.039
H[a]	0.06	0.149	0.029	0.081	0.019	0.039
C[a]	-0.18	-0.447	-0.087	-0.243	-0.057	-0.117
H[b]	0.06	0.14	0.027	0.116	0.02	0.042
C1	-0.12	-0.296	-0.063	-0.418	-0.008	-0.054
H[b]	0.06	0.144	0.027	0.109	0.021	0.042
C2[c]	0.205	0.132	0.107	0.51	0.726	0.112
H	0.06	0.131	0.017	-0.005	0.012	0.045
O	-0.683	-0.657	-0.271	-0.7	-1.353	-0.408
H[d]	0.418	0.406	0.156	0.388	0.582	0.221
H[e]	0.06	0.149	0.03	0.128	0.024	0.042
H[e]	0.06	0.149	0.03	0.128	0.024	0.042
H[e]	0.06	0.149	0.03	0.128	0.024	0.042
C[e]	-0.18	-0.447	-0.09	-0.384	-0.072	-0.126

[a] Starting methyl group-Carbon connected to C1
[b] Connected to C1
[c] Connected to O
[d] Connected to O
[e] End methyl group-Carbon connected to C2

Based on the above discussion, we selected the PACs calculated for optimized structures in vacuum as representative of each method. Since differences between PACs of different tacticities are negligible, we considered the same PAC set for all stereoisomers where PACs were averaged over all three tacticities. Table 6.1 shows the final partial charges for each method which were used in the MD simulations. In agreement with previous studies [118], our results show that predictions by the AIM method for the oxygen atom in the hydroxyl group are exaggerated. On the other hand, predictions by the MSK method is moderately damped while the NPA's predictions lies in between of the other two methods. The interesting fact here is how the PACs of the OH group calculated via the MPA and MSK methods are close to those of the original OPLS-AA force field. However, the PACs of both carbon atoms in the PVA monomer calculated from the MSK method are significantly different from the original OPLS-AA force field.

As mentioned before, properties of PVA are mostly dictated by its hydrogen bonding network (or the Coulombic interactions). So, any change in the PACs of the PVA can cause drastic changes in the PVA's properties. Accordingly, following the procedure presented in our previous work [119], we calculated the properties of pure PVA looking for effect of PACs. In Figure 6.5 densities of isotactic PVA at different temperatures calculated using different sets of PACs are shown. The results confirm that values calculated using the MPA and MSK methods are very close to the OPLS-AA predictions. This is not sur-

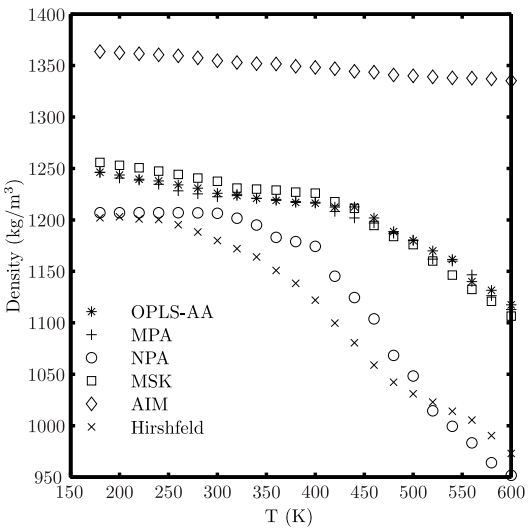

Figure 6.5: MD results for density of pure isotactic PVA as a function of temperature calculated using different PAC sets.

prising, as it was reported before that PACs calculated using the MSK method are more successful than other methods[118]. Also note that how over estimation of the PACs of the OH group by AIM method causes a dramatic overestimation of the density. Both NPA and Hirshfeld methods underestimate the PACs of the hydroxyl moiety, thereby the density.

In the formulation of the OPLS-AA force field, the non-bonded interactions between atoms connected by 3 bonds (1-4 interactions) are considered with a fudge factor of 0.5. So any change in the PACs of the back-bone carbon atoms of PVA can change the dihedral angle distribution and therefore, the chain's conformation. In Figure 6.6, the dihedral angle distribution for the back-bone carbon atoms of an isotactic PVA chain with 400 monomers is shown. Despite the significant difference in the PACs of carbon atoms calculated by the MSK method with respect to the original OPLS-AA values, the dihedral angle distributions are in good agreement (see the appendix F for the comparison of the other methods). Note that the minor deviation in the gauche+ can be easily removed by a slight change in the parameters of the Ryckaert-Belleman potential. This trend, close proximity of the MSK results with those of OPLS-AA, holds true for other properties of the PVA (data not shown).

6.5.2 Free energy of solvation

FES calculated via MD simulations need to be validated by comparing with proper experimental estimations. As no experimental data is available for current hypothetical oligomers, we calculated the FES using accurate ab initio calculations by applying the implicit solvent model[129, 130]. To capture the effect of conformational changes [117], FES was calculated

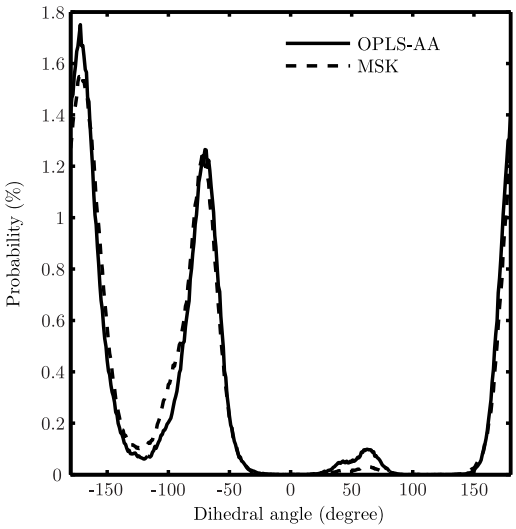

Figure 6.6: Comparison of back-bone carbon atoms dihedral angle distribution of an isotactic PVA chain with 400 monomers determined by the original OPLS-AA and MSK PACs. Results were averaged over all possible dihedral angles in a 5 ns MD simulation on a well relaxed chain in a NPT ensemble at 300 K and 1 bar.

for all snapshots of each tacticities (see appendix G). For averaging the FES over all snapshots, data were weighted by a Boltzmann factor[117]. This is necessary as all snapshots were generated at very high temperature (500 K) and the results are about to be compared with values calculated at 300 K in MD simulations. So, averaged values for ab initio calculations shown in the first part of Table 6.2 were calculated as follows:

$$\langle \Delta E_{solvation} \rangle = \langle E_{sol} \rangle - \langle E_{vac} \rangle = \frac{\sum_{i=1}^{N} E^i_{sol} e^{-\frac{E^i_{sol}}{k_B T}}}{\sum_{i=1}^{N} e^{-\frac{E^i_{sol}}{k_B T}}} - \frac{\sum_{i=1}^{N} E^i_{vac} e^{-\frac{E^i_{vac}}{k_B T}}}{\sum_{i=1}^{N} e^{-\frac{E^i_{vac}}{k_B T}}} \tag{6.1}$$

where N is the number of snapshots; $\Delta E_{solvation}$ is the FES. E_{sol} and E_{vac} are the absolute ab initio calculated energy of the oligomer in the solvated state and vacuum, respectively; k_B is the Boltzmann constant and T is the absolute temperature here set to 300 K. For the detail of the regular averaged values, readers are referred to the appendix G. Based on the results, such short PVA oligomers were thermodynamically miscible with all three solvents as the negative value for the FES indicates. While the solvation in solvents with polar groups (water and ethanol) is highly exothermic, the heat released in the case of benzene is significantly lower. Note that the fact that these oligomers are miscible with benzene and ethanol is not in contrast with the fact that PVA macromolecule is not miscible with these solvents. Oligomers used in this study were very short and miscibility of such

short oligomers has been reported before in the case of PVA with molecular weights less than 10000 (g/mol) [109]. Comparing the FES for oligomers with different tacticities shows that there is no significant difference, another indication that differences between difference stereoisomers of PVA comes from topological differences between their hydrogen bonding network and not conformational differences.

Using the PAC sets developed in previous section we calculated the FES for each oligomer using the MD simulation coupled with the slow-growth method. As each structure evolves during the MD simulation there is no need to repeat this calculation for each snapshot (we repeated a couple of simulations using 5 different initial structures and the results did not show any deviation). Calculated FESs are shown in Table 6.2. As it was mentioned before in the case of PACs and ab initio calculated FESs, MD calculated FES exhibited no significant difference between PVA oligomers with different tacticities in water. Accordingly for other solvents, the simulations were limited to isotactic oligomers.

Table 6.2: Summary of the calculated FES ($kJ\,mol^{-1}$) of PVA oligomers in selected solvents. The maximum estimated error for MD calculated FES was less than 2%. For the distribution of the ab initio calculated FES, see the appendix G.

		Solvent		
Method	Tacticity	Water	Ethanol	Benzene
Ab initio	Ata	-158.3	-149.5	-63.1
	Iso	-155.9	-147.9	-63.9
	Syn	-148.0	-138.3	-56.9
OPLS-AA	Ata	-160.7	-	-
	Iso	-169.3	-169.2	-125.7
	Syn	-159.4	-	-
MPA	Ata	-179.2	-	-
	Iso	-182.2	-168.6	-128.9
	Syn	-180.8	-	-
NPA	Ata	1.1	-	-
	Iso	0.1	-76.0	-89.4
	Syn	0.0	-	-
MSK	Ata	-157.8	-	-
	Iso	-164.5	-156.6	-86.7
	Syn	-154.7	-	-
AIM	Ata	-698.7	-	-
	Iso	-699.6	-526.8	-173.5
	Syn	-740.0	-	-
Hirshfeld	Ata	-34.4	-	-
	Iso	-36.1	-90.1	-101.6
	Syn	-36.6	-	-

A quick comparison of the MD results with ab initio results reveals that the predictions by NPA, AIM and Hirshfeld PAC sets deviate significantly from the expected values. On the other hand, the predictions by the MPA and original OPLS-AA PAC sets are reason-

able for PVA oligomers solvated in water and ethanol. But both PAC sets exhibited poor prediction for the benzene case. Further, our results suggest that FES calculated by the MSK PAC set gives the best prediction of oligomers solvated in all three solvents with less deviation in the case of benzene. To ensure that water model and the system size do not affect the results, we repeated the calculation using the SPC water model and systems with more solvent molecules. Our results confirm that in all cases, FES deviates no more than 1% with respect to the values reported here. This insensitivity of the FES to the water model used has been reported previously [137] for drug like molecules.

It is interesting to note that PACs calculated by the MSK scheme are in such great agreement with the OPLS-AA force field and also can predict the solvation energy of PVA in three different solvents even better than using the OPLS-AA PACs. Nevertheless, to check if this holds true as a general rule, such calculations should be repeated for an extended list of solvents and other macromolecules. If successful, the cumbersome task of assigning the PACs to new molecules will be replaced by a series of short and affordable ab initio calculations. In the near future, we will present a comprehensive study on several other polymers and will extend the list of solvents to evaluate the robustness of the approach presented in this work.

6.6 Conclusion

To asses the quality of the PACs of PVA used in the original OPLS-AA force field, we collected a rich data set on PACs for short chain PVA oligomers using different conventional population analysis schemes. Our results confirmed that PACs are very sensitive to the initial structures in most of the cases and geometry optimization before PAC calculations is necessary (either at MD or ab initio level). While the sensitivity of the PACs to tacticity of the oligomers was not significant, they showed slightly different values in different solvents. Among all PAC data sets, values of the MSK and MPA schemes were closer to those of the original OPLS-AA force field, and this was reflected in the properties of the pure PVA too. Based on the ab initio results, the FES of PVA oligomers in water and ethanol was lower than those in benzene which is a direct results of hydroxyl groups available in those solvents. While the MD calculated FES using PACs calculated by MPA scheme showed great agreement with values predicted by original OPLS-AA parameters, both showed great deviation for FES of oligomers solvated in benzene. However, use of PACs obtained from the MSK scheme yielded FES values that showed better agreement with ab initio calculated values even in the case of benzene.

Chapter 7

Dynamic of solvent in PVA matrix

7.1 Introduction

Poly(vinyl alcohol) (PVA) is a versatile polymer. Owing to its non-toxic and non-carcinogenic characteristics and ease of processing, PVA is found in a variety of applications in science and engineering. Major applications include its use as textile sizing and finishing agents, emulsifiers, photosensitive coatings, adhesives for paper, wood, textiles and leather, and barrier films for food packaging [4]. It has also been frequently found in biomedical applications such as contact lenses, lining for artificial hearts, and drug delivery devices.

To optimize the performance of PVA in many of the aforementioned applications, a molecular level understanding of the diffusion behavior of low molecular weight substances, water in particular, in PVA is crucial. Given the difficulties associated with studying diffusion at the molecular level experimentally, molecular simulation does provide a viable alternative. For the PVA/water system, there exist quite a few of such studies using molecular dynamics (MD) simulation [106, 111, 138, 139]. However, such studies used different force fields, chain lengths of PVA, simulation times, concentrations of water and temperature ranges. This makes drawing a general conclusion on the diffusion behavior of water in PVA rather difficult. Therefore, in this study, we used a force field that has been shown to be suitable for PVA [119] and a very long PVA chain under a wide range of temperatures and concentrations to ensure the reliability of the data. We then used the resultant MD data to interpret a previous observation of Zhang et al. [2] in their study on a pervaporation separation process in which they found water diffusivity increases with increasing water concentrations while the corresponding mean free volume decreases. At first, this result seems to be counter intuitive according to the free volume theory but a detailed analysis of the free volume redistribution dynamics would reveal the underlying reason.

A modified version of this chapter was published as an invited paper to a special issue of Chemical Engineering Science (In Press) to showcase molecular simulation work done in the chemical engineering community in light of the 2013 Noble Prize of Chemistry being awarded to three chemists who developed a variety of molecular simulation methods: Effect of free volume redistribution on the diffusivity of water and benzene in poly(vinyl alcohol)"

There are different classes of predictive models for the estimation of self-diffusion coefficients of small molecules in polymers. For a great review on these models, readers are referred to [140]. Among all of these models, the Mackie-Meares model, a simple lattice based model, shows an exceptional ability to predict water diffusivity in PVA as reported by Muller-Plathe [3]. The Mackie-Meares model is shown as follows:

$$\frac{D_{S,1}}{D_{0,1}} = \left(\frac{1-\phi}{1+\phi}\right)^2 \tag{7.1}$$

where ϕ is the volume fraction of the polymer in the system and $D_{S,1}$ and $D_{0,1}$ are the self-diffusion coefficient of the penetrant in the mixture and pure state, respectively. Muller-Plathe stated that the Mackie-Meares equation works well when the nature of intermolecular interactions are alike (e.g., polar penetrant and polar polymer or vice versa) but not for systems containing components interacting with dissimilar intermolecular interactions (e.g., PVA and benzene). However, we will show that the prediction of the model can be poor even for the PVA/water system at low temperatures and/or low water concentrations. And the reason for the failure of the Mackie-Meares model essentially stems from the size fluctuations of the free volume holes as they redistribute in the system.

In the first part of this work, we will show the computed self-diffusion coefficients of water and benzene from MD to validate the simulation protocols and force fields used. We will then use the self-diffusion coefficients of water and benzene in PVA along with the corresponding free volume data to analyze the underlying diffusion mechanisms of the penetrants.

7.2 Molecular dynamics simulation

In this work, we used GROMACS 4.5.5 [58–62] for carrying out all MD simulations. We used the OPLS-AA force field [25] to describe the intra and intermolecular interactions of PVA and benzene. For water molecules, the TIP4P model developed by Jorgensen et al. [76, 77] was used while all bonds were constrained using the SHAKE algorithm [132].

In all simulations, the Nose-Hoover thermostat [21] with a time constant of 0.2 ps and the Parrinello-Rahman barostat [65] with a time constant of 2 ps were used to control the temperature and pressure of the simulation cell, respectively. A temperature range of 270 to 370 K was used, as pervaporation separation is usually operated near the boiling temperature of water [3] while all biomedical applications are at 310 K. Also, use of such a wide range of temperatures allowed us to elucidate the effect of temperature on the diffusion mechanism. In terms of the concentration, we considered the range from 1 wt% water (where all the separations are believed to happen in the pervaporation process) to 20 wt%

water (swelling of polymer matrix by water in drug delivery devices).

Newton equations of motion were integrated using leap-frog algorithm [135] with a time step of 1 fs and a sampling time of 1 ps. The total production simulation time after full equilibration was on average around 100 ns. Readers are referred to our previous work [119] for the procedure for the generation of the initial structures and the equilibration criteria. The cut-off distance of the non-bonded interactions was set at 1 nm and the Particle Mesh Ewald (PME) method was used for handling the long range Coulombic interactions. The long range dispersion energy and pressure correction was applied to retrieve the correct density of the system, as previously mentioned by Wu [63].

Single chain PVA models were used and the PVA chain was atactic with the head-to-tail connection, as it is the major stereomer of PVA produced by the hydrolysis of poly (vinyl acetate) [5, 68]. The PVA chain contained 400 monomers and two methyl end-groups (i.e., the corresponding molecular weight was 17,630 $\mathrm{g\,mol^{-1}}$). Accordingly, simulation cells, each containing a single PVA chain, were built with appropriate numbers of penetrant molecules to obtain the required concentrations (wt%). Concentrations of interest here were 1, 3, 5, 10, 15 and 20 wt%.

7.3 Determination of free volume

To study the effect of free volume on the diffusivity of the penetrants, two major characteristics of free volume were determined, namely statistical and frequency changes. To calculate free volume, there are two methods currently used in the literature. The first option is the probe method (i.e., the Connolly surface analysis). This has been recently used by Zhang et al. [2] for calculating the mean fractional free volume of the PVA/water system. The more sophisticated method is based on the concept of Voronoi tessellation of the space. It enables one to determine the free volume associated with each penetrant molecule independently [141–143] as it is defined in the original free volume theory. The diffusional motion of a penetrant molecule in a polymer matrix is mainly influenced by its local free volume, not by the mean free volume per penetrant molecule as determined by the Connolly surface analysis. One implication of defining free volume by the Voronoi tessellation method is that there is no free volume when there are no penetrant molecules. Nonetheless, Greenfield and Theodorou used such an approach for their work on determining the diffusion pathway in glassy and melt polypropylene [144]. As the computational cost of this method is much less than the probe method, one can apply it to a series of consecutive frames to obtain the evolution of free volume as a function of time. Having this rich information, it increases our ability to analyze the dynamics of free volume that is not possible with the use of the probe method. For the three-dimensional tessellation of space, we used the VORO++ code

[145].

7.4 Results and discussion

For detailed analysis of PVA/solvents density and glass transition temperature please refer to appendix D.

7.4.1 Solvents' self diffusion coefficients

Figure 7.1 shows the self diffusion coefficients of water and benzene ($D_{0,1}$) over the temperature range of 270 to 370 K along with the available experimental data. Obviously, the results obtained using the selected force field are in reasonably good agreement with experiment and the deviation is less than 5% for both liquids. In the case of water, the overestimation is attributed to the system size considered here (500 water molecules). The computed activation energy (By fitting Arrhenius law on the temperature dependency of self diffusion coefficients) for self-diffusion of water is 13.9 $\mathrm{kJ\,mol^{-1}}$ while that of the experimental data shown in Figure 7.1 is 17.5 $\mathrm{kJ\,mol^{-1}}$. Activation energy values of 18.5 to 20 $\mathrm{kJ\,mol^{-1}}$ [3, 70] based upon MD data (short simulation time) have also been reported where Tamai et al. [70] slightly underestimated the activation energy (see Table 7.1). But in the case of benzene, the deviation of the self-diffusion coefficient is slightly higher. This is result of the system size (100 benzene molecules) and simulation time (100 ns) used. The other reason for the deviation is that the benzene molecules do not adopt a planar structure which has been reported previously [146]. The activation energy calculated in this work is 26.4 $\mathrm{kJ\,mol^{-1}}$ while the two sets of experimental data shown yield values of 13.3 and 12.5 $\mathrm{kJ\,mol^{-1}}$, respectively. The discrepancy is due to the fact that the activation energy of this work covers a wide range of temperatures while those from the experimental data mainly derived from the high temperature region. Given that the computed self-diffusion coefficients of benzene changes slope around 300 K, it is possible to split the data set into two regions. And the corresponding activation energy values for the low and high temperature regions will then be 38 and 18.7 $\mathrm{kJ\,mol^{-1}}$, respectively. It is clear that the result of the high temperature region is in line with experiment. Nevertheless, for the sake of consistency, we will use our calculated self-diffusion coefficient data of the pure penetrants, instead of experimental data, for comparison purpose in section 7.4.5.

7.4.2 Self-diffusion of water in PVA

In Figure 7.2, we compare our self-diffusion coefficient ($D_{S,1}$) results of water in PVA with those reported by Muller-Plathe [3]. As can be seen, our results are about one order of magnitude smaller than those of Muller-Plathe. This is because we used the TIP4P model

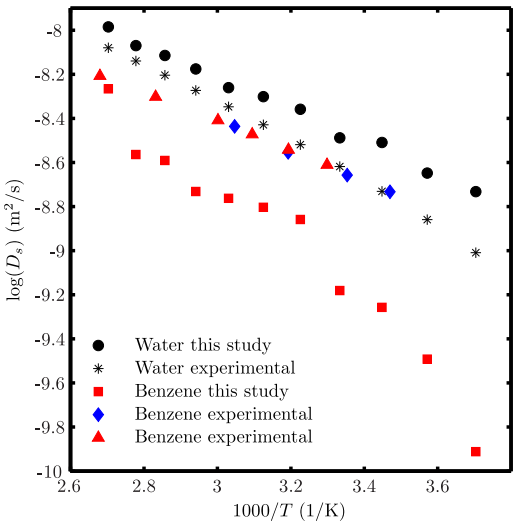

Figure 7.1: Computed self diffusion coefficients of water and benzene. The experimental data for water are from [147] while those for benzene [148] and [149].

for water, a more effective hydrogen bonding model, and all-atom force field for PVA that includes realistic geometrical obstruction by considering explicit hydrogen atoms. In addition, considering the shorter chain length and simulation time adopted by Muller-Plathe, the difference was totally expected. In Figure 7.3 we compare our results at 20 wt% water at different temperatures with values reported by Wu [63] at 21 wt% water. As there are no significant differences between the respective works (small differences in chain lengths and partial charges used), the self-diffusion coefficient values are in good agreement especially at elevated temperatures. And both sets of values at low temperatures are within the error range of experimental values reported. It is known that diffusion coefficients calculated using MD simulation are affected by size of the system considered [150]. Accordingly, we have conducted a similar analysis introduced by Yeh et al. [150] and found that the size of the system used in this work was sufficient.

In Table 7.1 we show both the experimental and simulation data on self diffusion for the PVA/water system under different conditions that we could find. Since most of these data are single point data, there is no point to compare them in a graph with our data. Accordingly, we compared them one by one and did not find any significant discrepancies (extrapolation was required for some data points). Nevertheless, our results and those of Karlsson et al. [7] do not agree and their reported values are much higher than ours from extrapolation to 502 K using the calculated activation energies (see Table 7.2). In addition, the calculated density of PVA in the work of Karlsson et al. is much lower than what we reported previously [119]. It seems that all observed differences are attributed to different force fields used in the respective works.

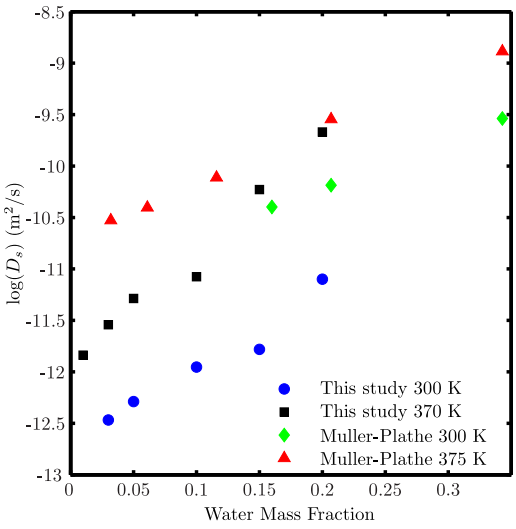

Figure 7.2: Comparison between the computed self diffusion coefficients of water in PVA at different water concentrations from this study and those of Muller-Plathe [3, 98]. Results of Muller-Plathe were obtained from using the SPC model for water and a short simulation time of 20 ns.

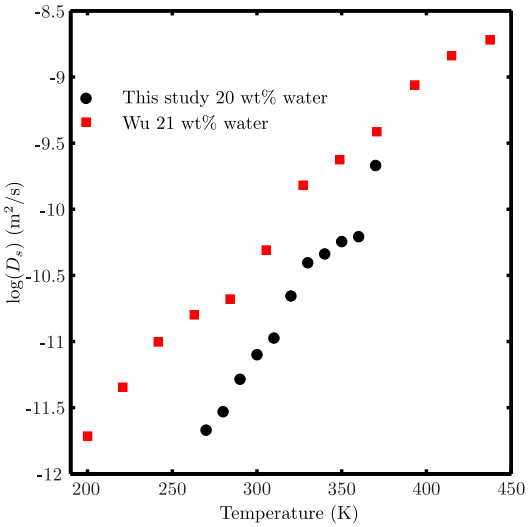

Figure 7.3: Comparison between the computed self-diffusion coefficients of water in PVA at 20 wt% of water at various temperatures in this study and those of Wu [63].

Table 7.1: Reported values for self-diffusion coefficient of water and its activation energy in the PVA.

T (K)	$D_{s0} * 10^{10}$ (m^2/s)	E_a (kJ/mol)	Reference
370-400	2.8-42	167.97	[151][b]
298	0.1-10	-	[108, 152][c]
510	36	50	[153][d]
298	0.1-0.24	-	[154][e]
502	1-1.78	-	[7][f]
200-400	0.63-63	18-20	[70][g]
200-420	0.015-18.2	15 and 32.4[a]	[63][h]
300	4.8-130	-	[2][i]
300	1.9-15.6	-	[2][j]
502	9.5	-	[7][k]
502	21	-	[7][l]

[a] Below and above the T_g
[b] Infinite dilution using inverse gas chromatography
[c] 0.5-7.5 wt% water
[d] MD with low water content
[e] Vapor phase sorption on cross linked PVA at relative humidities of 0.38-0.74
[f] MD at 2.6-5.2 wt% water
[g] MD simulation at 50 wt% water
[h] MD at 21 wt% water
[i] Sorption on systems containing 18-46 wt% solvent (water and ethanol)
[j] MD on systems containing 18-46 wt% solvent (water and ethanol)
[k] 2.6 wt% water
[l] 5.2 wt% water

According to Zhang et al. [155], the diffusion coefficient of water in PVA, in the presence of a small amount of ethanol, was a linear function of the degree of swelling induced by the water. We observed a similar phenomenon at very high water contents that were close to the water contents used in the work of Zhang et al. But analysis of the concentration range studied here indicated that the functionality at low water contents is exponential as it is often reported in literature [152, 153]. The reason is a sharp increase in the diffusional

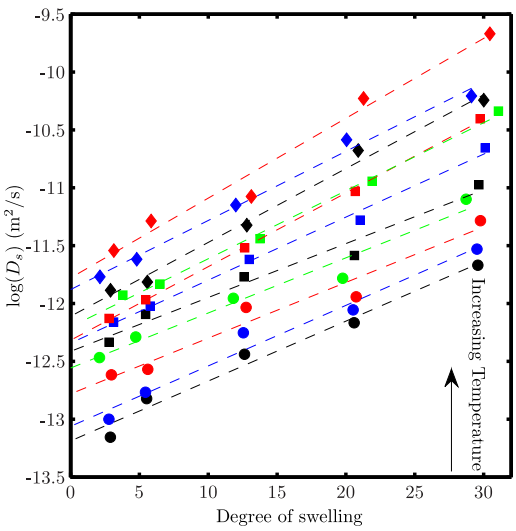

Figure 7.4: Self diffusion coefficients of water in PVA as a function of the degree of swelling. The degree of swelling is defined as: $\rho_{PVA}/\rho_{Mixture} - 1$.

parameters caused by significant changes in the polymer mobility by adding solvent (reduction in T_g). Figure 7.4 shows the diffusion coefficients of water in PVA. According to the free volume theory and work of other researchers (e.g. see [108, 152]), diffusion coefficient shows an exponential functionality with the degree of swelling (or water content). Although the fits of some data points seem not so good, one noteworthy point is that the slope of the fitted lines seems to be insensitive to temperature. The average slope of the fitted lines is 0.056 ± 0.015. Note that these lines cannot be extrapolated to very low water contents as it has been shown experimentally that there is a sudden decrease in the values at very low water contents (in the log scale plot)[108].

Having the self-diffusion coefficient data over a range of temperatures allowed us to calculate the activation energy of the diffusion for water at different water contents. Figure 7.5 shows the temperature dependence of self diffusions coefficients as well as lines fitted to calculate the activation energy of diffusion. Table 7.2 summarizes the calculated activation energy and the corresponding literature values. According to Zielinski and Duda [156], the activation energy of diffusion should decrease with increasing solvent content in polymers [156]. As can be seen in Table 7.2, the activation energy for systems containing 1 to 10 wt% of water follows this prediction. In contrary, activation energy value increases considerably from 10 to 15-20 wt%. This is very likely due to the decrease in the glass transition of the system. As Wu [63] reported before, the activation energy of water diffusion in PVA at 21wt% of water underwent a sudden change passing the glass transition temperature. And they reported values of 15.0 and 32.4 kJ mol^{-1} for temperatures below and above T_g, respectively. The value for the rubbery region is in good agreement with our values for 15

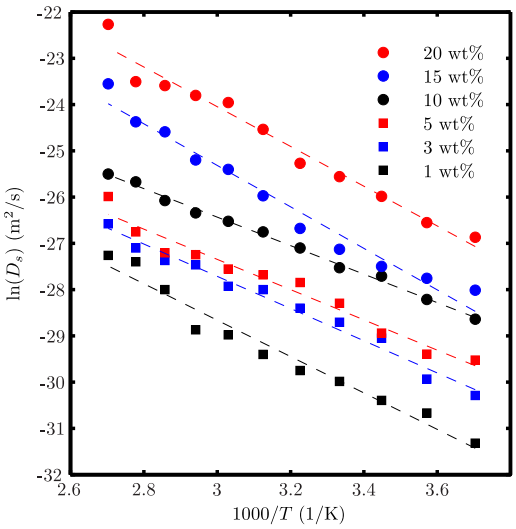

Figure 7.5: Temperature dependence of self diffusion coefficient of water in PVA.

and 20 wt% of water in our systems.

Table 7.2: Summary of the activation energy of water diffusion in PVA at different water contents.

Water Content (wt%)	E_{act} (kJ/mol)
1	32
3	29
5	27
10	26
15	37
20	36

7.4.3 Self-diffusion of benzene in PVA

Due to its larger size and its inability to affect the hydrogen bond network of PVA, the self diffusion coefficient of benzene in PVA is about one order of magnitude lower than that of water. Accordingly, much longer simulation times (400 ns) was required to properly estimate the self diffusion coefficients. Also, by closely monitoring the mean square displacement curves of different benzene molecules, we excluded the data that had not yet reached the Einstein regime. As a result, the resultant values carry larger statistical errors compared to the case of water. The self diffusion coefficients of benzene in PVA containing

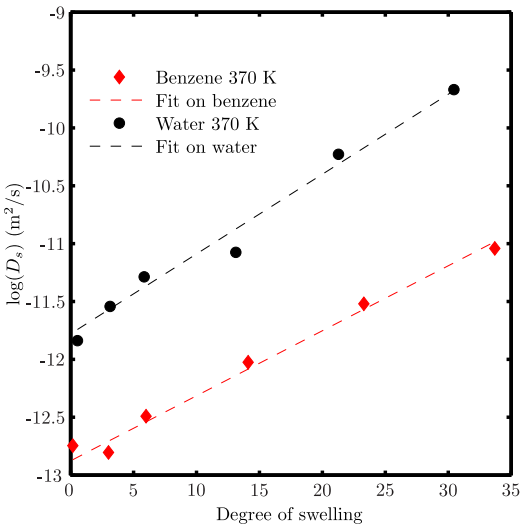

Figure 7.6: Self diffusion coefficients of water and benzene in PVA as a function of the degree of swelling.

20 wt% benzene are shown in Figure 7.6 along with the data for water at 370 K. Unlike the PVA/water system, experimental data on the PVA/benzene system is scarce. The only experimental data we could find is $0.25 * 10^{-12}$ m^2/s at 323 K and 2.5 wt% of benzene as reported by Pan et al. [157]. Comparing their results at 320 and 300 K with our data $0.27 * 10^{-12}$ m^2/s at 370 K indicates that our data is well in the range of experimental data. Pan et al. [52, 157] also did MD simulation on the system and reported values of $1.55 * 10^{-12}$ m^2/s for the NVE ensemble and $1.05 * 10^{-12}$ m^2/s for the NVT ensemble under the same conditions. It is clear that their simulation results are an overestimation of their own experimental data. By using a larger system and a much longer simulation time, our values are in a better agreement with the experimental data of Pan et el. Using a coarse grained force field and a much longer simulation time, Gautieri et al. [158] reported a diffusion value of $0.263 * 10^{-12}$ m^2/s at 2.5 wt% for benzene in PVA and 300 K. Considering that coarse grained simulations are known to yield overestimation, our data at 370 K seems to be reliable. Figure 7.6 shows the dependence of the diffusivity of benzene on the degree of swelling of the PVA/benzene system along with data for water. Please note that at the same degree of swelling, the weight concentration of benzene is lower than that of water. In other words, at the same weight concentration, the PVA/benzene system contains more free volume holes than the PVA/water system. This is because there are lower intermolecular attractions between PVA and benzene (apolar) molecules comparing to the PVA/water(polar) system. Nevertheless, the self diffusion coefficients of benzene are significantly lower than those of water. This is attributable to the larger size of the benzene molecules making them more difficult to undergo diffusion jumps.

7.4.4 Effect of free volume redistribution frequency on water diffusivity

According to the original free volume theory [13], there requires a minimum (critical) free volume, a necessary condition, for successful diffusional jumps. This critical value in the original paper was considered to be about 10 times of the volume of the jumping (diffusing) molecule. Accordingly, the average free volume is not so important (either at a particular instant or averaged over a time period.). What is important is the availability of the minimum required free volume and its frequency of appearance. Figure 7.7 shows the normalized probability distribution for free volume per water molecule at different temperatures and water concentrations. As can be seen in the figure, by adding more water to PVA at constant temperature, the average free volume decreases which is consistent with the results of Zhang et al. [2]. Zhang et al. [2] mentioned in their work that with increasing water content, the fractional free volume decreases while the diffusion coefficient of water increases which is in contradiction to the free volume theory. Since the authors calculated the average free volume using the probe method, they were not able to explain the counter intuitive results. Further examination of Figure 7.7 reveals the reason for this observation. This figure shows that there exist long tails on the right hand side of the distribution at high water contents (magnified in Figure 7.8 for better resolution). Now, defining an arbitrary critical free volume value (say 10 times the size of water molecule), it is easily deduced that more holes with appropriate size are provided by the high water content systems while the average free volume of such systems is lower than that of the low water content systems. Figure 7.9 shows the averaged accessible free volume per water molecule and its standard deviation at the lowet and highest temperatures considered in this study. The figure clearly shows that the average/standard deviation consistently decreases/increases by adding more water to the system. In fact, such data was our first clue on this problem and led us to calculate the free volume probability distribution for further investigation.

Theoretically, even at low water contents, some water molecules would have access to the free volume holes with size larger than the critical free volume in some instances although data shown in Figure 7.15 does not show such behaviour due to limited time span. What causes the difference between low and high water content systems is the frequency of the occurrence of this favorable hole formation. When the water content is low, PVA is in the glassy state and its segments do not participate in free volume redistribution much. This can be easily seen in Figure 7.10, where the mobility of PVA segments is compared in the sense of mean square displacement averaged over all segments. For the systems with higher water contents, the mobility of the chain segments increases due to the plasticization effect of water, thereby enhancing the free volume redistribution. It is known that increasing water content increases the frequency and amplitude of polymer segment wiggling motion under isothermal conditions [153].

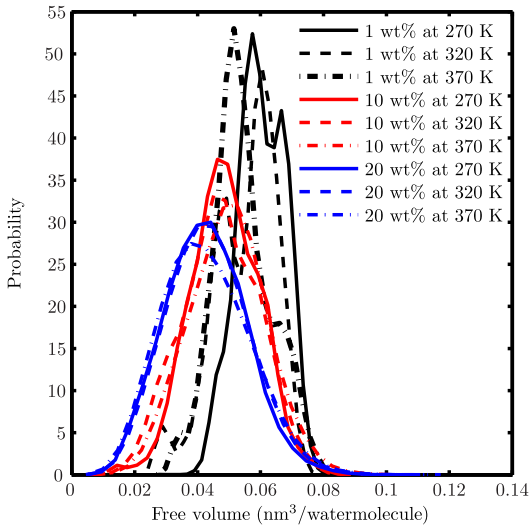

Figure 7.7: The normalized free volume probability functions of water in PVA at different temperatures and concentrations.

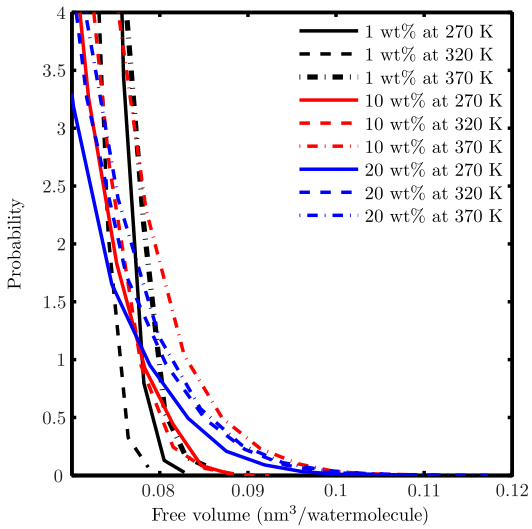

Figure 7.8: Tails of the normalized free volume probability functions of water in PVA at different temperatures and concentrations.

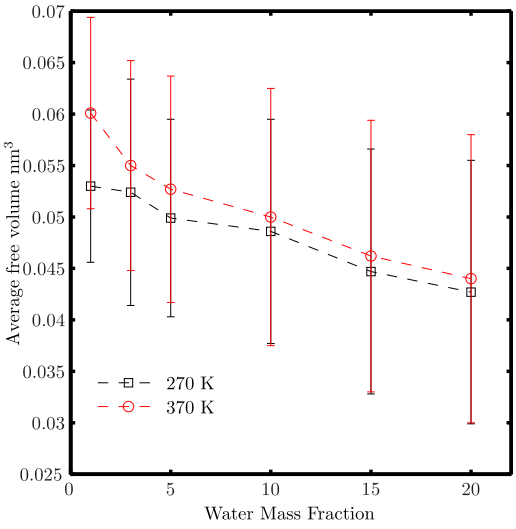

Figure 7.9: Average free volumes and their standard deviations per water molecule. The averages were obtained from the last 5 ns of the production simulation runs.

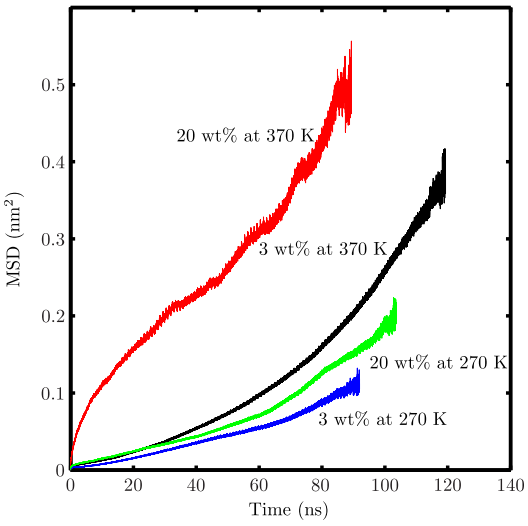

Figure 7.10: Mean square displacements of PVA segments at different temperatures and water concentrations.

Now, the question is how does the increasing mobility of polymer segments increase the chance of forming larger free volume holes? Answer to this question lies in the time evolution of free volume. In Figure 7.11, we compared the Fast Fourier Transform (FFT) of free volume (as we had access to free volume versus time for each water molecule separately) at different temperatures and water contents. It should be noted that the analysis was done on the last 5 ns of the trajectories. The data analysis needed to be done for each penetrant molecule individually at different temperatures and concentrations. Therefore, we had to limit our analysis to a practical time span. Our preliminary results indicated that a 5 ns span was enough to show the concept that we had in mind. For more accurate and smooth results, the analysis should be done on the entire trajectory of a production simulation. As can be seen in Figure 7.11(a), the high frequency changes in free volume are similar for low and medium water content systems while it is higher for high water content. By increasing temperature, 7.11(b) and 7.11(c), one can easily see that the behavior of the medium water content system approaches that of the high water content system while the low water content system shows no significant changes. What this really means is that high frequency redistributions of free volume holes are intensified by adding water. The faster the changes (i.e., higher intensity for high frequency changes) in free volume around a water molecule (with the collaboration of the polymer segments) take place, the higher the chance that low probability outcome like large free volume holes can be satisfied over a fixed time span.

To show that the increase in free volume redistribution frequency is not due to the formation of water clusters during simulation, we compare the water radial distribution functions (RDF) shown in Figure 7.12 at the initial and final stages of the simulations. As we carefully generated the initial structures to have uniform water distribution in the system, any deviation from the initial form of the RDF can be interpreted as a sign of extensive water clustering in the system. In both figures, the blue and red lines represent the RDF over the first and last 5 ns of production simulation runs, respectively. It is clear that the radial distribution function at high water content systems do not undergo a significant change. But for low water content systems (1 and 3 wt% systems) the initial RDF is changing during simulation time that is a sign of poor initial water distribution (in the sense of thermodynamic equilibrium) due to low number of water molecules. Accordingly, we inspected these systems visually and no water cluster has been identified over the entire simulation period. Hence, we can conclude that changes in the dynamics of the free volume redistribution are attributed to the placticization effect of water and higher mobility of the polymer segments.

7.4.5 Limitation of Mackie-Mears model

The Mackie-Mears model [159], originally developed for ion exchange membranes, is based on the obstruction concept in which polymer chains are regarded as motionless objects rel-

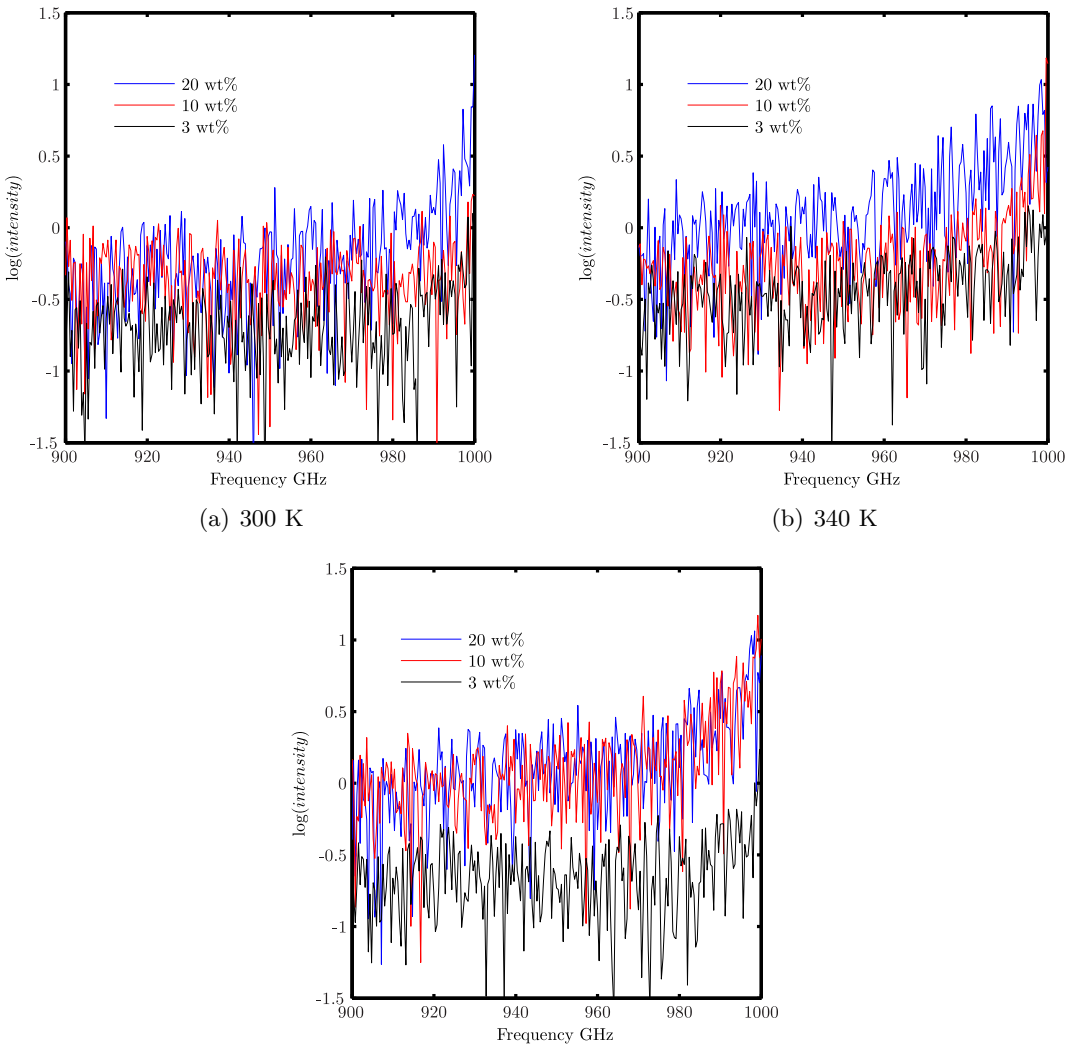

(a) 300 K

(b) 340 K

(c) 370 K

Figure 7.11: Frequency dependence of the intensity of free volume fluctuations. Data were collected from the last 5 ns of the production simulation runs.

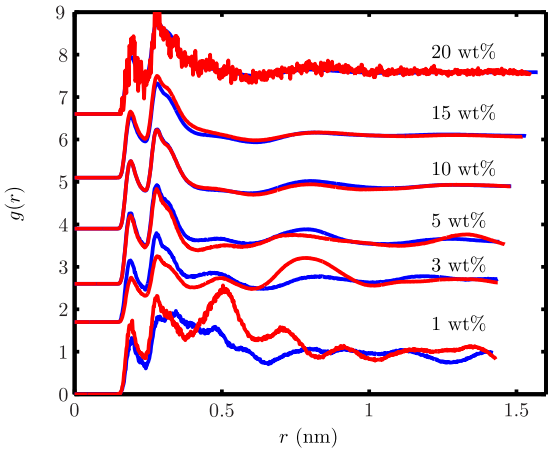

(a) 270 K

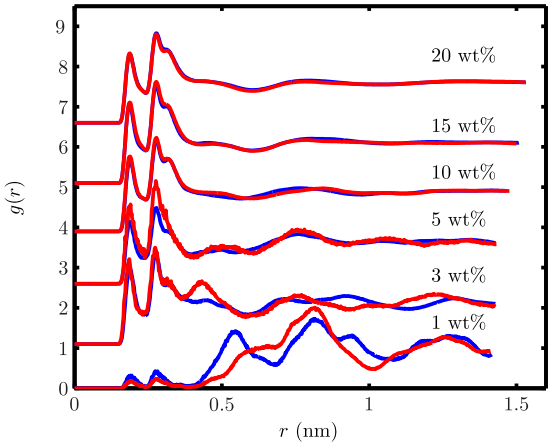

(b) 370 K

Figure 7.12: Radial distribution functions of water. The blue/red lines show data for the first/last 5 ns of the production simulation runs.

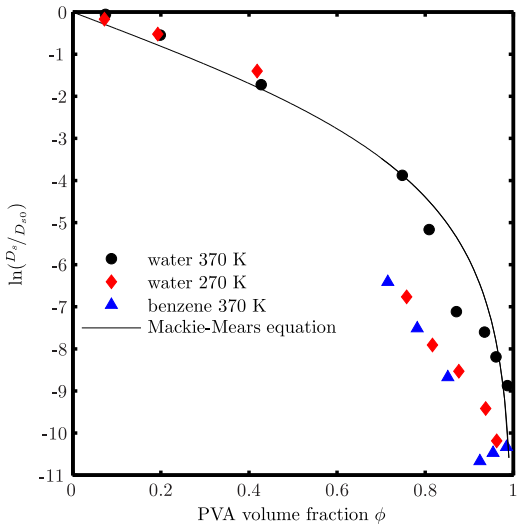

Figure 7.13: Comparison between the computed self diffusion coefficients of water and benzene in PVA at 270 and 370 K and the prediction of the Mackie-Meares model.

ative to the penetrating molecules. In fact, the polymer molecules are considered to be a collection of fixed impenetrable segments that increase the mean diffusion path length of the penetrating molecules [140]. Despite its simplicity, the prediction of the model for the self-diffusion coefficients of small molecules in a polymer matrix containing down to 60 vol% small molecules, is exceptional [160]. This seems to be the case for data at high contents of penetrating molecules shown in Figure 7.13. As mentioned before, Muller-Plathe [3] reported that the prediction of the Mackie-Mears model for water in PVA matrix is in good agreement with their MD results, and suggested that the agreement would vanish in the case of benzene, a non-polar substance. Accordingly, the self-diffusion coefficient data for water at 270 and 370 K and those for benzene at 370 K are shown in Figure 7.13 along with the prediction of the Mackie-Mears model. It is obvious that the model prediction and our simulation data agree reasonably well for water at 370 K while a significant deviation arises for the other two data sets.

Figure 7.14 compares the calculated self diffusion coefficients of both water and benzene in PVA for all temperatures and concentrations of interest. An interesting fact here is that the Mackie-Mears model systematically overestimates the self diffusion data except for a few data points at low penetrant concentrations and temperatures. As the PVA segments are not completely motionless (one of the models assumptions), our expectation was that the Mackie-Mears model would underestimate the self diffusion coefficient. Also, based upon the prediction of Muller-Plathe, we would expect to see more deviations for benzene than water, which is not the case as shown in Figure 7.14.

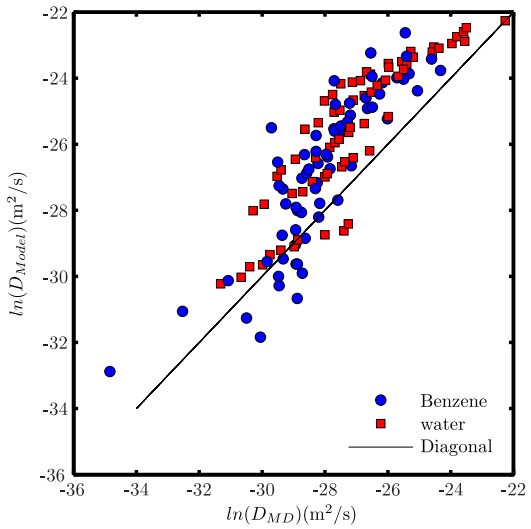

Figure 7.14: Comparison between the computed self diffusion coefficients of water and benzene in PVA at all temperatures and concentrations used and the prediction of the Mackie-Meares model. All values have been reported in the Appendix H.

Regarding these observations, there are three noteworthy points:

1. As mentioned, the Mackie-Mears model works reasonably well at high penetrant concentrations. Figure 7.15 shows the change in the diffusion mechanism of water in the PVA/water system as the water content increases. Starting at lowest temperature and water concentration (Figure 7.15(a)), it is clear that there exists no significant change in the position of the water molecules over a time span of 5 ns and that the motion of the water molecules are limited to jiggling within their confining cages. Consistently, there are no sudden changes in position and free volume during the same time (i.e., no hopping). In the next four figures, by increasing temperature and water concentration, sudden jumps in position and free volume start to emerge with increasing frequencies. The interesting fact here is that the jumps in the position and free volume of the water molecules are synchronized as predicted by the free volume theory. Another noteworthy point is that the spatial displacement of the water molecules continues to amplify as the free volume starts to reach higher values (around 0.08 nm^3). Eventually, at the highest temperature and water concentration (Figure 7.15(f)), water molecules start to drift in space and they diffuse by a fluid-like streaming mechanism rather than hopping process.

2. Our data on the intermolecular hydrogen bonds between PVA segments (not shown) indicates that water even at small amount is effectively plasticizing the PVA chains as it breaks the hydrogen bond network of the PVA. A direct result of this phenomenon is that the mobility of the PVA segments is significantly increased (see Figure 7.10) and

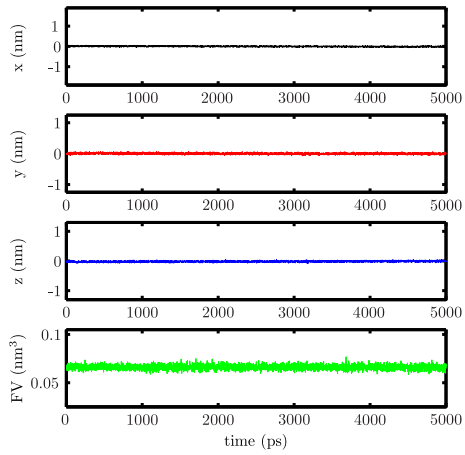

(a) 1 wt% water and 280 K

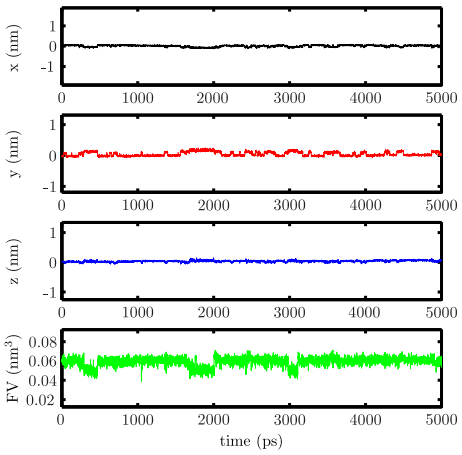

(b) 3 wt% water and 300 K

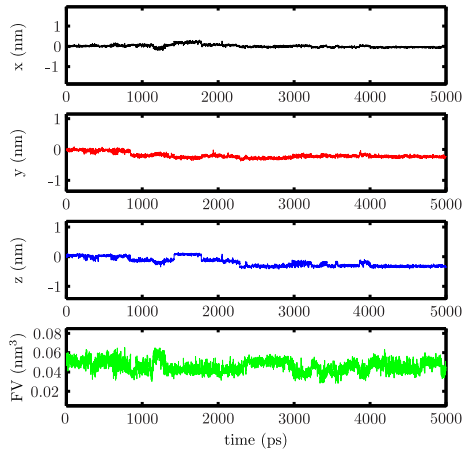

(c) 5 wt% water and 320 K

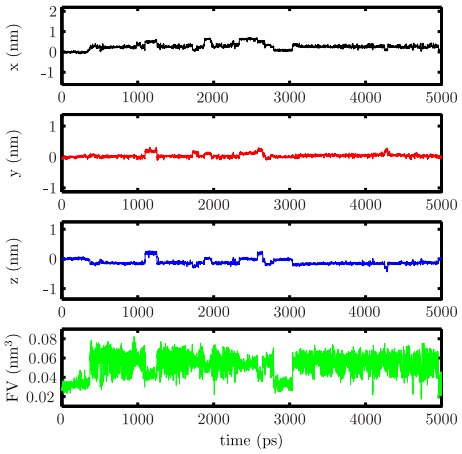

(d) 10 wt% water and 340 K

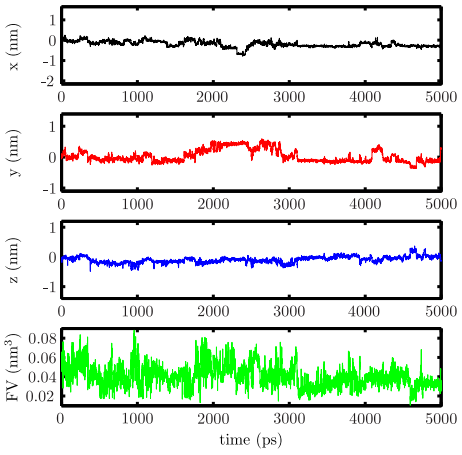

(e) 15 wt% water and 350 K

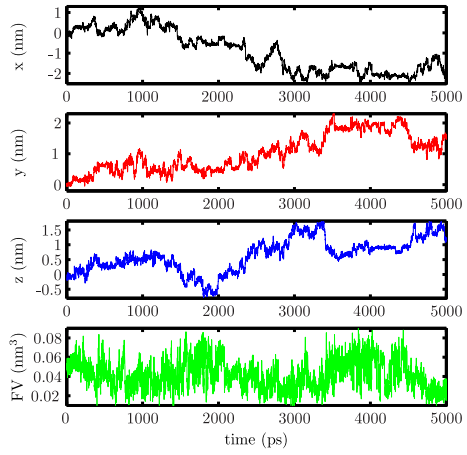

(f) 20 wt% water and 370 K

Figure 7.15: Trajectories and free volume of a water molecule. Data were collected from the last 5 ns of the production simulation runs.

reduction in the glass transition temperature of PVA. Despite this, the Mackie-Mears model still overestimates the self diffusion of the water molecules in the PVA matrix. This is because hydrogen bonds formed between water molecules and PVA segments hinder the motion of the water molecules. As shown in Figure 7.13, increasing the temperature effectively decreases the life time of hydrogen bonds. Consequently, the systematic overestimation is reduced drastically for the PVA/water system.

3. In the case of benzene, since it is incapable of breaking the hydrogen bond network of PVA and it requires larger free volume holes for jumping, even at very high temperatures and benzene contents, jumping is suppressed, let alone diffusing through a "the fluid-like" streaming mechanism as required by the Mackie-Mears model. Numbers of hydrogen bonds formed between PVA segments for water and benzene at different concentrations as shown in the Appendix H support such an argument.

It is clear from the above discussion that both intermolecular interactions and size of the penetrant play major roles in determining its diffusion in the PVA matrix. However, these two factors are not considered in the Mackie-Mears model. Considering changes in the activation energy of diffusion around the glass transition temperature and the exponential relationship between self diffusion coefficient and the degree of swelling, the free volume model of Vrentas&Duda [161, 162] seems to be a logical candidate for correlating the diffusion data. In such a model, it considers both the intermolecular interactions and size of penetrant. Unfortunately, parameters required for the free volume model of Vrentas and Duda are numerous and difficult to obtain either experimentally or by MD simulation. In this regard, Costa et al. [163] recently made a break through by combining the free volume model and Sanchez Lacombe equation of state [164–166] in such a way that the free volume parameters can be easily obtained from MD simulation. As our preliminary results indicate (results will be presented in a forthcoming publication), this lattice free volume model yields better predictions without sacrificing the simplicity of model.

7.5 Conclusion

We used molecular dynamics simulation to study the diffusion of water and benzene in a PVA matrix over a practical range of temperatures and concentrations. Computed self diffusion coefficients for both penetrants in the pure and mixed states showed great agreement with experimental and simulation data available in the literature. By applying the Voronoi tessellation method, we determined the free volume of the PVA/water system. We showed that diffusivity of water in PVA correlated with the frequency of free volume redistribution and probability of the occurrence of the critical (minimum) free volume. And such correlation depends on the water concentration. Here, the higher the water concentration, the higher the probability of the formation of free volume holes larger than the

critical free volume. Using this fact, we explained the counter intuitive observation that the diffusivity of water increases while the average free volume decreases as a result of increasing water concentration. Our data indicates that the quality of the prediction of the Mackie-Mears model for both water (polar) and benzene (non-polar) in PVA (polar) is comparable. In particular, the model overestimates the diffusion coefficients of both systems at low temperatures and low penetrant concentrations. This is because effects of intermolecular interaction (PVA/water) and size of the penetrant (PVA/benzene) are not considered in the Mackie-Mears model.

Chapter 8

Modeling solvent self diffusion in PVA matrix

8.1 Introduction

Undoubtedly, poly(vinyl alcohol) (PVA) is a technologically useful polymer [2–5, 7]. Review of a variety of applications using PVA shows that knowing the diffusivity of low molecular weight substances in PVA under different conditions (e.g., concentration, temperature, etc.) is essential to optimize the use of the material [167]. In our previous work [167], using molecular dynamics (MD) simulation, we calculated the self diffusion coefficients (SDCs) of water and benzene in PVA. Besides discerning the underlying diffusion mechanism of the solvents and the role of free volume (FV) redistribution, we also demonstrated that the Mackie-Meares model [159] is not sufficient for predicting SDCs of solvents in PVA which is in contrast to what was reported previously [3]. Our previous results [167] showed that there is a strong correlation between the calculated SDC and the degree of swelling (DS) of PVA, suggesting that a more sophisticated model that is capable of capturing the effect of FV on the predicted SDC is needed. Such a model, known as the FV theory for simple liquids [13] and its extension to polymeric systems [161, 162], is available with a great success on correlating SDCs of solvents with different system variables [168, 169].

The FV theory is a very useful, predictive model which can be applied to polymeric systems at temperatures above and below the glass transition temperature (T_g) so long as all required model parameters are known [170]. Unfortunately, parameterization of the FV model is not a trivial task [163]. In fact, most of the parameters needed are difficult to obtain. Most recently, Costa and Storti [163] have developed a lattice free volume (LFV) model, based on the original FV theory and Sanchez-Lacombe equation of state (SLEOS) [164–166], which is much easier to parameterize. Also, parameters used in the LFV model bear physical meanings that make the analysis of the system much easier [163] comparing

A modified version of this chapter has been accepted for publication in Polymer:"Prediction of self diffusion coefficients of selected solvents in poly(vinyl alcohol) using lattice-free volume theory"

to the original FV theory.

To use the LFV model, parameterization of the SLEOS is needed. In this work, SLEOS parameters for PVA and three solvents (water, ethanol and benzene) were determined. After validating the SLEOS parameters, they were used in the LFV model to calculate SDCs of the corresponding solvents at various concentrations and temperatures. A brief recap of underlying theories and a summary of simulations required to calculate the SLEOS parameters will be presented in the next section before the discussion of the results.

8.2 Theoretical background

In this section, the SLEOS and the LFV formulation using the original FV theory are provided. Readers who are interested in the original FV theory are referred to the work of Vrentas and Duda [161, 162].

8.2.1 Sanchez-Lacombe equation of state

The Sanchez-Lacombe equation of state (SLEOS) [164–166] is a powerful lattice based thermodynamic model for the prediction of properties of fluids in the pure and mixed states including those of polymer solutions and blends. As an evolutionary counterpart of the Flory-Huggins (FH) theory [171, 172], it considers the volume change upon mixing, which is not considered in the FH theory. Therefore, the SLEOS is able to predict both lower and upper critical solution temperatures (LCST and UCST) while the FH theory can only predict the UCST, a well-known weakness of the FH theory [173]. Equation 8.1 shows the general form of SLEOS [173]:

$$\tilde{\rho}^2 + \tilde{P} + \tilde{T}[ln(1-\tilde{\rho}) + (1-\frac{1}{r})\tilde{\rho}] = 0 \tag{8.1}$$

Here, r is a molecular size parameter (see Equation 8.10) and

$$\tilde{\rho} = \frac{\rho}{\rho^*} \qquad \tilde{P} = \frac{P}{P^*} \qquad \tilde{T} = \frac{T}{T^*} \tag{8.2}$$

where ρ, P and T are density, pressure and temperature, respectively and ρ^*, P^* and T^* are the respective characteristic parameters yet to be determined. Conventionally, the characteristic parameters are obtained by fitting a large set of experimental PVT data for pure components while mixtures are handled by applying proper mixing rules. Recently, a method for the derivation of these characteristic parameters using MD simulation has emerged in the literature [173, 174]. In this study, we followed the procedure proposed by Jo and Choi [173] along with the correction proposed by Li et al. [174] to accurately estimate the temperature dependency of the characteristic temperature, (T^*). For binary mixtures containing PVA and solvent, we utilized a commonly used mixing rule (unless otherwise stated) as follows [163]:

$$\phi_i = \frac{w_i/\rho_i^*}{\sum_i w_i/\rho_i^*} \tag{8.3}$$

$$\rho{*}_{mix} = \left(\sum_i w_i/\rho_i^*\right)^{-1} \tag{8.4}$$

$$\Delta P = P_1^* + P_2^* - 2\chi\sqrt{P_1^* P_2^*} \tag{8.5}$$

$$P_{mix}^* = \sum_i \phi_i P_i^* - \phi_1\phi_2\Delta P \tag{8.6}$$

$$\nu_{mix}^* = \left(\sum_i \phi_i/\nu_i^*\right)^{-1} \tag{8.7}$$

$$T_{mix}^* = \frac{P_{mix}^*\nu_{mix}^*}{R} \tag{8.8}$$

$$r_{mix} = \sum_i x_i r_i \tag{8.9}$$

where ϕ_i is the volume fraction; w_i is the weight fraction; ν_i^* is the characteristic specific volume; and x_i is the mole fraction. In the above equations, the asterisk signifies the SLEOS characteristic parameters and super script "mix" denotes the property of the mixture. The χ parameter in Equation 8.5 refers to the Flory-Huggins interaction parameter of a pair of polymer and solvent. Although we had the values for this parameter for the systems under study in this work, we used an estimate value of 1 (only in the cases of ethanol and benzene.) as suggested by Costa and Storti [163]. This is because values of P_{mix}^* (Equation 8.6) were not sensitive to the value of ΔP (Equation 8.5). To calculate r and ν^*, the following equation is needed:

$$\nu{*} = \frac{RT^*}{P{*}} \qquad r = \frac{MP^*}{RT^*\rho^*} \tag{8.10}$$

where M is the molecular weight.

8.2.2 Lattice free volume model

The lattice free volume (LFV) model is basically derived from the FV theory by re-parameterizing it based upon the concept that there exists equivalence between free volume and the so-called unoccupied volume stated in the SLEOS. For the details of the derivation, interested readers are referred to the work done by Costa and Storti [163]. The final form of the LFV model reads:

$$D_{S,1} = D_{0,1} exp\left(-\gamma\frac{\omega_1/\rho_1^* + \xi\omega_2/\rho_2^*}{1/\rho_{mix} - 1/\rho_{mix}^*}\right) \tag{8.11}$$

where $D_{S,1}$ and $D_{S,0}$ are the SDCs of the solvent in the mixture and pure states, respectively; γ is the overlap factor in the original FV theory; ω_i is the weight fraction of each component; ρ_i is the density of pure components or mixture. The asterisk indicates the SLEOS characteristic parameters. The parameter ξ is defined as follows:

$$\xi = \frac{M_1^{\#}\rho_2^*}{M_2^{\#}\rho_1^*} \tag{8.12}$$

where $M_i^{\#}$ refers to the molecular weight of the solvent and that of the hypothetical jumping unit of the polymer. Originally, the FV model was developed for the rubbery state, but its prediction for the glassy region (without any modification) is also reasonable [170].

8.3 Molecular dynamics simulation

In this work, molecular dynamics (MD) simulation was used for the parameterization of the SLEOS of the polymer, solvents and their binary mixtures. To calculate SDCs of the solvents in the binary mixtures using Equation 8.11, we used the calculated SDCs of the solvents in the pure state reported previously [167]. For polymer/solvent binary mixtures, SDC values previously calculated [167] over a concentration range of 1-20 wt% of the solvent and a temperature range of 270-370 K were used to compare with the results obtained using the LFV model. For the parameterization of the SLEOS for each component in its pure state, isobaric-isothermal MD simulations were carried out at the atmospheric pressure and over a temperature range of from 50-600 K with 50 K intervals. Since some of the systems were not stable at elevated temperatures, only data with liquid like densities were used. GROMACS 4.5.5 [58–62] was used for performing all MD simulations along with the OPLS-AA force field [25] to describe ethanol, benzene and PVA. The TIP4P model developed by Jorgensen et al. [76, 77] was used for water.

In all simulations, the Berendsen thermostat/barostat [20] with time constants of 0.2/1 ps were used to control the temperature/pressure of the simulation cells. Newtons equations of motion were integrated using the leap-frog algorithm [135] with a time step of 1 fs and a sampling time of 1 ps. The cut-off distance of the non-bonded interactions was set to 1 nm and the Particle Mesh Ewald (PME) [136] method was used for handling the long range Coulombic interactions. The long range dispersion energy and pressure corrections were applied to retrieve the correct density of the system. Depending on the system (solvent or polymer), simulation times ranged between 10-30 ns were used. Note that our previous work showed that the aforementioned simulation times were long enough to equilibrate the systems.

8.4 Results and discussion

8.4.1 SLEOS parameters for pure components

Having computed the equilibrium density and potential energy for each pure component over a wide range of temperatures, we determined their ρ^* and P^* by extrapolating the density and cohesive energy density (E_{coh})to 0 K, respectively. The cohesive energy density is defined as:

$$E_{coh} = \frac{E_{vacuum} - E_{condensed}}{V} \tag{8.13}$$

where E is the total potential energy in vacuum and in the condensed state, respectively, and V is the molar volume of material in its condensed state. Note that in the case of PVA, for both ρ^* and P^*, only the data below its T_g (350 K) was used. After obtaining these two characteristic parameters, T^* can then be easily calculated by fitting ρ^* and P^* to Equation 8.1. The value of T^* is not constant and shows a temperature dependency. Accordingly, a Boltzmann distribution was fitted to the calculated T^* to obtain the extrapolated values at higher temperatures as suggested by Li et al. [174]. For the sample MD calculation of the characteristic parameters, readers are referred to I.

Table 8.1: Sanchez-Lacombe equation of state parameters

	ρ^* (kg/m^3)	P^* (bar)	T^* (K)	Reference
Water	1083	16716	756	[175]
	1030	30500	826	This study
Ethanol	881	3989	583	Experimental[a]
	960	11500	431	This study
Benzene	971	4962	564	[175]
	996	4480	520	[163]
	1045	6800	458	This study
PVA	1346	8288	859	Experimental[a]
	1293	7947	888	This study

[a] These parameters are the results of fitting SLEOS directly on a set of experimental densities for ethanol [176] and PVA [74] over a wide range of temperatures and pressures. For the data used for the fitting and the quality of the fits see I. As the SLEOS is only valid for the rubbery region, only data collected at temperatures above the T_g of PVA but below its melting point were used.

The computed characteristic parameters are shown in Table 8.1. In the cases of water and benzene, characteristic parameters computed in this work are compared with values reported in the literature. But, in the case of PVA and ethanol, to the best knowledge of the authors, no such parameters have been reported previously. Therefore, results are compared

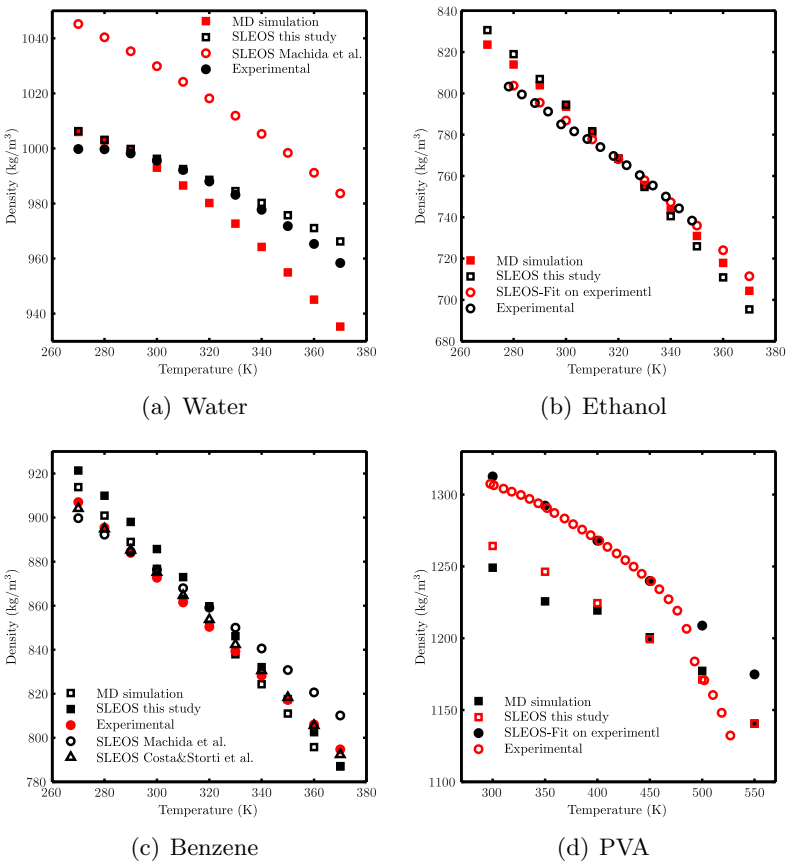

(a) Water (b) Ethanol

(c) Benzene (d) PVA

Figure 8.1: Comparison between density values calculated from isobaric-isothermal MD simulations and experiment at atmospheric pressure and different temperatures.

with those obtained by fitting the SLEOS to the experimental PVT data available. The calculated characteristic parameters for PVA are in good agreement with those obtained by the fitting of the experimental PVT data to the SLEOS. But in the cases of solvents, there exist significant discrepancies. The discrepancies between P^* from this work and those of experiment should not be viewed negatively on the quality of the computed P^*. In fact, to obtain P^*, the SLEOS was solved by simultaneously inserting ρ^* and T^* and adjusting P^* to fit the MD data. Therefore, the discrepancies are not solely of P^*. In our view, individual characteristic parameters should not be compared one by one. Instead, their quality should be examined based upon their predictions of properties. Accordingly, we compare the predicted density using the characteristic parameters shown in Table 8.1 to the experimental values (see Figure 8.1). As can be seen, in all cases, predictions are fairly close to the experimental values. The only deviation is on the PVA density at very low temperatures where our parameters reproduce the MD calculated densities well, but off the experimental values. This is not a problem with the SLEOS itself. In fact, it is a known problem of MD simulation of PVA due to the lack of crystalline phase in the PVA model [119]. Since the crystalline phase does not exist in our simulated systems, characteristic parameters derived in this study should be valid to be used in the LFV model.

8.4.2 SLEOS parameters for mixtures

To validate the derived characteristic parameters from the mixing rule, we compare the direct MD calculated densities of the mixtures with those calculated using the SLEOS along with the mixing rule as shown in Figure 8.2. As can be seen, despite small deviations in predictions by the SLEOS for pure components, predictions for PVA/solvent mixtures are in reasonable agreement with the direct MD calculations. While the mixing rule in Equations 8.3-8.9 worked well in the cases of PVA/benzene and PVA/ethanol systems, predictions for the PVA/water system was poor (results not shown). However, it was found that the normal weighted average for both ρ^*_{mix} and T^*_{mix} based on weight fractions yielded reasonable results:

$$\begin{aligned} \rho^*_{mix} &= w_1\rho^*_1 + w_2\rho^*_2 \\ T^*_{mix} &= w_1T^*_1 + w_2T^*_2 \end{aligned} \tag{8.14}$$

It is worth noting that there exist other mixing rules in the open literature [177, 178]. However, we found that none of them yielded better predictions than the normal weighted average for the PVA/water system. To justify this choice, we calculated the T^* and P^* for the PVA/water system with different solvent contents by the direct simulation of the mixtures over the temperature range mentioned earlier. Figure 8.3 shows the comparison of directly calculated characteristic parameters with the weighted average values and those calculated by the mixing rule depicted in Equations 8.3-8.9. This comparison confirms the accuracy of the weighted average values comparing to those obtained by the mixing rule.

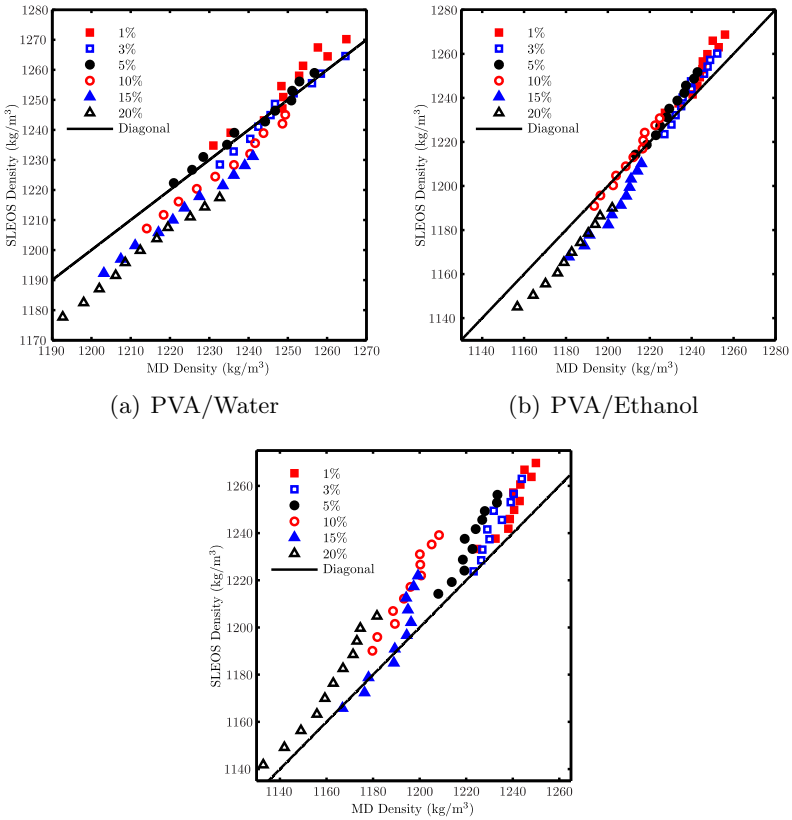

(a) PVA/Water

(b) PVA/Ethanol

(c) PVA/Benzene

Figure 8.2: Comparison between density values of the PVA/water system at various water concentrations and those predicted by the SLEOS. For each solvent concentration, data are obtained over a temperature range of 270-370 K with an interval of 10 K.

Note that values of T^*_{mix} are very sensitive to the χ parameter of the system. The reason behind this is that there exists a large difference between P^* of water and that of PVA. For other solvents, when the mixing rule was applied, the sensitivity to χ parameters was negligible and its value was considered to be 1 as recommended by Costa and Storti [163].

Furthermore, in Figure 8.4, experimental densities of the PVA/water system at very low polymer concentrations are compared with predictions by the SLEOS. The perfect agreement indicates that the parameterized SLEOS is a good representation of the system over a wide range of concentrations. The reason that predictions by the SLEOS at high water contents is more accurate than those at low water contents is attributed to the fact that no crystalline phase exists at high water contents, as it was experimentally demonstrated that all crystalline domains of PVA dissolve under such conditions [179].

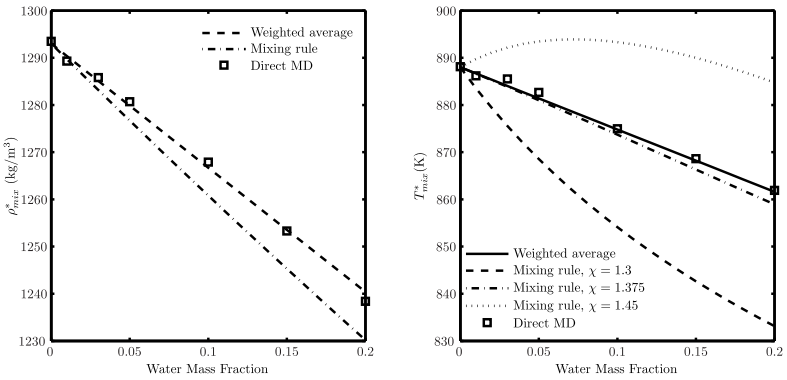

(a) ρ^*_{mix} (b) T^*_{mix}

Figure 8.3: Comparison between characteristic parameters of the SLEOS for the PVA/water system at various water concentrations.

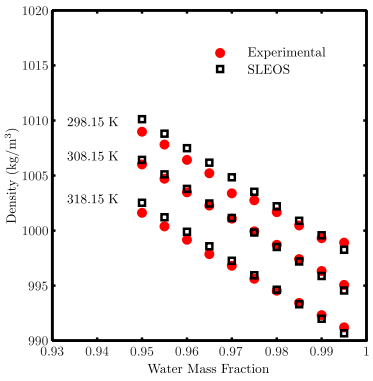

Figure 8.4: Comparison between density values predicted by the SLEOS at high water concentrations and experiment for the PVA/water system [1].

8.4.3 Calculation of SDC from the LFV model

Majority of the parameters needed for the LFV model ρ_i^* and the mixing rule were determined and validated in the previous section. The only remaining parameters for the model that needed to be determined were γ and ξ. Here, γ should have a value of 0.5-1 theoretically. But, as Costa and Storti [163] suggested, it can be used as a fitting parameter with the only requirement of positivity. And the parameter ξ is defined as the ratio of the molar volume of the solvent to that of a polymer jumping unit. In other words, ξ is directly related to the mobility of polymer segments. Stiffer chains are expected to have smaller ξ than more flexible chains. However, when the Vreantas and Duda free volume theory is used to correlate the diffusion coefficient data, parameter ξ is considered to be an adjustable parameter. This parameter is the most ambiguous in the free volume theory formulation [163], and the LFV model also suffers from this drawback. Accordingly, in this study, we used this parameter as a fitting parameter as well. Results of fitting the LFV model on the diffusion coefficient data for PVA/solvent systems are summarized in Figure 8.5(a). By comparing the results with the predictions of the Mackie-Meares model in Figure 8.5(b) (from our previous work [167]), it is clear that the LFV model is astonishingly more successful in correlation of the data. This is partly due to the consideration of the effect of free volume and glass transition in the model and partly due to the free fitting parameters in the LFV model. It should be noted that the Mackie-Meares model was developed for polymers in the rubbery state. As you can see from Figure 8.5, the LFV model outperforms the Mackie-Meares in that state (high SDCs region in the upper right hand corner of the figure). The agreement between the Mackie-Meares model and MD results in the glassy region (low SDCs region) is merely a coincidence, as the model was not built for the glassy state. However, the LFV model bears a meaningful deviation from the MD results in the glassy state, as this is one of the major inadequacies of the original FV theory. Upon using a modified version of the FV theory (the work is ongoing in our lab), such deviations could be reduced. The deviation at low temperatures, in the case of benzene and ethanol, can be attributed to two factors. First, as the temperature is low and the size of the solvent molecules is bigger than water, MD simulations would overestimate SDCs due to slight deviation of the means square displacement curves from a perfect line. Secondly, as Figure H.1 indicates, these solvents are not capable of breaking hydrogen bonds in PVA as successful as water does. Therefore, the system is effectively below the glass transition temperature of the mixture and the modified version of FV model[170] should be applied. The latter makes more sense, as the deviation of MD results from the model correlate well with the amount of hydrogen bonds left in the PVA matrix.

All the parameters used in the LFV model are summarized in Table 8.2. As the results indicate, γ increases with increasing size of the solvent molecules which is reasonable. This means that the chance of overlap between free volume elements decreases as their size

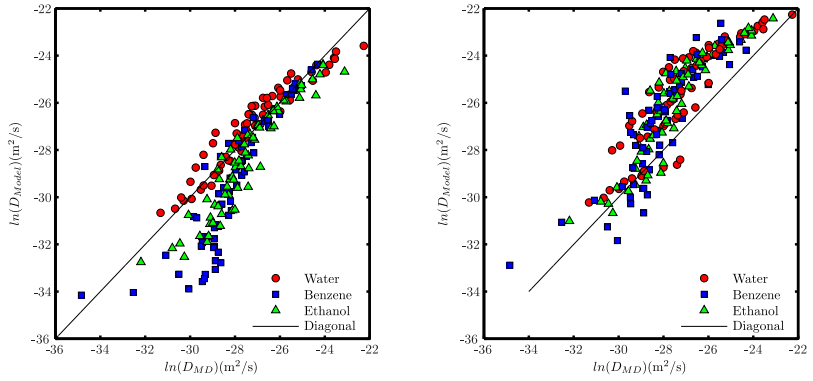

(a) LFV (b) Mackie-Meares

Figure 8.5: Comparison between SDCs of solvents as calculated by MD simulations and those predicted by (a) the lattice free volume model and (b) the Mackie-Meares model.

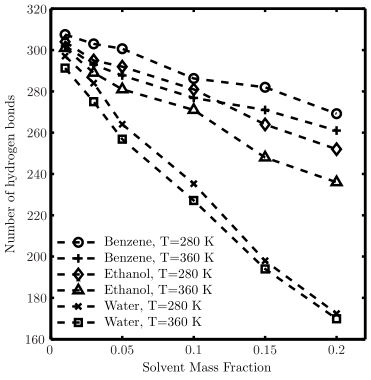

Figure 8.6: Number of hydrogen bonds formed between PVA and solvent at various solvent concentrations.

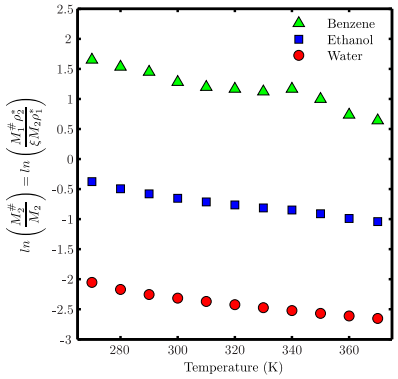

Figure 8.7: Temperature dependence of polymer jumping units. Note that $M_1^\#$ and $M_2^\#$ are the molar mass of the solvent and PVA jumping unit, respectively.

increases. Also, Figure 8.7 shows changes in the polymer jumping unit as a function of temperature for different solvents. Here, we would like stress on two facts. First, in the case of water, the polymer jumping unit has the smallest value due to the maximum chain flexibility (broken hydrogen bonds) and in the case of benzene, it has the largest size due to the presence of a higher number of hydrogen bonds. Secondly, in all cases, the size of jumping unit increases as temperature increases. And this observation was reported previously [163, 180].

Table 8.2: Summary of parameters used in the LFV model used to describe the PVA/solvent systems.

Solvent	γ	ρ_1^* (kg/m^3)	ρ_2^* (kg/m^3)	Mixing rule
Water	0.0504	1030	1293	Wighted average
Ethanol	0.3991	990	1293	Eq. 8.3-8.9
Benzene	0.6662	1097	1293	Eq. 8.3-8.9

8.5 Conclusion

In this work, we determined the characteristic parameters of PVA, water, ethanol and benzene for the corresponding Sanchez-Lacombe equation of state using data generated from isobaric-isothermal MD simulations. The SLEOS was found to be capable of predicting properties of the pure components and their mixtures as validated against the experimental and simulation data available. Using results from the direct simulation of the PVA/water mixture, we showed that the mixing rule normally used for the system was not effective and normal averaging based on weight fractions yielded better estimates. Finally, we used such parameters to correlate the SDCs of solvents in PVA at various solvent concentrations and temperatures. The results confirm that the LFV model is much more successful in correlating the data than the simple Mackie-Meares model with considering changes in the mobility

of the polymer segments. Details of the hydrogen bonding in PVA in different solvents confirm that water is more effective in increasing the chain mobility by breaking hydrogen bonding network of the PVA more effectively. Slight deviation of the MD calculated SDCs for ethanol and benzene at low temperatures from the LFV model was attributed to the glassy state of the mixture which requires a modified version of the FV model to handle that.

Chapter 9

Study of cyclohexane diffusion in Athabasca asphaltenes

9.1 Introduction

After Saudi Arabia and Venezuela, Albertas oil sands deposits represent the third largest proven crude oil reserves in the world[181, 182]. There are currently two methods for bitumen extraction from oil sands[183]. For deep deposits, steam assisted gravity drainage (SAGD) technology is used where thermal energy is applied to heat the bitumen in-place and allow it to flow to the well bore and be pumped to the surface. Bitumen recovery by the in-situ technologies is typically less than 60%. In order to enhance the energy efficiency of these processes, injection of a mixture of steam and solvent is under commercial development[184]. In this case, the recovery of the solvent from the reservoir is a major concern.

Shallow oil sands ores are mined by surface mining methods, which currently contribute 55% of the oil production in Alberta. In this case, the bitumen is recovered by water extraction whereby oil sands are mixed with hot water and caustic and sent through a hydro-transport pipeline to the extraction plant where the bitumen froth is recovered by flotation.

While bitumen extraction using hot water is an economic recovery process, its disadvantage is high fresh water and energy consumption. The volumetric water-to-bitumen ratio in this process is approximately 19. The majority of the process water is recycled, but some of the water is trapped in the wet unsettled tailings, giving net consumption of 2 to 4.5 barrels of fresh water to produce one barrel of oil.3,5 The resulting wet tailings, a mixture of water, fine solids, and residual bitumen, require large tailings ponds which had accumulated

A modified version of this appendix was published: "Study of Cyclohexane Diffusion in Athabasca Asphaltenes", Abolfazl Noorjahan, Xiaoli Tan, Qi Liu, Murray R. Gray, and Phillip Choi, Energy&Fuels 28(2) 2014, 1004-1011

to about 650 million m^3 by 2006 [183]. These large volumes of wet tailings are a risk to wildlife and a liability for future remediation [181, 185, 186]. The use of hot water, which has a high heat capacity, contributes to the energy consumption in this process[185].

Another input to the extraction process is solvent, which is used to dilute the bitumen froth to enable the removal residual solids and emulsified water [187]. The majority of the solvent is recovered, but some is released to the tailings ponds. Depending on the plant, the solvent may be naphtha or a hexane-rich mixture. In the case of the hexane-based process, a portion of the asphaltenes in the oil are precipitated[188], so that recovery of residual solvent from asphaltenes is a major concern.

Solvent extraction of bitumen is an alternative technology that offers high recovery from a range of ores [182, 185, 189, 190]. Solvent extraction can greatly decrease or eliminate fresh water demand for the extraction process and eliminate the wet tailings associated with the hot water process. It works at ambient pressure and temperature, so less energy is consumed in the addition of solvent. The solvent-extracted mixture of sand and fine solids, which we call gangue, is almost dry and can be returned to the mine area immediately to enable fast reclamation of the landscape. The biggest technical, economic, safety, and environmental challenge of solvent extraction is the recovery of solvents from the gangue [185, 190].

Several promising solvents have been identified, including aromatics, n-alkanes and cycloalkanes [181, 191–193], but a key criterion is the recovery of the solvent by methods such as vacuum or atmospheric drying [194]. Cycloalkanes have the advantage of high solvent power, high vapor pressure, and low odor [181, 191]. A successful process must remove solvent from the gangue to give residual concentrations lower than circa 250 ppm, better than the current losses of solvents from the froth treatment process. In the gangue, the main capacity for retention of solvent will be in residual bitumen, residual asphaltenes, and insoluble adsorbed organic matter that occurs in oil sands ores [186].

For detailed engineering design, we need to predict the diffusion of solvents out of these organic materials, especially at low residual solvent concentrations. Several studies on solvent diffusion in bitumen have shown that the diffusion coefficients are strongly concentration dependent [192, 195–197], with values at low solvent concentrations ranging from 10^{-11} to 10^{-12} m^2/s at 25 °C.

Given the technologies for oil sands production, data on solvent diffusion in asphaltene fractions are important for enhancing solvent recovery from existing froth treatment processes and from future solvent extraction processes. In this study, we examine the rate of

desorption or release of cyclohexane solvent from bitumen films by gravimetric measurements, and use these data to model the concentration-dependent diffusion coefficients.

9.2 Materials and methods

9.2.1 Materials

The Athabasca asphaltenes used in this study were from the bottom stream of a deasphalting unit processing bitumen from a steam-assisted gravity drainage (SAGD) operation. This material contained 28 wt% pentane-solubles based on the standard method of dissolution then precipitation in 40:1 solvent.
Reagent-grade cyclohexane and methylene chloride purchased from Fisher Scientific (Mississauga, Ontario, Canada) were used as received. P-type double-side polished silicon wafers (100) with a 250 µm in thickness and a resistivity of 135 Ω cm were purchased from University Wafer (Boston, MA). Nitrogen (99.999%, Praxair) was used as carrier gas for all sorption and desorption experiments.

9.2.2 Asphaltene film preparation

To obtain a regular geometry, a rectangular film of asphaltene was prepared. For this purpose, the silicon wafer was cut into 12 pieces of rectangular shape with known mass and surface area (a total surface area of 35.28 (cm^2)) in order to accommodate these pieces in the sample bucket for following experiments. A 1.0 wt% of Athabasca asphaltene solution in methylene chloride was sprayed on both sides of silicon wafers by using an air brush. The mass of coated asphaltene on these pieces of silicon wafer was pre-calculated to get the desired thickness. For each piece of silicon wafer, the deposition of asphaltene was multistep process where the actual mass of coated asphaltenes on silicon wafer was monitored by using analytical balance at each step of spraying following by drying at room temperature in fumehood to evaporate the solvent. After deposition, all asphaltene coated wafers were air dried for 48 hours in a fumehood then weighted to calculate the mean thickness of asphaltene films, which was 7 ± 1.4(µm).

9.2.3 Methods

A Hiden Intelligent Mass Gravimetric Analyzer (IGA) was used for sorption/desorption experiments. The schematic of this unit is shown in Figure 9.2. The IGA allows isotherms and the corresponding kinetics of sorption and desorption for set pressure or partial pressure steps. The balance and pressure control system were isothermal to ±0.01 °C to eliminate changes due to variation in the external environment. The microbalance with a sample loading range of 50 mg and 2.0 g had a long-term stability of ±1 µg with a weighing resolution of 0.2 µg. The sample temperature was controlled by water bath while the pressure was maintained at the set point by active computer control of the inlet/outlet

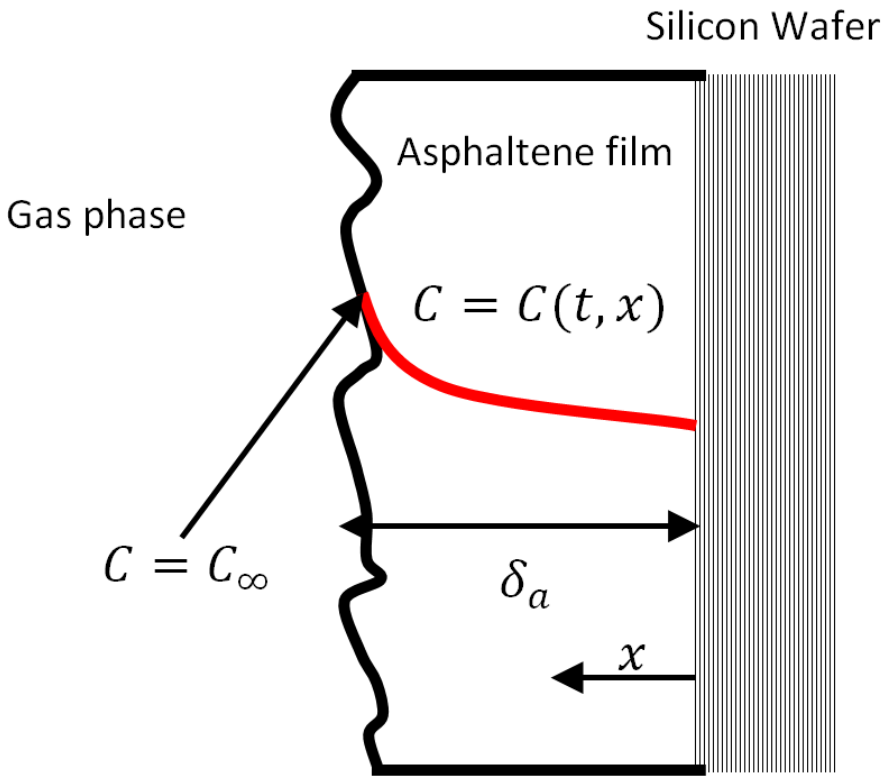

Figure 9.1: Sample geometry for sorption

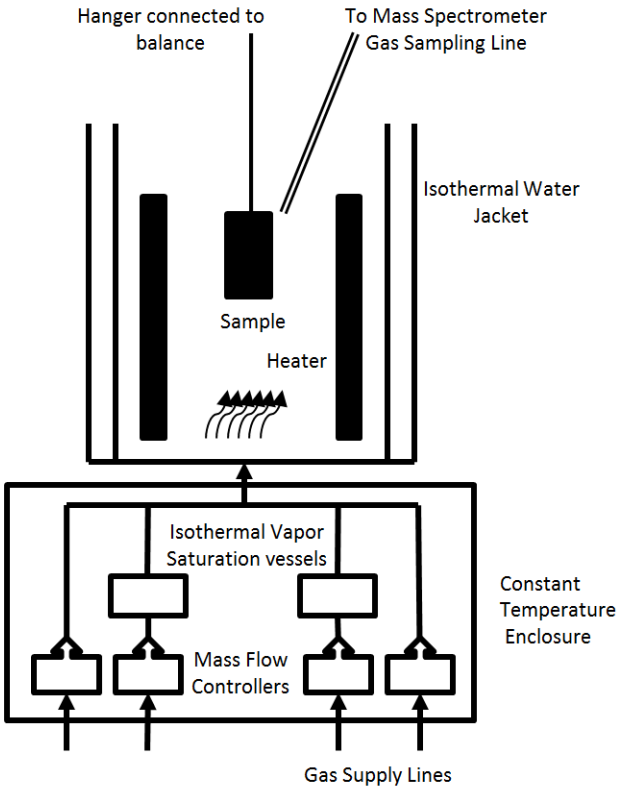

Figure 9.2: Schematic of Hiden Intelligent mass gravimetry analyzer

valves throughout the duration of the experiment. The solvent vapor with a desired relative pressure was maintained from a temperature controlled saturated vapor generator and the output of the generator was mixed with a flow of pure inert gas as carrier gas, and then the vapor was introduced through the sample chamber with specific flow rates. In our experiments, the nitrogen was the carrier gas. The experiments were conducted at sample temperatures of 30 °C and 40 °C, respectively, while the temperature of vapor generator was fixed at 30 °C to generate the relative pressure of cyclohexane vapor of 0.4 and 0.9 at each sample temperature correspondingly. In each set of experiment, the asphaltene coated silicon wafers were pretreated within the IGA at 70 °C in nitrogen atmosphere with flow rate of 100 mL min^{-1} to remove residual solvents and water until the weight of sample leveled off. The total flow rate throughout the experiments was kept at 50 mL min^{-1}, whereas the pressure was maintained at a constant value of 105 ± 0.1 kPa and the temperature variation was < 0.1 °C. The mass uptake of samples was monitored as a function of time in different cyclohexane vapor concentrations with a computer algorithm.

9.3 Theory for mass uptake and release kinetics and diffusion coefficients

Typically the mass uptake and release in sorption/desorption of light components on different materials shows 5 different classes of kinetics [9] which can be classified using a power law relationship as follows:

$$\frac{M_t}{M_\infty} = kt^n \tag{9.1}$$

Where M_t and M_∞ are the mass uptake/release in finite time and mass uptake at infinite time (equilibrium), and k is the kinetic constant. Different values of the exponent, n, and their physical interpretations are summarized in Table 9.1.

Table 9.1: Typical observed mass uptake kinetics

n	Name	Note
> 1	Super case II	Swelling controlled Diffusion
1	Case II	-
$1/2 <,< 1$	Anomalous	-
$1/2$	Fickian	Normal Fickian Diffusion
$< 1/2$	Pseudo Fickian	Concentration Dependent Diffusion

Given the data for sorption and desorption, we can discern the underlying mechanism with determining the power n to best fit the data. When the limiting mechanism can be attributed to diffusion, the general form of second law of Fick can be used to determine the diffusion coefficient of solvent in asphaltenes as follows (for notation see figure 9.1):

$$\frac{\partial C}{\partial t} = \frac{\partial}{\partial x}\left(D_{AS}(C)\frac{\partial C}{\partial x}\right) = D_{AS}\frac{\partial^2 C}{\partial x^2} + \frac{dD_{AS}}{dC}\left(\frac{\partial C}{\partial x}\right)^2 \tag{9.2}$$

where C is the concentration of cyclohexane in the asphaltenes, t is time, x is the Cartesian coordinate and D_{AS} is the diffusion coefficient. To determine the diffusion coefficient, the nonlinear partial differential equation in Eq. 9.2 must be solved with the following boundary and initial conditions:

$$\begin{aligned} C &= C_0 \qquad t = 0 \\ C &= C_\infty \qquad x = \delta_a \\ \frac{\partial C}{\partial x} &= 0 \qquad x = 0 \end{aligned} \tag{9.3}$$

where C_0 is the initial concentration (which is zero for sorption and C_∞ for desorption), C_∞ is the equilibrium concentration at the end of sorption and δ_a is the average thickness of the prepared asphaltene film. It has been assumed that the film surface is always in equilibrium with gas phase. To solve Eq. 9.2, the method of lines was used, where the spatial

domain is discretized using central finite difference scheme. And a fifth order predictor corrector has been used for the integration in temporal domain. To reduce the numerical error, the finest required mesh was obtained according to Richardson extrapolation criteria. To calculate the value of D_{AS}, a Levenberg-Marquardt optimizer was coupled to an ordinary differential equation solver to find the best value of D_AS which can fit the data. We considered 3 different functionalities for diffusion coefficients with different levels of flexibility as follows:

1. A constant value

2. Arational functionality with concentration

$$\frac{D}{D_0} = \frac{\alpha}{\beta \frac{C}{C_\infty} + \alpha} \tag{9.4}$$

   Where D_0, α and β are constants to be determined by optimization.

3. A flexible error function[198]

$$\frac{D}{D_0} = \left(1 + \alpha\ erf\left(\beta \frac{C}{C_{max}}\right) + \gamma \frac{C}{C_{max}}\right) \tag{9.5}$$

   Where D_0, α, β and γ are constants to be determined by optimization.

In addition to the above analysis, the sorption/desorption data were compared with some other models from the literature to get more insight about the changes in the asphaltenes medium during the sorption/desorption processes. The first model is a double-first order kinetics model, which is the case when a portion of mass uptake or release is governed by a faster mechanism while the other portion is significantly slower. The mass uptake can be modeled as follows[199]:

$$\frac{M_t}{M_\infty} = \phi\left(1 - e^{-k_1 t}\right) + (1 - \phi)\left(1 - e^{-k_2 t}\right) \tag{9.6}$$

where ϕ is a fraction of the total mass up taken by first mechanism and k_1 and k_2 are kinetic constants related to first and second mechanisms, respectively.

The other model is the Weibull relaxation model[200] which indicates a continuous relaxation of the model medium during sorption/desorption to a more compact structure by introducing a stretched exponential with parameter ξ, which is related to the visco-elastic relaxation time of medium. This relaxation is enhanced by extra mobility of the medium due to plasticizing effect of the solvent and has been reported mostly for sorption in glassy polymers[201]. The governing equation is as follows:

$$\frac{M_t}{M_\infty} = 1 - e^{-(kt)^\xi} \tag{9.7}$$

where ξ is the Weibull relaxation parameter.

9.4 Results

Sorption/desorption experiments were carried out on asphaltene films at 30 and 40 °C and at 40% and 90% vapor saturation. Vapor saturation was kept below 100% to prevent solvent condensation on the film surface. The mass uptake and release for these experiments is plotted in Figure 9.3. At higher vapor saturation, the sorption process is very fast, regardless of temperature. The sorption at higher vapor saturation is much faster than desorption, which is not the case in lower vapor saturation where the two processes have comparable time scales. In every case, however, the desorption kinetics are slower than the rate of the corresponding sorption process. The data of Table 9.2 show the equilibrium concentration of the cyclohexane in the sample. These data indicate that with increasing temperature, the absorption of cyclohexane in asphaltenes is reduced, but as shown in Figure 9.3, the kinetics of uptake and release are significantly affected by temperature.
The diffusion coefficient of the cyclohexane in gas phase (30-40 °C) is around 10^{-5} m^2/s, which is much larger than the diffusion coefficient in the asphaltene phase. As the Reynolds number in the tubular section of the IGA is around 1.5 (laminar flow), in the worst case scenario the boundary-layer thickness would be the diameter of the tabular section of the IGA which is 5 cm. In this case, the ratio of the resistance of mass transfer in the asphaltenes phase to gas phase would be:

$$\frac{D_g \delta_{AS}}{D_{AS} \delta_g} = \frac{10^{-5} * 7 * 10^{-6}}{10^{-10} * 5 * 10^{-2}} = 14 \tag{9.8}$$

In this analysis, the value of $D_A S$ was taken as larger than the range of values reported for bitumen in the literature, and still resistance in gas phase is negligible. This calculation justifies the first boundary condition in Eq. 9.3 and neglecting the gas phase resistance in all subsequent analysis.

Table 9.2: Equilibrium concentration of cyclohexane in asphaltenes

T (°C)	Vap. Sat. (%)	Equilibrium concentration (g Cyclohexane/g Asphaltenes)
30	40	0.038±0.0001
30	90	0.202±0.0001
40	40	0.020±0.0001
40	90	0.065±0.0001

9.4.1 Mass uptake/release analysis

Table 9.3 summarizes the results of fitting Eq. 9.1 to the sorption/desorption data. The small value of the exponent n suggests that the transport of solvent is most likely diffusion

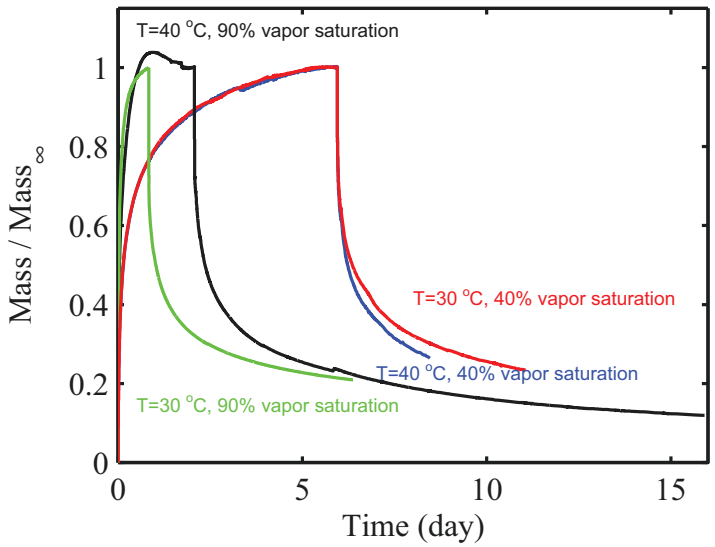

Figure 9.3: The experimental mass uptake/release during sorption/desorption of cyclohexane in asphaltenes.

limited with a concentration-dependent diffusion coefficient. The low value of the exponent suggests that cyclohexane diffusion in asphaltenes is not limited by swelling of film. This result can be explained by either fast swelling of the film relative to diffusion of cyclohexane or availability of molecular free volume in the medium in the solvent-free phase. Usually when swelling limits the sorption phase, sorption kinetics are slower than desorption because shrinkage during desorption may not occur while swelling does occur during sorption[198].

Table 9.3: Result of fitting Eq. 9.1 on sorption/desorption data

Experiment	T (°C)	Vap. Sat. (%)	k (s^{-n})	n (-)
Sorption	30	40	0.19	0.2
	30	90	0.28	0.2
	40	40	0.17	0.2
	40	90	0.25	0.2
Desorption	30	40	0.22	0.14
	30	90	0.3	0.14
	40	40	0.22	0.13
	40	90	0.25	0.13

As our results show (see Figure 9.6 and discussion there), any relaxation of the asphaltenes occurs after saturation of the film with cyclohexane which is a sign that swelling is not faster than diffusion. On the other hand, the prepared films were dried at a temperature below the glass transition temperature of asphaltene materials (usually 120 °C and

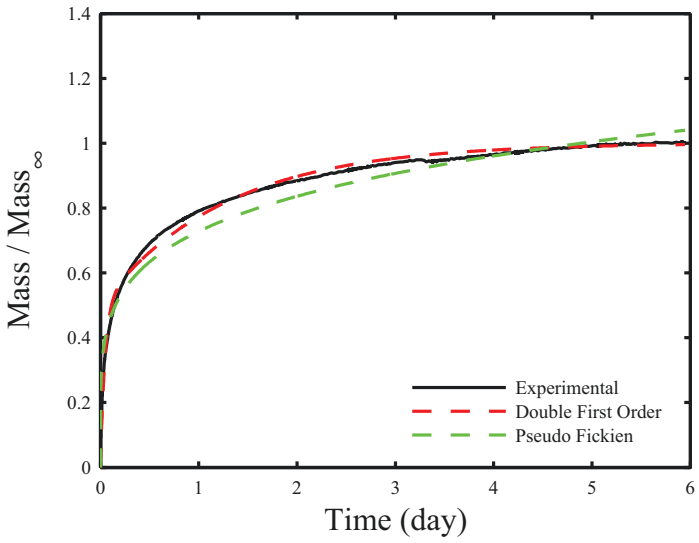

Figure 9.4: Fitting of double-first order kinetics on the sorption data at T=40 °C and 40 % vapor saturation.

above[202]) which makes it impossible for the film to relax to a compact structure in the last stages of the drying. Upon evaporation of methylene chloride used to cast the film, there was likely some extra free volume left in the film and upon arrival of the cyclohexane molecules, there is no need for asphaltene film to swell to create open space for the solvent molecules to diffuse in.

In Figure 9.4, a typical fitting of a double-first order kinetic equation to data for sorption at 40 °C and 40% vapor saturation is shown. This model provides a good fit to the data, which suggests that at least two different kinetic processes are involved in the sorption/desorption. In all cases, the double-first order kinetics fitted the experimental data well, and the resulting values for the mass fraction and kinetic constants are summarized in Table 9.4.

Table 9.4: Summary of fitting a double-first order kinetics on sorption desorption data

Experiment	T (°C)	Vap. Sat. (%)	ϕ (-)	k_1 (s^{-1})	k_2 (s^{-1})
Sorption	30	40	0.55	0.015	0.003
	30	90	0.70	0.020	0.004
	40	40	0.50	0.015	0.00055
	40	90	0.52	0.020	0.003
Desorption	30	40	0.49	0.0120	0.0002
	30	90	0.58	0.0092	0.0001
	40	40	0.50	0.0092	0.0002
	40	90	0.58	0.0042	0.0001

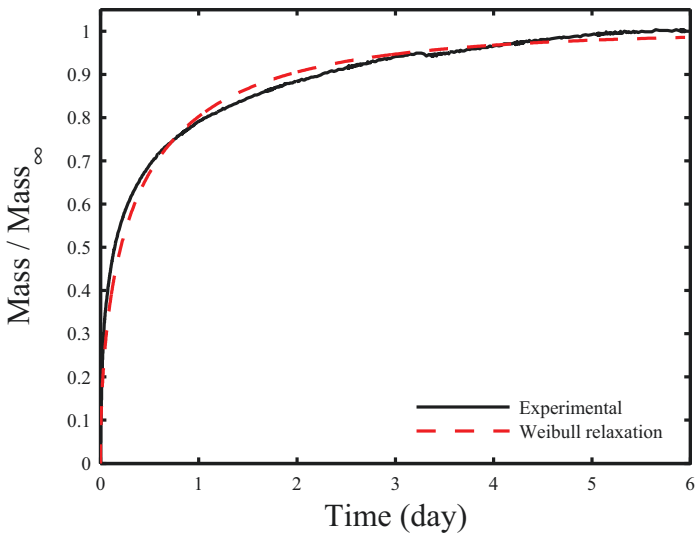

Figure 9.5: Result of fitting Weibull relaxation model on the sorption data at 40 °C and 40% vapor saturation.

As discussed in the previous section, resistance to mass transfer in the gas phase is not the limiting factor. The significant decrease between k_1 and k_2 in the solvent transport rate may be attributed to surface activity of the asphaltenes. For example, hydrophobic/hydrophilic interaction at the surface of the film might retard the initial adsorption of the solvent on the film. But in this case the initial stage should be slower and the second stage should be faster, whereas our data indicate that initial phase of transport (in both sorption and desorption) is faster. An alternate explanation is that a structural change in the asphaltene film during sorption/desorption can be the source of different rates observed. To test this hypothesis, we fitted the data with a Weibull relaxation model, which can account for the relaxation of the sample. A typical fitting of the Weibull model for 40 °C and 40% vapor saturation is shown in Figure 9.5. Detailed analysis of the sum of the squared residuals shows that this model can represent data (in all cases), even better than double-first order kinetics. The summary for Weibull relaxation model fitting is tabulated in Table 9.5.

The possibility that the asphaltene film undergoes a structural relaxation during sorption is consistent with the repeatable overshoot in sorption mass uptake. In Figure 9.6 a clear overshoot in mass uptake of sorption data at 40 °C and 90% vapor saturation can be detected. The source of such an overshoot in a sorption mass uptake can be attributed to [203–205]:

- Solvent induced crystallization.

- Penetrant induced melting and recrystallization.
- Release of indigenous components.
- Slow relaxation of the sorbent to a more compact structure.

Table 9.5: Summary of fitting Weibull relaxation model to sorption/desorption data.

Experiment	T (°C)	Vap. Sat. (%)	k (s^{-1})	ξ (-)
Sorption	30	40	0.002	0.5
	30	90	0.02	0.45
	40	40	0.0017	0.54
	40	90	0.007	0.72
Desorption	30	40	0.0005	0.3
	30	90	0.004	0.40
	40	40	0.0007	0.3
	40	90	0.0007	0.3

As all the films were thermally treated before experiments, any volatile components were released before the experiments. As asphaltenes are known to be mixture of glassy (amorphous) and crystalline phases[202] either relaxation or crystallization induced by solvent can explain the observed overshoot.

To investigate this phenomenon, we repeated a second cycle of sorption/desorption on the same film, and overshoot consistently occurred each time. If the solvent-induced crystallization was the reason behind the overshoot, it should be observed only in the first cycle. This result is an indication that crystallization cannot be the cause of the observed overshoot. We suggest that the observed overshoot in mass uptake is due to solvent-induced relaxation of the amorphous phase in asphaltenes toward more compact structure. This mechanism is in agreement with results of previous analysis with Eq. 9.1, where no sign of swelling was observed. If we accept this mechanism, then the hysteresis of the sorption/desorption curves is due to solvent molecules diffusing through a more compact medium during desorption than sorption, giving a slower rate process.

9.4.2 Estimation of apparent diffusion coefficients

Analysis the data in previous section indicates that a single, constant diffusion coefficient cannot fit the data well. As illustrated in Figure 9.7, the fit of a constant diffusion coefficient in Eq. 9.2 is poor. The initial stage of uptake is much faster and final stage is much slower than the simple diffusion model.

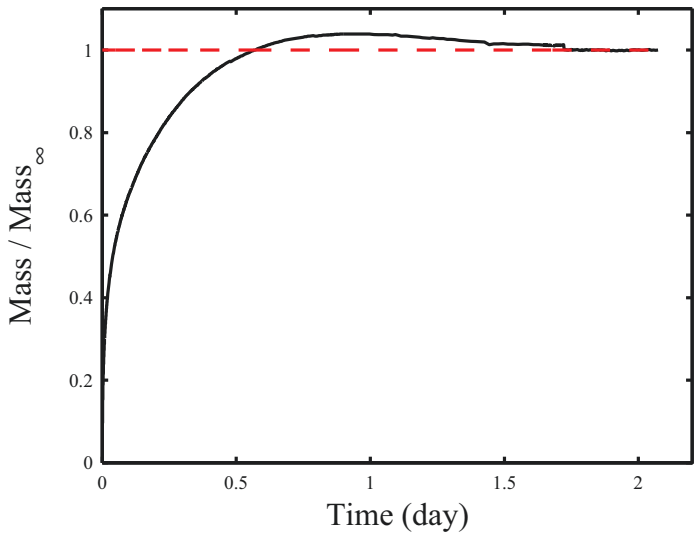

Figure 9.6: Overshoot in the sorption data at 40 °C and 90% vapor saturation.

To our knowledge, no diffusion coefficients have been reported in the literature for solvents in asphaltenes. The closest analogy in the literature is extracted bitumen. Salama and Kantzas [197] reported the diffusion coefficients of normal alkanes (C_6, C_7 and C_8) in bitumen using X-ray tomography. They reported that diffusion coefficient increased from $4 * 10^{-11}$ to $2 * 10^{-9}$ (m^2/s) as the solvent fraction increased from 0 to 1. Accordingly, we used Eq. 9.4 for diffusion coefficients to fit the data. The results are shown in Figure 9.8. Unlike the results of Salama and Kantzas, during sorption the diffusion coefficient decreased with increasing solvent concentration, which is consistent with structural relaxation of the asphaltene film as discussed previously. The data of Figure 9.8 also shows significant hysteresis between sorption and desorption. The calculated diffusion coefficient is two orders of magnitude smaller for desorption. Another interesting observation is that the diffusion coefficient during sorption is more dependent on vapor saturation than temperature.

Results of a more flexible model for diffusion coefficient (Eq. 9.5) are shown in Figure 9.9. This functionality resulted in a better fit of the experimental data in the sense of sum of the squared residuals (5% improvement on average). The order of magnitude for diffusion coefficients using Eq. 9.5 is not significantly different from the results with Eq. 9.4, but some new patterns emerge. The most important change is the predicted minimum for diffusion coefficient during desorption which happens at 20% of the C_max. Another interesting result is that diffusion coefficient during desorption is almost constant with temperature and only changes with concentration.

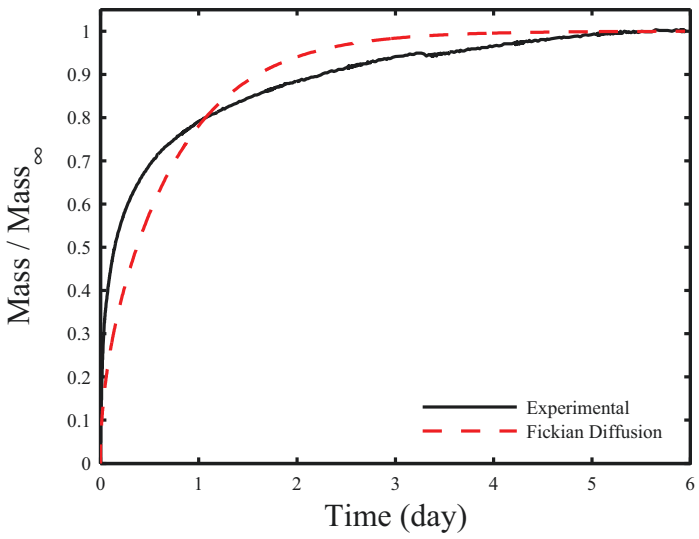

Figure 9.7: Fitting sorption data at 40 °C and 40% vapor saturation with constant diffusion coefficient. The diffusion coefficient is $4 * 10^{-11}$ m^2/s

Table 9.6: Optimized parameter for Eq. 9.4.

Experiment	Vap. Sat. (%)	T (°C)	$D_0 * 10^{12}$ (m^2/s)	$\alpha * 10^2$	β
Sorption	40	30	0.25	111.4	15.1
		40	0.8	1.44	0.78
	90	30	1.9	2.1	2.0
		40	2.7	1.64	0.50
Desorption	40	30	0.3	2.8	-2.3
		40	0.3	41.3	-16.1
	90	30	0.1	6.2	-2.3
		40	0.2	36.2	-25.1

9.5 Discussion

Beside the complexities observed in the sorption/desorption of cyclohexane on the asphaltenes, current data give a range of apparent diffusion coefficients for cyclohexane in asphaltenes to be 10^{-14}-10^{-16} and 10^{-15}-10^{-18} (m^2/s) for sorption and desorption, respectively. As there is no experimental data reported on diffusion of solvents in the asphaltenes (to the best knowledge of the authors), we compared these diffusion coefficients with the closest material to asphaltenes, oilsands bitumen. Table 9.8 summarizes diffusion coefficients reported in the literature. The most striking feature of this set of data is that diffusion coefficients of the cyclohexane in asphaltenes are orders of magnitudes smaller

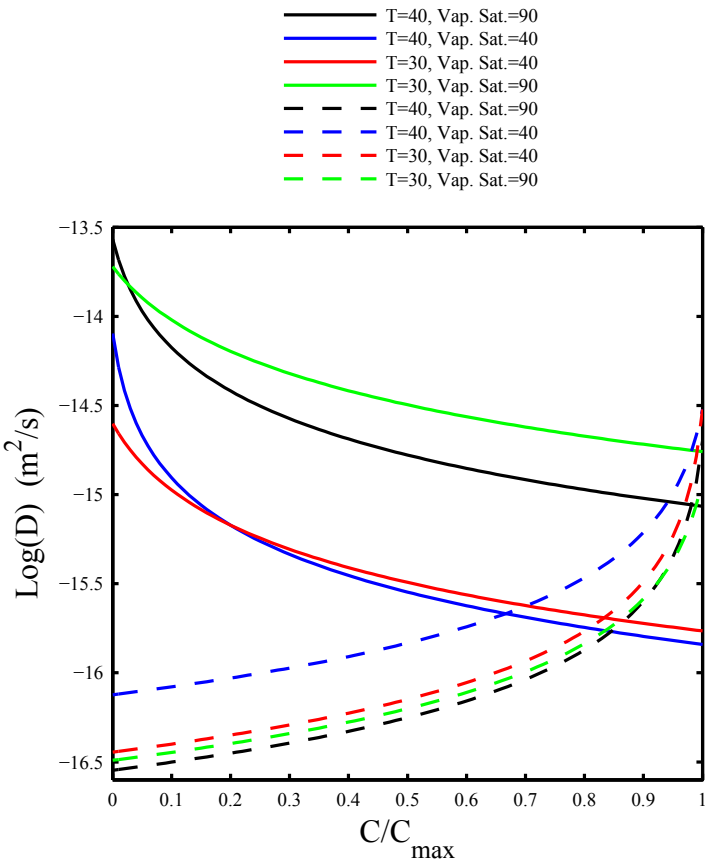

Figure 9.8: Calculated diffusion coefficient versus concentration of cyclohexane in the film using Eq. 9.4. The C_max values can be found in Table 9.2. Solid Lines represent D from sorption data while dashed lines represent D from desorption data. For the parameter see Table 9.6.

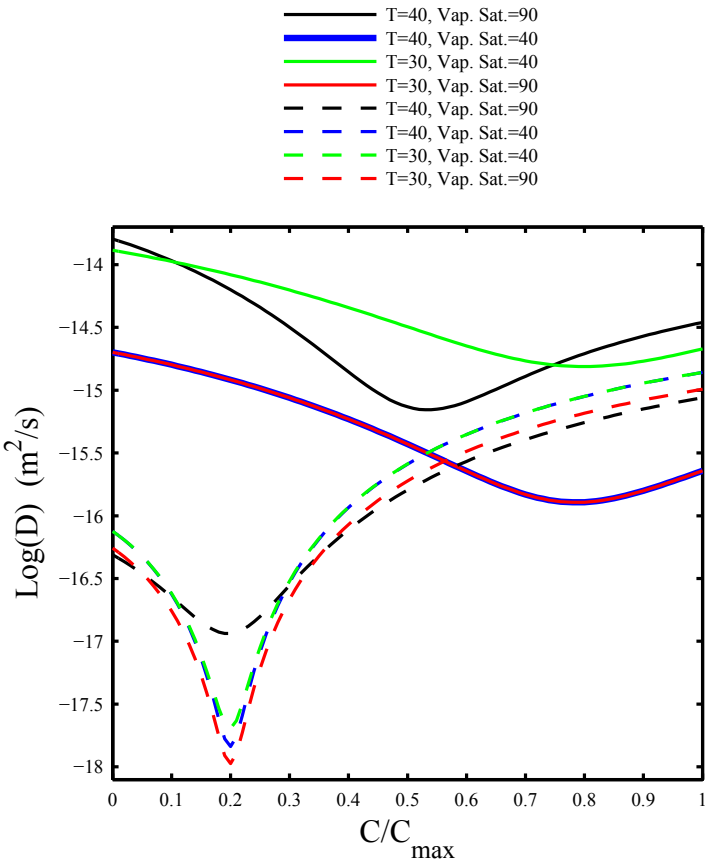

Figure 9.9: Calculated Diffusion coefficient versus concentration of cyclohexane in the film using Eq. 9.5. The C_max values can be found in Table 9.2. Solid Lines represent D from sorption data while dashed lines represent D from desorption data. For the parameter see Table 9.7.

than the values in bitumen. Lower values can be attributed to the larger size of the solvents molecules[1] and the higher density of asphaltenes with respect to bitumen. Higher density implies less free volume available for diffusion of solvent.

[1]Linear molecules like n alkanes need less free volume to diffuse. Also the aromatic compounds due to their planar structure need less free volume for diffusion with respect to the chair or boat structure of cyclohexane[196].

Table 9.7: Optimized parameter for Eq. 9.4.

Experiment	Vap. Sat. (%)	T (°C)	$D_0 * 10^{14}$ (m^2/s)	$\alpha * 10^2$	β	γ
Sorption	40	30	1.3	-1.8	1.3	0.9
		40	0.2	-1.7	1.5	0.8
	90	30	0.2	-1.7	1.5	0.8
		40	1.6	-126.8	2.7	0.5
Desorption	40	30	0.0075	1610	-2.3	33.4
		40	0.0075	1610	-2.3	33.4
	90	30	0.0055	1610	-2.3	33.4
		40	0.0049	1730	-2.0	34.0

The only concern about the diffusion coefficient data is the uncertainty in the calculation of the gradients of concentration in the film during the estimation of the diffusion coefficients. The total mass change during sorption/desorption can be calculated using:

$$\dot{m}(t) = \int_0^{\delta} A_{film}\rho_{AS}\frac{\partial C}{\partial t}dx \tag{9.9}$$

So using Eq. 9.2, the total mass uptake/release would be:

$$\dot{m}(t) = A_{film}\rho_{AS}D_{AS}(C)\frac{\partial C}{\partial x}\bigg|_{x=\delta} \tag{9.10}$$

In these experiments, we only have the concentration at the boundary ($x = \delta$) and the total mass of solvent. No matter what function has been chosen for the dependence of diffusion coefficient on concentration, there would be a concentration profile which will results in good fitting of the data. Experiments with thinner films than 7 µm are not practical due to error in mass measurement, and thicker films compound the problem unless a method were available for measuring gradients directly.

Table 9.8: Summary of diffusion coefficient of light hydrocarbons in bitumen and asphaltenes.

Medium	Solvent	Temperature (°C)	Density of Medium (kg/m^3)	Method	Diffusion Coefficient (m^2/s)	Reference
Athabasca bitumen	n-butane	25	1001	-	10^{-11}-10^{-9}	[206]
Bitumen[a]	pentane	24	1028	X-ray view-cell apparatus	10^{-11}	[207]
Athabasca bitumen	pentane	22	1000	X-ray Computer Assisted Tomography	10^{-10}	[208]
Athabasca bitumen	pentane	22	1000	X-ray Computer Assisted Tomography	10^{-10}	[209]
Bitumen	n-hexane	25	978	X-ray Computer Assisted Tomography	$5 * 10^{-11}$-$8.4 * 10^{-9}$	[197]
Semi-solid bitumen	hexane	25	-	Chromatography	$8.6 * 10^{-12}$	[196]
Semi-solid bitumen	iso-hexane	25	-	Chromatography	$6.3 * 10^{-12}$	[196]
Semi-solid bitumen	cyclohexane	25	-	Chromatography	$2.4 * 10^{-12}$	[196]
Asphaltenes	cyclohexane	30-40	1200	Gravimetric	10^{-14}-10^{-16}	Current Study[b]
Asphaltenes	cyclohexane	30-40	1200	Gravimetric	10^{-15}-10^{-18}	Current Study[c]
Athabasca bitumen	toluene	21	1026	Optical microscopy and image analysis	10^{-11}-$2 * 10^{-10}$	[210]
Semi-solid bitumen	toluene	25	-	Chromatography	$6.8 * 10^{-12}$	[196]
Bitumen	phenol	22	1000	Colorimetric method	$4 * 10^{-12}$	[195]
Cold Lake bitumen	heptane	22	1000	X-ray Computer Assisted Tomography	10^{-10}	[209]
Bitumen	heptane	20	981	X-ray Computer Assisted Tomography	$5 * *10^{-11}$-$1.5 * 10^{-9}$	[211]
Cold Lake bitumen	heptane	-	1000	NMR	$7 * 10^{-12}$-$2 * 10^{-10}$	[212]
Bitumen	n-heptane	25	978	X-ray Computer Assisted Tomography	$4 * 10^{-11}$-$7.4 * 10^{-9}$	[197]
Bitumen	n-octane	25	978	X-ray Computer Assisted Tomography	$2 * 10^{-11}$-$6.4 * 10^{-9}$	[197]

[a] (Atmospheric residue) From later stage of naphtha removal and it contains more asphaltenes than bitumen.
[b] Sorption
[c] Desorption

9.6 Conclusion

In this work, the transport of the cyclohexane (as a candidate for non-aqueous solvent extraction of oil sands) in asphaltenes has been studied for the first time, giving an estimate of the apparent diffusion coefficient of 10^{-14}-10^{-16} for sorption and 10^{-15}-10^{-18} (m^2/s) for desorption. The apparent diffusion coefficient is concentration-dependent and changes by two orders of magnitude for a narrow range of concentration. The hysteresis between sorption and desorption suggests that there is a fundamental difference between sorption and desorption mechanisms. As sorption is faster than desorption and the film relaxation kinetics is slower than solvent diffusion, we can conclude that there is no swelling in the asphaltenes from sorption of the solvent. The observed overshoot in mass uptake during sorption experiments suggests that a relaxation process is triggered in the asphaltenes by presence of the solvent.

Chapter 10

Conclusion and future works

10.1 Conclusion

The problem of polymer/solvent mutual diffusion, with so many applications, was introduced and mathematically formulated. Upon analysis using non-linear thermodynamics, the problem was reduced to determine self diffusion coefficients of the polymer and solvent as well as the Flory-Huggins interaction parameter of the corresponding binary system. As MD -a powerful method with atomistic resolution- was selected to study both quantities, an introduction to the simulation theory and method was provided. And the next step was to conduct extensive molecular dynamics and first principle simulations to validate and modify the simulation protocol and selected force field, OPLS-AA. After fine tuning the procedure, the mechanism of solvent diffusion in PVA, the selected polymer, was studied using MD simulation. Results of this study revealed that solvent self diffusion is more correlated with free volume available for the solvents molecule. With insight provided by these results, free volume theory was found to be the most appropriate choice for modeling the solvent self diffusion. As parametrization of the free volume theory is not a trivial task, both experimentally and by simulation, the lattice free volume theory, as an exact alternative, was used to correlate the data. For parametrization of this new formalism of the free volume theory, the Sanchez-Lacombe equation of state was parametrized using molecular dynamics simulation. Up to this point, the first task, determining the self diffusion coefficients of the solvents in PVA, was successfully achieved. To complete the problem of of predicting the mutual diffusion coefficients of polymer/solvent systems, there are two more steps of calculations required which are planned for the future work. In the next section, the summary of these steps are presented.

10.1.1 Original contributions Summary

- OPLS-AA force field was validated for pure PVA.
- Atomic partial charges in OPLS-AA force field were modified to describe the interaction between PVA and selected solvents.

- Self diffusion coefficients of the selected solvents were estimated in wide range of temperature and concentration in PVA.
- The free volume redistribution as main mechanism of the solvents diffusion was estimated and inconsistencies reported in the literature with this regard were addressed.
- Free volume theory as a reasonable candidate was parameterized to correlate the solvent self diffusion coefficient with system variables.
- It was found that for glassy region a modified version of the free volume theory os required.

10.2 Future work

For the evaluation of the mutual diffusion coefficients of polymer/solvent systems using Equation 2.16, we should calculate the Flory-Huggins interaction parameters of the PVA/solvent systems. Even though this part of calculation has been done using the original OPLS-AA parameters, preliminary results were not satisfactory. Clarification of the source of this inconsistency with experimental expectations was the initial motive behind the calculations in Chapter 6. Now that reliable PACs for PVA are available, the next step is to re-evaluate the interaction parameters. After providing a reasonable estimate of the interaction parameters, the mutual diffusion coefficients can then be easily calculated using Equation 2.16.

Having the mutual diffusion coefficients of polymer/solvent systems, the data needs to be validated against the experimental data. So, another step is to measure mutual diffusion coefficients of PVA/solvent systems using the technique of IGA as described in the case of asphaltenes/cyclohexane in Chapter 9. On the other hand, MD simulation of a non-equilibrium system consisting polymer/solvent double layer can provide insightful information for the correlation of the simulation and experimental data.

Beside these essential parts to complete determination of mutual diffusion, we faced several interesting problems that we tried to address in the course of this project (but we never found chance to complete or publish the data). We believe that understanding and solving these problems (even though indirectly) can greatly facilitate future research on this topic (or any other problem of similar nature). Here, we present a short list of these problems:

- We studied the diffusion of gaseous species especially oxygen, methane and carbon dioxide in PVA matrix using the same procedure described in Chapter 7. It is known that water content of the matrix can greatly affect the mobility of the gases in the PVA. As we have access to the trajectory of a fully equilibrated PVA/water system, by simply measuring diffusion coefficients of these gases in the wet PVA, a complete

understanding of the underlying mechanism can be obtained. Results of this study are crucial for the applications of PVA in contact lenses and food packaging.

- In most of its applications, PVA is cross linked using a chemical agent named glutaraldehyde. Recently, we have developed a model of such a system at different cross linking density. Preliminary analysis on the system indicates that our model is a good representative of the real sample. As our results indicates, properties of PVA are very sensitive to cross linking density even at low level (less than 1%). So, it is worth repeating the calculation of self diffusion coefficients on the cross linked polymer to evaluate the effect of the constraints added to the chain mobility on the solvent dynamics.

- Experimentally, it is known that PVA properties, especially its density and crystalline structure, are highly affected by the tacticity of the chain. Unfortunately, our simulation results (presented in Chapter 5) using small system size could not effectively capture this effect. Accordingly, we started an extensive study on the problem using a properly sized system and carefully tuned protocol to capture this effect. These simulations are half way through and results are promising to address this problem with atomistic resolution for the first time.

Bibliography

[1] C. Wohlfarth, CRC Handbook of Phase Equilibria and Thermodynamic Data of Aqueous Polymer Solutions, 2012.

[2] Q. G. Zhang, Q. L. Liu, Y. Chen, J. Y. Wu, A. M. Zhu, Chemical Engineering Science 64 (2009) 334–340.

[3] F. Muller-Plathe, Journal of Membrane Science 141 (1998) 147–154.

[4] J. Jang, D. K. Lee, Polymer 44 (2003) 8139–8146.

[5] J. Pritchard, Poly(vinyl Alcohol): Basic Properties and Uses(Polymer Monographs, Volume 4), Routledge, 1970.

[6] E. Rossinsky, K. B. Tarmyshov, M. C. Bohm, F. Muller-Plathe, Macromolecular Theory and Simulations 18 (2009) 545–552.

[7] G. Karlsson, U. Gedde, M. Hedenqvist, Polymer 45 (2004) 3893–3900.

[8] J. Crank, The Mathematics of Diffusion, Oxford Science Publications, second edition, 1975.

[9] P. Neogi, Diffusion in Polymers (Plastics Engineering), Marcel Dekker, Inc., New York, NY, first edition, 1996.

[10] L. Darken, Metals Technology (1948) 184–194.

[11] P. F. Green, Kinetics, Transport, and Structure in Hard and Soft Materials, CRC Press; 1 edition, 2005.

[12] G. S. Hartley, J. Crank, Transactions of the Faraday Society 45 (1949) 801–818.

[13] M. H. Cohen, D. Turnbull, The Journal of Chemical Physics 31 (1959) 1164.

[14] M. A. Islam, Physica Scripta 120 (2004) 120125.

[15] W. Ebeling, Acta Physica Polonica ... 39 (2008) 1003–1019.

[16] A. Poupon, Current opinion in structural biology 14 (2004) 233–41.

[17] F. M. Richards, Journal of Molecular Biology 82 (1974) 1–14.

[18] B. Gellatly, J. Finney, Journal of Molecular Biology 161 (1982) 305–322.

[19] S. Sastry, D. Corti, P. Debenedetti, F. Stillinger, Physical Review E 56 (1997) 5524–5532.

[20] H. J. C. Berendsen, J. P. M. Postma, W. F. van Gunsteren, a. DiNola, J. R. Haak, The Journal of Chemical Physics 81 (1984) 3684.

[21] W. G. Hoover, Physical Review A 31 (1985) 1695–1697.

[22] D. van der Spoel, E. Lindahl, B. Hess, t. G. development Team, GROMACS User Manual version 4.6.1, 2013.

[23] M. Abraham, D. van der Spoel, E. Lindahl, B. Hess, GROMACS User Manual version 5.0, 2014.

[24] M. P. Allen, D. J. Tildesley, Computer Simulation of Liquids, Oxford University Press, USA, 1989.

[25] W. L. Jorgensen, D. S. Maxwell, J. Tirado-rives, Journal of American Chemical Society 118 (1996) 11225–11236.

[26] J. Tomasi, B. Mennucci, R. Cammi, Chemical reviews 105 (2005) 2999–3093.

[27] M. R. Shirts, J. D. Chodera, The Journal of Chemical Physics 129 (2008) 124105.

[28] P. Echenique, J. L. Alonso, Molecular Physics 105 (2007) 3057–3098.

[29] A. C. Phillips, INTRODUCTION TO QUANTUM MECHANICS, John Wiley & Sons Ltd, New York, 2003.

[30] E. G. Lewars, Computational Chemistry, Springer, London, second edi edition, 2010.

[31] F. Jensen, Introduction to Computational Chemistry, John Wiley & Sons Ltd, New York, second edi edition, 2007.

[32] V. Magnasco, Methods of Molecular Quantum Mechanics, John Wiley & Sons Ltd, New York, 2009.

[33] J. H. Jensen, Molecular Modeling Basics, Taylor & Francis Group, Boca Raton, 2010.

[34] W. J. Hehre, Molecular Mechanics and Quantum Chemical Calculations, Wavefunction, Inc., Irvine, 2003.

[35] J. B. Foresman, A. Frisch, Exploring Chemistry with Electronic Structure Methods, Gaussian, Inc., Pittsburgh, second edi edition, 1996.

[36] D. S. Sholl, J. A. Steckel, Density Functional Theory: A Practical Introduction, volume 68, John Wiley & Sons, 2009.

[37] P. Hohenberg, W. Kohn, Physical review 155 (1964).

[38] M. Levy, Physical Review A 26 (1982) 1200.

[39] W. Kohn, L. Sham, Physical Review 140 (1965) A1133–38.

[40] W. J. Hehre, L. Radom, P. v. R. Schleyer, J. Pople, AB INITIO Molecular Orbital Theory, John Wiley & Sons Ltd, New York, 1986.

[41] G. E. S. M. J. Frisch, G. W. Trucks, H. B. Schlegel, B. M. M. A. Robb, J. R. Cheeseman, G. Scalmani, V. Barone, H. P. H. G. A. Petersson, H. Nakatsuji, M. Caricato, X. Li, M. H. A. F. Izmaylov, J. Bloino, G. Zheng, J. L. Sonnenberg, T. N. M. Ehara, K. Toyota, R. Fukuda, J. Hasegawa, M. Ishida, J. Y. Honda, O. Kitao, H. Nakai, T. Vreven, J. A. Montgomery, E. B. J. E. Peralta, F. Ogliaro, M. Bearpark, J. J. Heyd, J. N. K. N. Kudin, V. N. Staroverov, T. Keith, R. Kobayashi, J. T. K. Raghavachari, A. Rendell, J. C. Burant, S. S. Iyengar, J. B. C. M. Cossi, N. Rega, J. M. Millam, M. Klene, J. E. Knox, R. E. S. V. Bakken, C. Adamo, J. Jaramillo, R. Gomperts, J. W. O. O. Yazyev, A. J. Austin, R. Cammi, C. Pomelli, G. A. V. R. L. Martin, K. Morokuma, V. G. Zakrzewski, A. D. D. P. Salvador, J. J. Dannenberg, S. Dapprich, J. C. O. Farkas, J. B. Foresman, J. V. Ortiz, Fox, D. J., Gaussian 09 Revision C.01, 1999.

[42] A. Ruzsinszky, C. V. Alsenoy, Journal of Physical Chemistry A 106 (2002) 12139–12150.

[43] B. H. Besler, K. M. Merz, P. a. Kollman, Journal of Computational Chemistry 11 (1990) 431–439.

[44] U. C. Singh, P. a. Kollman, Journal of Computational Chemistry 5 (1984) 129–145.

[45] P. H. Berens, D. H. J. Mackay, G. M. White, K. R. Wilson, The Journal of Chemical Physics 79 (1983) 2375–89.

[46] E. Chiessi, F. Cavalieri, G. Paradossi, The journal of physical chemistry. B 109 (2005) 8091–6.

[47] G. E. Karlsson, T. S. Johansson, U. W. Gedde, M. S. Hedenqvist 41 (2002) 185–206.

[48] F. Muller-Plathe, W. F. van Gunsteren, Polymer 38 (1997) 2259–2268.

[49] R. Fossheim, Acta Chemica Scandinavica 52 (1998) 603–607.

[50] K. Masuda, H. Kaji, F. Horii, Journal of Polymer Science: Part B: Polymer Physics 38 (2000) 1–9.

[51] A. De La Rosa, L. Heux, J. Y. Cavaille, K. Mazeau, Polymer 43 (2002) 5665–5677.

[52] F. Pan, F. Peng, Z. Jiang, Chemical Engineering Science 62 (2007) 703–710.

[53] S. S. Jawalkar, K. V. S. N. Raju, S. B. Halligudi, M. Sairam, T. M. Aminabhavi, The Journal of Physical Chemistry B 111 (2007) 2431–9.

[54] H. Sun, Journal of Physical Chemistry 102 (1998) 7338–7364.

[55] S. S. Jawalkar, S. G. Adoor, M. Sairam, M. N. Nadagouda, T. M. Aminabhavi, The journal of physical chemistry. B 109 (2005) 15611–20.

[56] S. S. Jawalkar, T. M. Aminabhavi, Polymer 47 (2006) 8061–8071.

[57] M. Belmares, M. Blanco, W. a. Goddard, R. B. Ross, G. Caldwell, S.-H. Chou, J. Pham, P. M. Olofson, C. Thomas, Journal of computational chemistry 25 (2004) 1814–26.

[58] B. Hess, C. Lutzner, v. d. S. David, E. Lindhal, Journal of Chemical Theory and Computation 4 (2008) 435–447.

[59] D. V. Spoel, E. Lindahl, B. Hess, G. Groenhof, A. E. Mark, H. J. C. Berendsen, Journal of Computational Chemistry 26 (2005) 1701–1718.

[60] U. Essmann, L. Perera, M. L. Berkowitz, T. Darden, H. Lee, L. G. Pedersen, The Journal of Chemical Physics 103 (1995) 8577.

[61] E. Lindahl, B. Hess, D. van der Spoel, Journal of Molecular Modeling 7 (2001) 306–317.

[62] H. Berendsen, D. van der Spoel, R. van Drunen, Computer Physics Communications 91 (1995) 43–56.

[63] C. Wu, Polymer 51 (2010) 4452–4460.

[64] W. D. Cornell, P. Cieplak, C. I. Bayly, I. R. Gould, K. M. Merz, D. M. Ferguson, D. C. Spellmeyer, T. Fox, J. W. Caldwell, P. a. Kollman, Journal of the American Chemical Society 117 (1995) 5179–5197.

[65] M. Parrinello, A. Rahman, Journal of Applied Physics 52 (1981) 7182.

[66] N. Metatla, A. Soldera, Molecular Simulation 32 (2006) 1187–1193.

[67] Accelry Inc, Materials Studio4.0, 2005.

[68] P. J. Flory, F. S. Leutner, Journal of Polymer Science 3 (1948) 880–890.

[69] D. N. Theodorou, U. W. Suter, Macromolecules 18 (1985) 1467–1478.

[70] Y. Tamai, H. Tanaka, K. Nakanishi, Macromolecules 29 (1996) 6761–6769.

[71] D. Bloch, Polymer Handbook, 4th Edition, Wiley-Interscience, 1999.

[72] D. R. Lide (Ed.), CRC Handbook of Chemistry and Physics, CRC-Press, 1998.

[73] J. E. Mark, Polymer Data Handbook, Oxford University Press, USA, 2009.

[74] D. Walsh, P. Zoller, Standard Pressure Volume Temperature Data for Polymers (9781566, 1995.

[75] J. Han, R. H. Gee, R. H. Boyd, Macromolecules 27 (1994) 7781–7784.

[76] W. L. Jorgensen, J. Chandrasekhar, J. D. Madura, R. W. Impey, M. L. Klein, The Journal of Chemical Physics 79 (1983) 926–35.

[77] J. L. F. Abascal, C. Vega, Journal of Chemical Physics 123 (2005) 234505.

[78] D. Rigby, R.-J. Roe, The Journal of Chemical Physics 87 (1987) 7285.

[79] H. Schreiber, O. Steinhauser, Biochemistry 31 (1992) 5856–5860.

[80] P. E. Smith, B. M. Pettitt, The Journal of Chemical Physics 105 (1996) 4289.

[81] D. a. C. Beck, R. S. Armen, V. Daggett, Biochemistry 44 (2005) 609–16.

[82] U. Leute, W. Dollhopf, E. Liska, Colloid and polymer science 254 (1976) 237–246.

[83] F. Peng, L. Lu, H. Sun, Y. Wang, J. Liu, Z. Jiang, Chemistry of Materials 17 (2005) 6790–6796.

[84] A. Stavropoulou, K. G. Papadokostaki, M. Sanopoulou, Journal of Applied Polymer Science 93 (2004) 1151–1156.

[85] O. W. Guirguis, M. T. H. Moselhey, Natural Science 04 (2012) 57–67.

[86] M. Krumova, R. Benavente, C. Mijangos, J. M. Peren, Polymer 41 (2000) 9265–9272.

[87] J.-S. Park, J.-W. Park, E. Ruckenstein, Journal of Applied Polymer Science 82 (2001) 1816–1823.

[88] J. Rault, R. Gref, Z. H. Ping, Q. T. Nguyen, J. Neel, Polymer 36 (1995) 1655–1661.

[89] P. Y. Choi, T. A. Kavassalis, A. Rudin, Journal of colloid and interface science 150 (1992) 386–393.

[90] P. Choi, Macromolecular Rapid Communications 23 (2002) 484–487.

[91] J. H. Choi, S.-W. Ko, B. C. Kim, J. Blackwell, W. S. Lyoo, Macromolecules 34 (2001) 2964–2972.

[92] M. Shiga, W. Shinoda, The Journal of chemical physics 123 (2005) 134502.

[93] D. Noid, B. Sumpter, B. Wunderlich, Analytica Chimica Acta 235 (1990) 143–153.

[94] S.-T. Lin, M. Blanco, W. a. Goddard, The Journal of Chemical Physics 119 (2003) 11792–805.

[95] T. a. Pascal, S.-T. Lin, W. a. Goddard, Physical chemistry chemical physics 13 (2011) 169–81.

[96] C. Caleman, P. J. V. Maaren, M. Hong, J. S. Hub, L. T. Costa, D. V. D. Spoel, Journal of chemical theory and computation 8 (2012) 61–74.

[97] P. Patel, F. Rodriguez, Journal of Applied Polymer Science 23 (1979) 2335–2342.

[98] F. Muller-Plathe, The Journal of Chemical Physics 108 (1998) 8252.

[99] S. Pricl, M. Fermeglia, Chemical Engineering Communication 190 (2003) 1267–1292.

[100] C. Caddeo, A. Mattoni, Macromolecules 46 (2013) 8003–8008.

[101] Q. G. Zhang, Q. L. Liu, J. Lin, J. H. Chen, A. M. Zhu, Journal of Materials Chemistry 17 (2007) 4889.

[102] J. B. Durkee, Metal Finishing 102 (2004) 42–50.

[103] S. S. Jawalkar, S. G. Adoor, M. Sairam, M. N. Nadagouda, T. M. Aminabhavi, The Journal of Physical Chemistry B 109 (2005) 15611–20.

[104] S. Patel, A. Lavasanifar, P. Choi, Biomacromolecules 9 (2008) 3014–23.

[105] H. E. Assendert, A. H. Windle, Polymer 39 (1998) 4295–4302.

[106] E. Chiessi, F. Cavalieri, G. Paradossi, The Journal of Physical Chemistry B 111 (2007) 2820–7.

[107] C. Hassan, N. Peppas, Advances in Polymer Science 153 (2000) 37–65.

[108] S. Jeck, P. Scharfer, M. Kind, Journal of Membrane Science 417-418 (2012) 154–162.

[109] K. Matyjaszewski, Encyclopedia Of Polymer Science and Technology 8 (2002) 399–437.

[110] Y. T. Suchiya, N. Y. Oshii, T. I. Watsubo, Japanese Journal of Applied Physics 43 (2004) 5676–5681.

[111] G. Tesei, G. Paradossi, E. Chiessi, The Journal of Physical Chemistry B 116 (2012) 10008–19.

[112] H. Watanabe, R. Koyama, N. Hiroshi, A. Nishioka, Journal of polymer science 62 (1962) 77–81.

[113] T. Takigawa, H. Kashihara, K. Urayama, T. Masuda, Polymer 33 (1992) 2334–2339.

[114] N.-x. Chen, J.-h. Zhang, Chinese Journal of Polymer Science 28 (2010) 903–911.

[115] G. Henkelman, A. Arnaldsson, H. Jónsson, Computational Materials Science 36 (2006) 354–360.

[116] S. J. Weiner, P. a. Kollman, D. T. Nguyen, D. a. Case, Journal of Computational Chemistry 7 (1986) 230–252.

[117] M. Basma, S. Sundara, D. Calgan, T. Vernali, R. J. Woods, Journal of Computational Chemistry 22 (2001) 1125–37.

[118] E. Sigfridsson, U. Ryde, Journal of Computational Chemistry 19 (1998) 377–395.

[119] A. Noorjahan, P. Choi, Polymer 54 (2013) 4212–4219.

[120] S. Genheden, P. Soderhjelm, U. Ryde, International Journal of Quantum Chemistry 112 (2012) 1768–1785.

[121] P. Soderhjelm, U. Ryde, Journal of computational chemistry 30 (2008) 750–760.

[122] R. S. Mulliken, The Journal of Chemical Physics 23 (1955) 1833.

[123] A. E. Reed, R. B. Weinstock, F. Weinhold, The Journal of Chemical Physics 83 (1985) 735.

[124] R. F. W. Bader, Atoms in Molecules: A Quantum Theory, Oxford University Press, Oxford, 1990.

[125] A. V. Marenich, S. V. Jerome, C. J. Cramer, D. G. Truhlar, Journal of Chemical Theory and Computation 8 (2012) 527–541.

[126] J. P. Ritchie, S. M. Bachrach, Journal of Computational Chemistry 8 (1987) 499–509.

[127] J. P. Ritchie, Journal of American Chemical Society 107 (1985) 1829–1837.

[128] F. L. Hirshfeld, Theoretica Chimica Acta 44 (1977) 129–138.

[129] F. J. Luque, J. M. López, M. Orozco, Theoretical Chemistry Accounts: Theory, Computation, and Modeling (Theoretica Chimica Acta) 103 (2000) 343–345.

[130] M. Wen, J. Jiang, Z.-X. Wang, C. Wu, Theoretical Chemistry Accounts 133 (2014) 1471.

[131] H. J. C. Berendsen, J. P. M. Postma, J. van Gunsteren, W. F. Hermans, in: B. Pullman (Ed.), Intermolecular Forces, D. Reidel Publishing Company, Dordrecht, 1981, pp. 331–342.

[132] J.-P. Ryckaert, G. Ciccotti, H. J. C. Berendsen, Journal of Computational Physics 23 (1977) 327–341.

[133] P. V. Klimovich, D. L. Mobley, Journal of computer-aided molecular design 24 (2010) 307–16.

[134] J. P. M. Jämbeck, A. P. Lyubartsev, The Journal of Physical Chemistry Letters 4 (2013) 1781–1787.

[135] R. W. Hockney, S. P. Goel, J. W. Eastwood, Jpurnal of Computational Physics 14 (1974) 148–158.

[136] T. Darden, D. York, L. Pedersen, The Journal of Chemical Physics 98 (1993) 10089.

[137] J. P. M. Jambeck, F. Mocci, A. P. Lyubartsev, A. Laaksonen, Journal of computational chemistry 34 (2013) 187–97.

[138] Z. Qiao, Y. Wu, X. Li, J. Zhou, Fluid Phase Equilibria 302 (2011) 14–20.

[139] J. Sacristan Bermejo, C. Mijangos Ugarte, The Journal of Chemical Physics 129 (2008) 154907.

[140] L. Masaro, X. Zhu, Progress in Polymer Science 24 (1999) 731–775.

[141] S. Sastry, T. M. Truskett, P. G. Debenedetti, S. Torquato, F. H. Stillinger, Molecular Physics 95 (1998) 289–297.

[142] R. Kumar, B. G. Sumpter, in: SciDAC, volume 8.

[143] D. Rigby, R. J. Roe, Macromolecules 23 (1990) 5312–5319.

[144] M. L. Greenfield, D. N. Theodorou, Macromolecules 26 (1993) 5461–5472.

[145] C. H. Rycroft, Chaos (Woodbury, N.Y.) 19 (2009) 041111–1.

[146] J. H. Kim, S. H. Lee 23 (2002) 5–10.

[147] M. Holz, R. Heil, A. Sacco, Phys. Chem. Chem. Phys 2 (2000) 4740–42.

[148] M. a. McCool, a. F. Collings, L. a. Woolf, Journal of The Chemical Society, Faraday Transactions 1 68 (1972) 1489.

[149] K. Yoshida, N. Matubayasi, M. Nakahara, The Journal of chemical physics 129 (2008) 214501.

[150] I.-C. Yeh, G. Hummer, The Journal of Physical Chemistry B 108 (2004) 15873–15879.

[151] C. Zeng, J. Li, D. Wang, T. Chen, C. Zhao, C. Chen, Journal of Chemical & Engineering Data 51 (2006) 93–98.

[152] S. Jeck, P. Scharfer, W. Schabel, M. Kind, Chemical Engineering and Processing 50 (2011) 543–550.

[153] P. Taylor, A. L. Iordanskii, G. E. Zaikov, International Journal of Polymeric Materials and Polymeric Biomaterials 24 (1994) 37–41.

[154] E. Shafee, H. Naguib, Polymer 44 (2003) 1647–1653.

[155] Q. G. Zhang, Q. L. Liu, Z. Y. Jiang, Y. Chen, Journal of Membrane Science 287 (2007) 237–245.

[156] J. Zielinski, J. Duda, Journal of Polymer Science Part B: Polymer Physics 30 (1992) 1081–1088.

[157] F. Pan, F. Peng, L. Lu, J. Wang, Z. Jiang, Chemical Engineering Science 63 (2008) 1072–1080.

[158] A. Gautieri, S. Vesentini, A. Redaelli, Journal of Molecular Modeling 16 (2010) 1845–51.

[159] J. S. Mackie, P. Meares, Proceedings of the Royal Society A: Mathematical, Physical and Engineering Sciences 232 (1955) 498–509.

[160] W. Brown, P. Stilbs, T. Lindström, Journal of Applied Polymer Science 29 (1984) 823–827.

[161] J. S. Vrentas, Journal of Polymer Science: Polymer Physics Edition 15 (1977) 417–439.

[162] J. S. Vrentas, J. L. Duda, Journal of Polymer Science: Polymer Physics Edition 15 (1977) 403–416.

[163] L. I. Costa, G. Storti, Journal of Polymer Science Part B: Polymer Physics 48 (2010) 529–540.

[164] R. H. Lacombe, I. C. Sanchez, The Journal of Physical Chemistry 80 (1976) 2568–2580.

[165] I. C. Sanchez, R. H. Lacombe, The Journal of Physical Chemistry 80 (1976) 2352–2362.

[166] I. C. Sanchez, R. H. Lacombe, Macromolecules 11 (1978) 1145–1156.

[167] A. Noorjahan, P. Choi, Chemical Engineering Science In Press (2014).

[168] J. S. Vrentas, J. L. Duda, H.-C. Ling, A.-C. Hou, Journal of Polymer Science: Polymer Physics Edition 23 (1985) 289–304.

[169] J. S. Vrentas, C.-H. Chu, M. C. Drak, E. V. Meerwal, Journal of Polymer Science: Part B: Polymer Physics 27 (1989) 1179–1184.

[170] N. Ramesh, P. K. Davis, J. M. Zielinski, R. P. Danner, J. L. Duda, Journal of Polymer Science Part B: Polymer Physics 49 (2011) 1629–1644.

[171] P. J. Flory, Journal of Chemical Physics 10 (1942) 51–61.

[172] M. L. Huggins, Journal of American Chemical Society 64 (1942) 1712–1719.

[173] W. H. Jo, K. Choi, Macromolecules 30 (1997) 1800–1805.

[174] Z. wei Li, Z. yuan Lu, Z. yan Sun, Z. sheng Li, L. jia An, Journal of Physical Chemistry B 111 (2007) 5934–5940.

[175] H. Machida, Y. Sato, R. L. Smith, Fluid Phase Equilibria 297 (2010) 205–209.

[176] F. Gonçalves, a.R. Trindade, C. Costa, J. Bernardo, I. Johnson, I. Fonseca, a.G.M. Ferreira, The Journal of Chemical Thermodynamics 42 (2010) 1039–1049.

[177] R. A. Krenz, T. Laursen, R. A. Heidemann, Industrial and Engineering Chemistry Research 48 (2009) 10664–10681.

[178] E. Neau, Fluid Phase Equilibria 203 (2002) 133–140.

[179] R. M. Hodge, Polymer 37 (1996) 1371–1376.

[180] C. a. Grabowski, A. Mukhopadhyay, Macromolecules 41 (2008) 6191–6194.

[181] H. Nikakhtari, L. Vagi, P. Choi, Q. Liu, M. R. Gray, The Canadian Journal of Chemical Engineering 91 (2013) 1153–1160.

[182] M. Osacky, M. Geramian, D. G. Ivey, Q. Liu, T. H. Etsell, Fuel 113 (2013) 148–157.

[183] A. Hooshiar, P. Uhlik, Q. Liu, T. H. Etsell, D. G. Ivey, Fuel Processing Technology 94 (2012) 80–85.

[184] S. Gupta, S. Gittins, P. Picherack, Journal of Canadian Petroleum Technology 44 (2005).

[185] X. Li, L. He, G. Wu, W. Sun, H. Li, H. Sui, Energy & Fuels 26 (2012) 3553–3563.

[186] J. L. Tolton, R. F. Young, W. V. Wismer, P. M. Fedorak, Water Quality Research Journal of Canada 47 (2012) 1–13.

[187] W. Shelfantook, R. Tipman, N. Anderson, C. Strand, in: In CIM, Edmonton, AB.

[188] R. Tipman, Y.-C. Long, W. E. Shelfantook, Solvent process for bitumen separation from oil sands froth, 2001.

[189] D. E. Cormack, J. M. Kenchington, C. R. Phillips, P. J. Leblanc, The Canadian Journal of Chemical Engineering 55 (1977) 572–580.

[190] J. M. Kenchington, C. R. Phillips, Energy Sources 5 (1981) 317–338.

[191] J. Wu, T. Dabros, Energy & Fuels 26 (2012) 1002–1008.

[192] B. C. Fu, C. R. Phillips, Fuel 58 (1979) 557–560.

[193] B. C. H. Fu, C. R. Phillips, Fuel 58 (1979) 554–556.

[194] S. B.D., M. F.W., Fuel Processing Technology 4 (1981) 251–264.

[195] J. S. Tang, P. X. Zhang, The Canadian Journal of Chemical Engineering 78 (2000) 1175–1180.

[196] J. S. Tang, The Canadian Journal of Chemical Engineering 79 (2001) 164–168.

[197] D. Salama, A. Kantzas, in: SPE Annual Technical Conference and Exhibition, 2007, pp. 1–14.

[198] J. Crank, The Mathematics of Diffusion, Oxford University Press, USA, 1980.

[199] M. B. Satterfield, J. B. Benziger, The journal of physical chemistry. B 112 (2008) 3693–704.

[200] a. Dobreva, I. Gutzow, J. Schmelzer, Journal of Non-Crystalline Solids 209 (1997) 257–263.

[201] P. W. Majsztrik, M. B. Satterfield, A. B. Bocarsly, J. B. Benziger, Journal of Membrane Science 301 (2007) 93–106.

[202] Y. Zhang, T. Takanohashi, S. Sato, I. Saito, Energy & Fuels 18 (2004) 283–284.

[203] H.-S. Liu, Y.-C. Wang, W.-Y. Chen, Colloids and Surfaces B: Biointerfaces 5 (1995) 25–34.

[204] J. S. Vrentas, J. L. Duda, A. Hou, Journal of Applied Polymer Science 29 (1984) 399–406.

[205] O. Rodrguez, F. Fornasiero, A. Arce, C. J. Radke, J. M. Prausnitz, Polymer 44 (2003) 6323–6333.

[206] L. A. James, M. A. Ioannidis, I. Chatzis, Energy & Fuels 26 (2012) 6200–6209.

[207] A. Sadighian, M. Becerra, A. Bazyleva, J. M. Shaw, Energy & Fuels 25 (2011) 782–790.

[208] X. Zhang, M. Fulem, J. M. Shaw, Journal of Chemical & Engineering Data 52 (2007) 691–694.

[209] X. Zhang, J. M. Shaw, Petroleum Science and Technology 25 (2007) 773–790.

[210] H. Fadaei, J. M. Shaw, D. Sinton, Energy & Fuels 27 (2013) 2042–2048.

[211] H. Luo, A. Kantzas, Journal of Canadian Petroleum Technology 143 (2011) 24–34.

[212] B. Afsahi, A. Kantzas, PETROLEUM SOCIETY 130 (2006) 1–10.

[213] T. M. Maria, R. a. de Carvalho, P. J. Sobral, A. M. B. Habitante, J. Solorza-Feria, Journal of Food Engineering 87 (2008) 191–199.

[214] D. Green, R. Perry, Perry's Chemical Engineers' Handbook, Eighth Edition, McGraw-Hill Professional, 2007.

[215] Y. Tamai, H. Tanaka, Chemical Physics Letter 285 (1998) 127–132.

[216] R. D. Goodwin, BenzeneThermophysical Properties from 279 to 900 K at pressures to 1000 Bar, 1988.

[217] J. R. Fried, Polymer Science and Technology, Prentice Hall, 2ed edition, 2003.

[218] J. Swenson, J. Teixeira, The Journal of chemical physics 132 (2010) 014508.

[219] Y. Xia, G. Dosseh, D. Morineau, C. Alba-Simionesco, The journal of physical chemistry. B 110 (2006) 19735–44.

[220] R. M. Hodge, T. J. Bastow, G. H. Edward, G. P. Simon, A. J. Hill 9297 (1996) 8137–8143.

[221] B. Hess, H. Bekker, H. J. C. Berendsen, J. G. E. M. Fraaije, Journal of computational chemistry 18 (1997) 1463–1472.

Appendix A

Self diffusion coefficient

Regardless of the arrangement in the space, all molecules have some kinetic energy or thermal motion. In the case of solids, this energy is more in the form of vibration of bonds. But in the case of liquids and gases, it is dominated by translational motion. This translational motion or thermal motion naturally causes the molecule to move more or less like a random walker. Although in a system with uniform distribution the average of this random motion is zero, its mean square displacment is not vanishing. The mean square displacement of the random walker is a measure of its mobility in the system and theoretically is proportional to its self-diffusion coefficient. The important point here is to distinguish the term self-diffusion which is totally different from mutual diffusion coefficient in the sense of Ficks first law. Unlike the Fickian diffusion coefficient, which is defined for systems with at least two components with some non-uniformity in the concentration, the self-diffusion is a measure of mobility of the molecules in the system due to the thermal motions and can be evaluated even in single component systems. This diffusion coefficient is also called the tracer diffusion coefficient. Tracer diffusion coefficient can be measured for molecule A in a system of A molecules (which is self-diffusion of A) or in a system of B molecule (which is the self-diffusion of A in B). Although the term self-diffusion has been defined for one component systems, but it is usual to use this term to point to the mobility of molecules in different environment.

Appendix B

Assigned OPLS-AA atom types to PVA monomer

In the Figure B.1 the atom type assignment used in our simulations is presented.

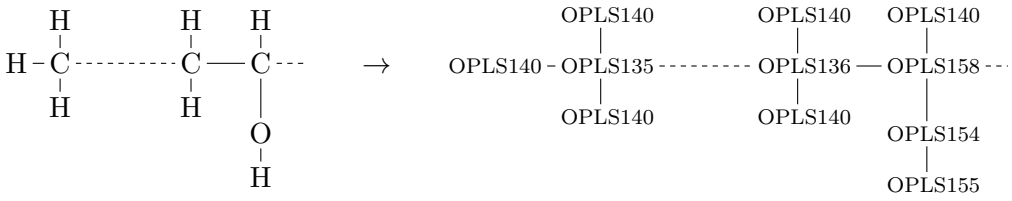

Figure B.1: Mapping of the PVA monomer and end methyl group to the OPLS-AA force field atom type.

Appendix C

Effect of degree of hydrolysis on Hildebrand solubility parameter

Before calculating HS parameter for PVA with different degree of hydrolysis, we have checked the density of these systems in figure C.1 to confirm if there is any inconsistency. As we expected, by decreasing degree of hydrolysis the density of the system decreases as density of pure PVA and PVAc at 300 K is around 1280-1310 and 1190 kg/m^3 respectively. The calculated T_g for these systems using data in figure C.1 is in good agreement with previously reported value of 320-340 K for PVA with degree of hydrolysis of 88-95% [88, 213].

Figure C.2 shows the effect of hydrolysis on the solubility parameter of the PVA. As you can see, by adding more hydrophobic acetate groups, the solubility parameter departs more from those of water.

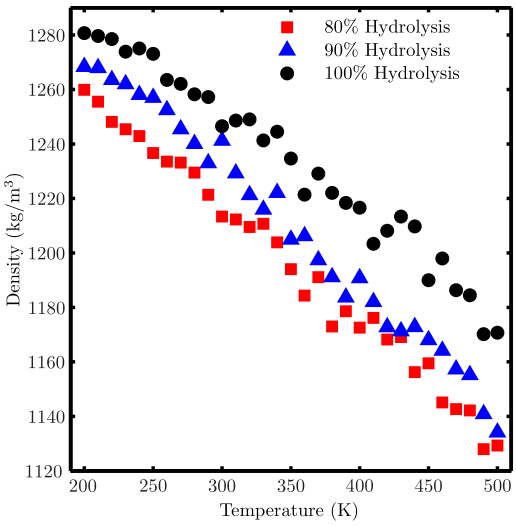

Figure C.1: Density of atactic PVA with different degree of hydrolysis and temperatures.

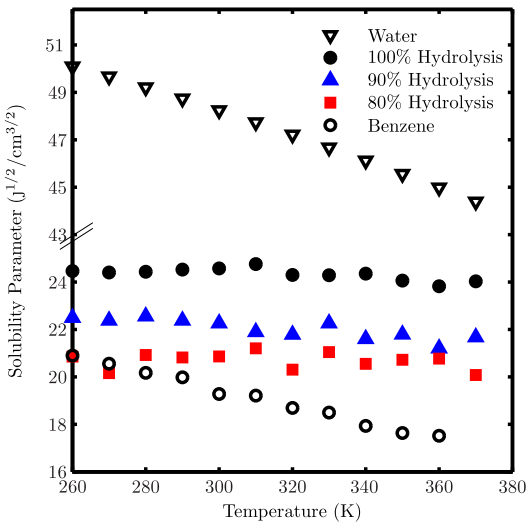

Figure C.2: Hildebrand solubility parameter of PVA with different degree of hydrolysis compared to those of water and benzene at different temperatures.

Appendix D

Density and glass transition temperature of PVA/solvent systems

D.1 Density

Calculated volumetric properties are mostly used to show both applicability of the applied force field and also it can provide useful information regarding other properties of the system like glass transition. Accordingly, in figure D.1 we have compared calculated density for systems with 1 and 20 wt% water at different temperatures with experimental density of the same systems calculated with inverse rule of mixture having the experimental density of pure PVA [74] and water [214] at different temperatures. As we expected, the density of higher water content system is in good agreement with experimental data while deviation is slightly higher for low water content systems owing to its slower relaxation. Also note that the experimental density reported for PVA[74] corresponds to PVA with some degree of crystallinity and serve as an upper limit as such crystalline phase does not exist in system considered here. Nonetheless, calculated densities indicate the deviation from expected experimental values (for PVA/water) is less than 3% at most (for low water content systems). This result, and agreement with other MD data reported indicates that the forcefield selected can describe the PVA/water system adequately. It is also worth noting that for systems with lower water content in some temperatures the density of the system has been increased to a value bigger than density of pure PVA (reported in our previous work [119]) which also has been observed experimentally [5]. Comparing to our results, densities reported by Wu [63] for system with 21 wt% water are smaller due to difference in preparation method of the samples and the smaller chain's length used in Wu's study (although the force field used for water and PVA are identical). Also Tamai et al. [215],

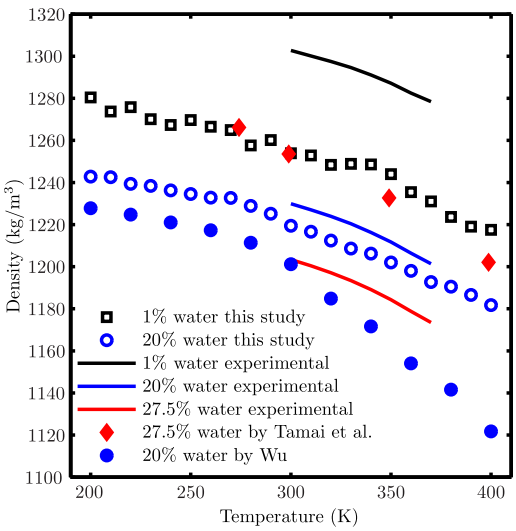

Figure D.1: Density of PVA/water mixture at different compositions and temperatures. Calculated densities are average over last 50 ns of production simulations.

using TIP4P model for water, and OPLS/united-atom for PVA has reported the density of system with 27.5 wt% water as function of temperature. The data by Tamai et al., shown in figure D.1, over estimates the density as it was expected (They applied united atom force field where less geometrical obstacles due to absence of explicit hydrogens in the system allows monomers' center of mass to pose a more compact structure respect to our system. This fact is also obvious in the water self diffusion coefficient data reported in their study).

In figure D.2 density of PVA/water systems with water contents up to 20 wt% has been shown. As you can see, the density of systems with 1 and 3 wt% water show a great deal of fluctuation as relaxation in these systems is relatively harder to achieve. In systems with higher water content (5-20 wt%) these fluctuations are significantly smaller as relaxation is achieved much faster due to plasticization effect of water.

In figure D.3 we have compared the calculated density for PVA/benzene systems with different benzene concentrations and temperatures with experimental data obtained by pure components' density (density of benzene from [216]) and inverse rule of mixture (which may not be applicable to this system as PVA and benzene are not miscible). Trend of deviation of calculated values from experimental data is similar to the case of PVA/water with slightly higher magnitude.

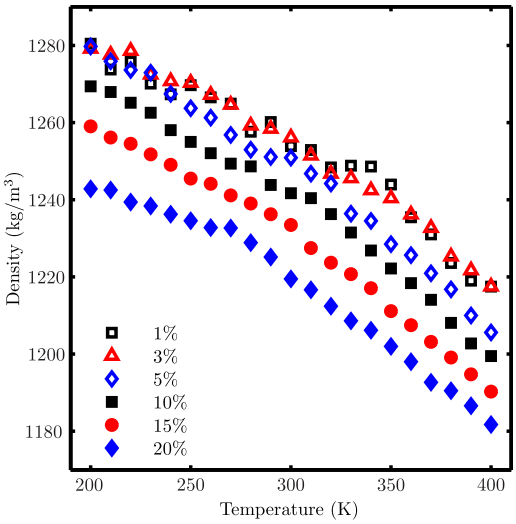

Figure D.2: Density of PVA/water mixture at different water contents and temperatures.

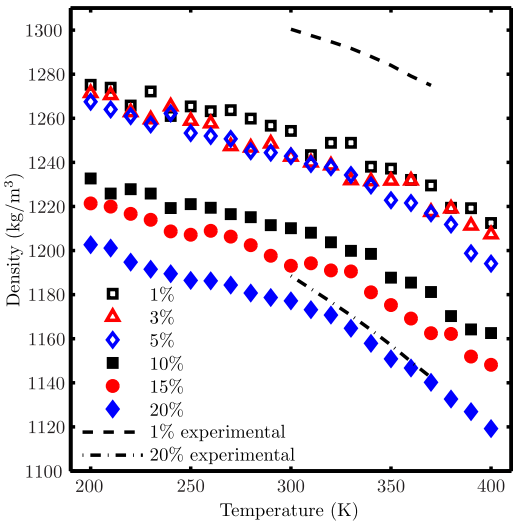

Figure D.3: Density of PVA/benzene mixture at different benzene contents and temperatures.

D.2 Glass Transition Temperature

Using the calculated density in previous section and applying the same method as we explained in our previous work [119], the glass transition temperature (T_g) of the PVA/solvent mixtures has been calculated at different concentrations. Great agreement between calculated and experimental values of T_g shown in figure D.4 confirms the accuracy of the force field and simulation protocol used for the simulations. Also Wu [63] reported the T_g for system containing 21 wt% water to be around 283 K which is in agreement with our value of 272 K for system containing 20 wt% water.

There are several models to predict the T_g of a binary mixture having the T_g of pure components. These models summarized in equations D.1-D.4 (for complete discussion see [217]):

$$T_g = w_1 T_{g1} + w_2 T_{g2} \tag{D.1}$$

$$ln\,(T_g/T_{g1}\,) = \frac{w_2 ln\,(T_{g2}/T_{g1}\,)}{w_1\ T_{g2}/T_{g1} + w_2} \tag{D.2}$$

$$1/T_g\ =\ w_1/T_{g1}\ +\ w_2/T_{g2} \tag{D.3}$$

$$lnT_g = w_1 lnT_{g1} + w_2 lnT_{g2} \tag{D.4}$$

The values used for T_g in these equations are 136[218], 170[219] and 350[119] K for water, benzene and PVA respectively. In figure D.4 we have compared the calculated T_g of PVA/water systems with predictions of equations D.1-D.4. As results indicate, the classical thermodynamic model (Eq. D.2) can describe the behavior of PVA/water system very well. At low water content systems T_g shows some deviation from classical thermodynamic model but as water content increases the T_g of mixture gets closer to prediction by this model. The deviation at lower water content can be attributed to incomplete relaxation of the system due to limited simulation time. In agreement with findings of Rault et al. [88], our data indicate that T_g of PVA/water system follows prediction by Fox equation (Eq. D.3).

AS benzene is not capable to plasticize PVA as it doesn't affect the hydrogen bonding network of PVA significantly, there is no significant decrease in T_g by adding benzene which is confirmed by data in figure D.5. Note that possibility of clustering of benzene molecules has been ruled out as radial distribution function of the benzene does not confirm that (data not shown). Unfortunately as PVA and benzene are not miscible there is no experimental data on their T_G. Also it is interesting that calculated values does follow any of the mentioned equations D.1-D.4.

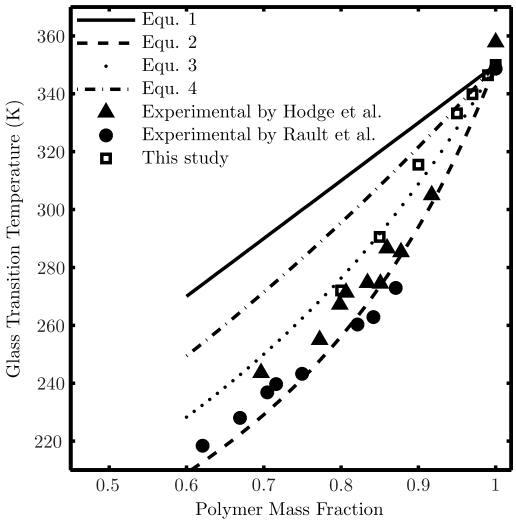

Figure D.4: Tg of PVA/water mixture at different compositions. For experimental data Rault and Hodge see [88, 220].

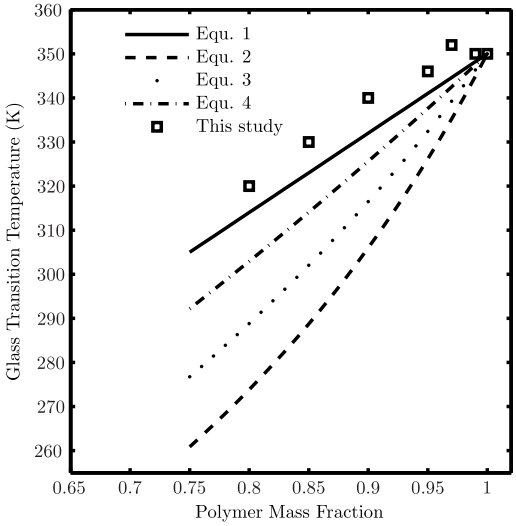

Figure D.5: Tg of PVA/benzene mixture at different compositions.

Appendix E

Sensitivity analysis on simulation of PVA melt

E.1 Simulation step time

The previous MD simulation on the PVA chain mostly used the united atom force field developed especially for PVA and as there is no high frequency degree of freedoms like bound involving hydrogen atoms using large simulation time step as high as (2fs) was possible. But Wu [63] has used an all atom force field, OPLS-AA, with time step of 1 fs without any comment on how this can affect the system. Although the using higher time step is computationally favorable, but we suspect that such large time step (beyond its effect on stability of the integrator) can affect the properties of the system especially those which are affected by hydrogen bonds in the system. Irregularity in number of hydrogen bonds and their mean life time in can directly affect properties like solubility parameter.

To check if there should be any concern with this regard we have simulated all 10 DP50 chains in two different time step of 0.5 and 0.1 fs. Doing this, simulation results indicates that energy of the system has been decreased as we expected due to more stable hydrogen atoms in the system. This energy reduction is more pronounced in the bonds energy in the system (which are not affecting the solubility parameter). Results for the solubility parameter of lower time step systems indicate that better estimation can be obtained with lower time step. This results all indicates that having explicit hydrogen atoms in the system requires reduction of the time step. But reducing the time step can increase the computation cost dramatically. As united atom force field is not an option, as explicit hydrogen atoms are required to capture true hydrogen bonding in the system, there will be two other options left. First option is doing simulations with time step of 1 fs and after

reaching close to equilibrium, continuing the simulation with time step of 0.1 fs for enough length of time. Obviously this method only works for static properties calculation as they mostly need short equilibrium trajectories. The second option is constraining all H atoms in their equilibrium bond length using an appropriate method like LINKS [221]. Applying this constrain, we repeated all simulations and results shows constraining hydrogen atoms cause a slightly under estimation of the density (less than 0.5%) and solubility parameter (less than 2.8%).

E.2 Atomic partial charge distribution

It has been reported that there was a problem using OPLS-AA original partial atomic charges for simulation of the PVA by Wu [63] and partial atomic charges of COMPASS force field has been used but we didn't find any problem using the original OPLS-AA charges. In other hand it has been numerously stressed in the literature that interchanging parameters between force fields with different philosophy is not recommended. To clarify that any difference between our results and those reported by Wu [63] is not due to this difference we have simulated all DP50 chains at 300 K. Comparing the results with our results using original OPLS-AA partial charges, both set of charges resulted in a same average value for density and solubility parameter with slightly more fluctuation in the system properties in the case of COMPASS charges. Also it came to our attention that using COMPASS charges there was a 10% reduction in number of hydrogen bonds in the system.

E.3 Effect of anisotropic box

Muller-Plathe et. al. [3] mentioned that they have used anisotropic pressure coupling to account for contribution to the atomic virial by the bond angle and dihedral angle terms, which will be canceled out only for the isotropic pressure coupling. Accordingly we have simulated all DP50 chains with anisotropic pressure coupling and found that there is a insignificant difference between the densities calculated in which anisotropic systems had smaller density values. Also systems with anisotropic pressure coupling poses slightly higher potential energy. Further investigation showed that systems with anisotropic pressure coupling have lower bond energy and higher angle energy. Beside these minor effects, the most important problem with anisotropic pressure coupling is the distortion of the cell which may

cause significant reduction in cell size in one dimension. In some cases it happened that the box size decreased so much that the simulation failed due to violation of the minimum image convention.

Appendix F

PAC Calculation

Table F.1 shows the deviation of average PACs calculated in the solvated state using different methods relative to the same PACs calculated in vacuum for optimized structures. As can be seen, the sensitivity of the AIM results to solvent is quiet high relative to other methods.

Table F.1: Percentage of relative changes in calculated PACs in the solvated state relative to those of optimized geometries in vacuum.

	MPA	NPA	MSK	AIM	Hirshfeld
Water	10	15	39	130	10
Ethanol	9	14	37	123	9
Benzene	10	15	39	130	10

Figure F.1 compares the dihedral angle distributions for different PAC sets. As we expected, the quality of results are in accordance with calculated densities.

Table F.2 shows the standard deviation of the PACs reported in table 6.1.

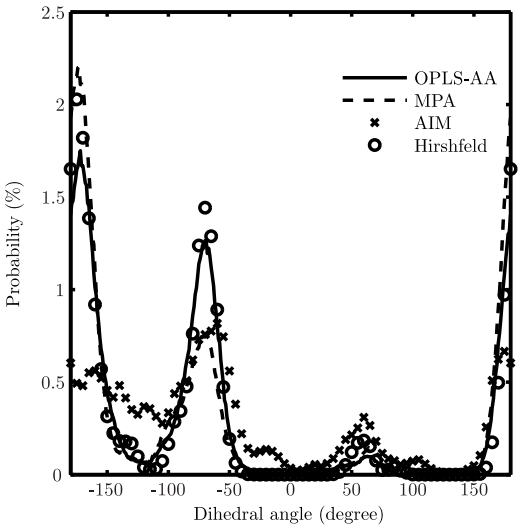

Figure F.1: Comparison of back-bone carbon atoms dihedral angle distribution of an isotactic PVA chain with 400 monomers calculated with different PAC sets. Results were averaged over all possible dihedral angles in a 5 ns simulation on a well relaxed chain in a NPT ensemble at 300 K and 1 bar. Note that the density of the data has been reduced for better resolution.

Table F.2: Standard error (%) for calculated PACs.

Atom	MPA	NPA	MSK	AIM	Hirshfeld
H[a]	0.92	0.33	1.42	1.16	0.37
H[a]	0.94	0.35	1.43	1.24	0.39
H[a]	1.04	0.38	1.50	1.26	0.43
C[a]	1.19	0.15	4.54	1.07	0.13
H[b]	1.46	0.50	3.60	1.56	0.56
C1	1.90	0.67	15.07	1.41	0.45
H[b]	1.56	0.51	3.81	1.66	0.55
C2[c]	1.62	0.36	8.84	5.55	0.21
H	1.87	0.68	3.52	1.95	0.83
O	2.31	0.97	4.06	4.55	2.28
H[d]	2.13	0.38	2.31	2.36	0.97
H[e]	1.25	0.42	1.34	1.30	0.46
H[e]	1.22	0.38	1.42	1.16	0.42
H[e]	1.14	0.37	1.25	1.18	0.41
C[e]	1.14	0.27	2.88	1.13	0.27

[a] Starting methyl group-Carbon connected to C1
[b] Connected to C1
[c] Connected to O
[d] Connected to O
[e] End methyl group-Carbon connected to C2

Appendix G

Free energy of solvation

Figure G.1 shows an example of Hamiltonian change as the lambda changes in the slow-growth method. We are aware of the fact that by increasing the number of points we are able to obtain smoother curves (especially when vdW interactions start to vanish), but our results indicate that change in the final calculated FES would be minor.

Figure G.2 shows the probability distribution for the ab initio calculated FES for oligomers of PVA in different solvents. As can be seen, these values are highly conformation dependent and are slightly different for different tacticities.

Table G.1 compares the ab initio calculated FES as averaged by the Boltzmann factor with regular averaged values.

Table G.1: Average values for ab initio calculated FES.

	Boltzmann weighted			Regular		
	Ata	Iso	Syn	Ata	Iso	Syn
Water	-158.3	-155.9	-148.0	-169.6	-163.0	-164.3
Ethanol	-149.5	-147.9	-138.3	-160.9	-154.8	-156.0
Benzene	-63.1	-63.9	-56.9	-70.8	-68.6	-68.8

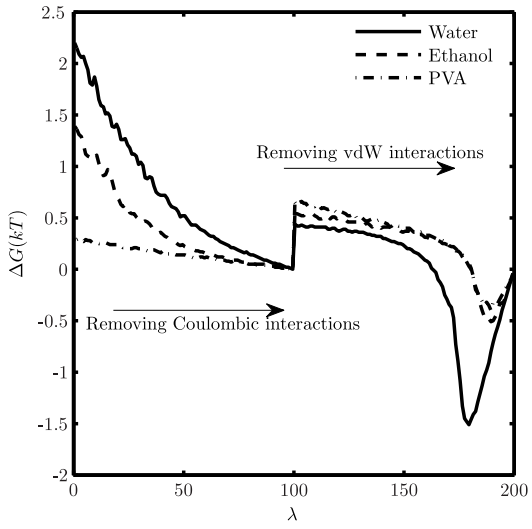

Figure G.1: A typical graph of changes in free energy during the slow-growth method. Data is related to solvation of one of the isotactic PVA oligomers.

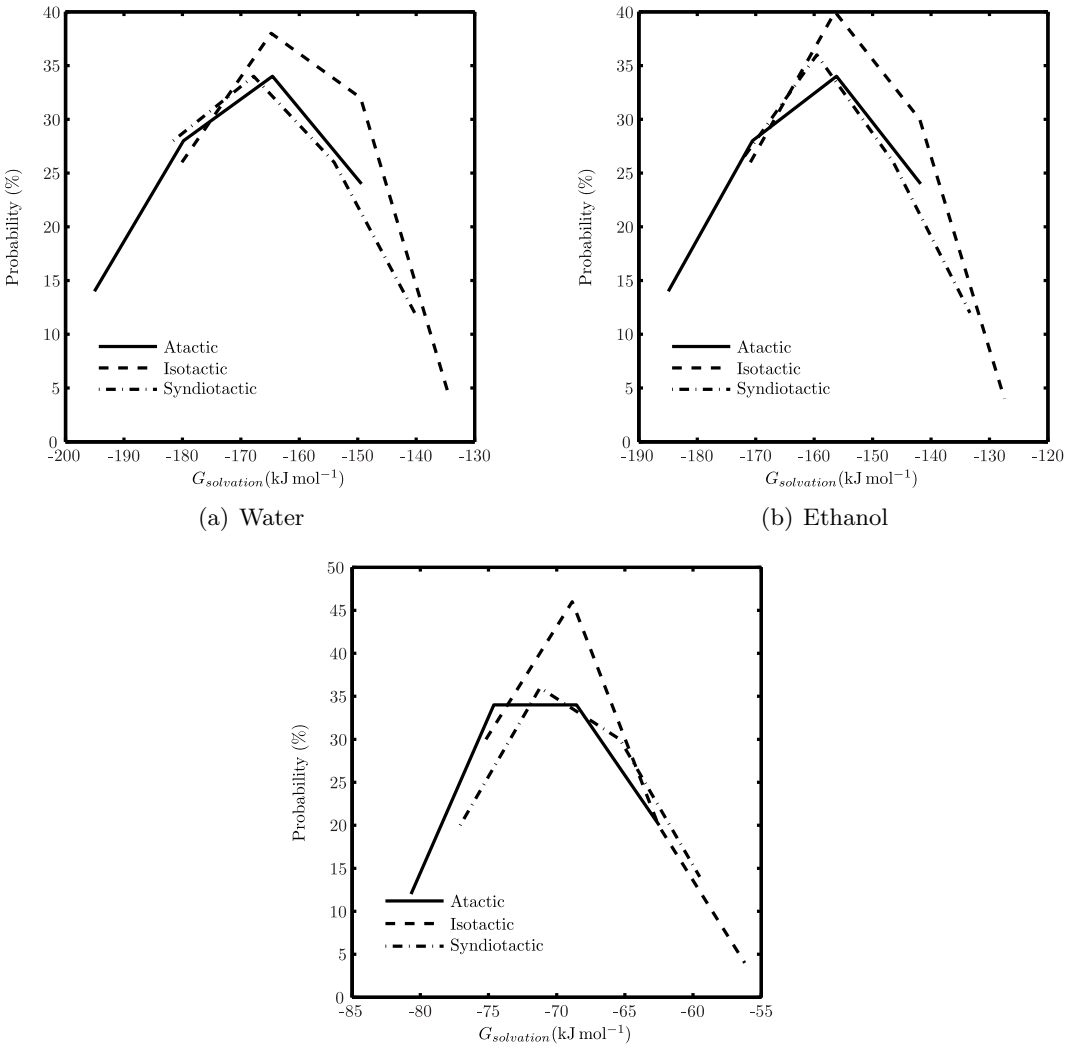

(a) Water

(b) Ethanol

(c) Benzene

Figure G.2: Probability distribution of ab initio calculated free energy of solvation.

Appendix H

Solvents self diffusion data

Table H.1: Calculated self-diffusion coefficients of water in the PVA/water system. Numbers multiplied by 10^{12}.

		T (K)										
		270	280	290	300	310	320	330	340	350	360	370
	1	0.03	0.05	0.06	0.10	0.12	0.17	0.26	0.29	0.69	1.26	1.45
	3	0.07	0.10	0.24	0.34	0.46	0.69	0.74	1.18	1.30	1.70	2.87
wt%	5	0.15	0.17	0.27	0.51	0.81	0.95	1.08	1.47	1.53	2.41	5.17
	10	0.36	0.56	0.93	1.11	1.70	2.41	3.03	3.63	4.75	7.10	8.41
	15	0.68	0.88	1.14	1.65	2.60	5.26	9.30	11.40	20.98	26.00	59.12
	20	2.14	2.95	5.19	7.95	10.62	22.09	39.43	46.00	57.00	62.00	214.16

Table H.2: Calculated self-diffusion coefficient of benzenes in the PVA/benzene system. Numbers multiplied by 10^{14}.

		T (K)										
		270	280	290	300	310	320	330	340	350	360	370
	1	0.07	8.88	5.70	0.74	16.04	3.18	15.77	33.65	10.97	18.30	17.71
	3	28.57	28.79	26.90	36.90	32.67	27.61	58.38	103.98	50.99	16.04	15.35
wt%	5	27.55	27.19	28.82	19.86	33.19	38.61	41.47	159.94	72.05	52.04	12.60
	10	56.74	53.98	55.35	75.06	93.58	114.71	141.29	504.57	311.80	96.23	92.71
	15	18.12	36.00	52.13	91.95	151.59	255.51	393.21	1312.38	843.41	308.20	296.27
	20	81.29	107.13	154.60	267.36	429.08	682.42	1005.31	2732.95	2051.37	926.90	891.06

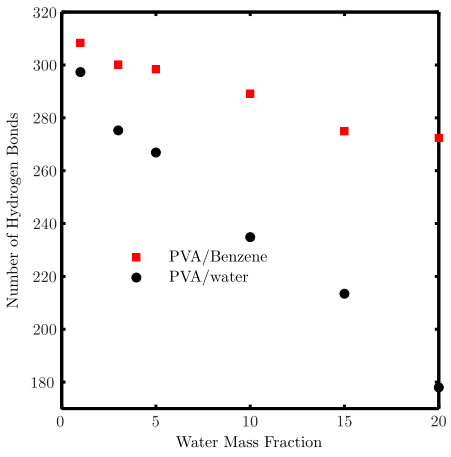

Figure H.1: Numbers of hydrogen bonds between PVA segments at different concentrations of water and benzene at 300 K. The averages were obtained from the last 5 ns of the production simulation runs.

Appendix I

Derivation of the characteristic parameters of the SLEOS

I.1 Typical graphs for derivation of the characteristic parameters of the SLEOS

Typical derivations of physical parameters obtained from the SLEOS from MD simulation are shown in figure I.1.

I.2 Quality of the prediction by SLEOS

Figure I.2 shows the experimental data used for the parametrization of SLEOS for ethanol. As can be seen, after fitting, the parameters are capable of predicting the density with great accuracy. Figure I.3 shows the experimental data used for parametrization of SLEOS for PVA. It is evident that after fitting, the parameters are capable of predicting the density with great accuracy.

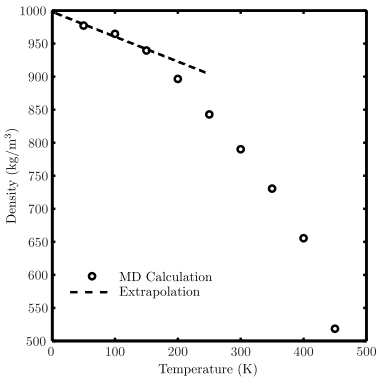

(a) ρ^* for water. The extrapolation line indicates the ρ^* at 0 K.

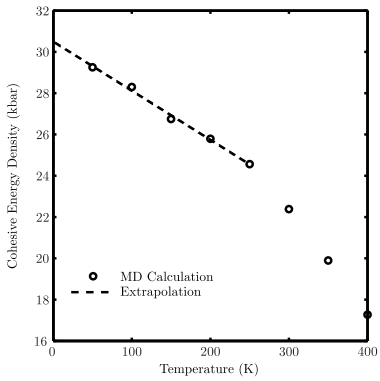

(b) P^* for ethanol. The extrapolation line indicates the P^* at 0 K.

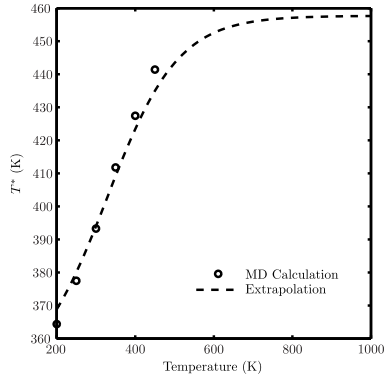

(c) T^* for benzene. The extrapolation line indicates the P^* at 0 K.

Figure I.1:

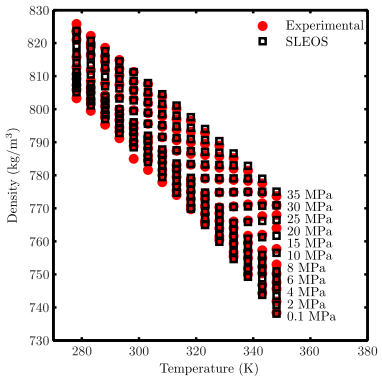

Figure I.2: Results of the fitting of the SLEOS to the ethanol experimental densities.

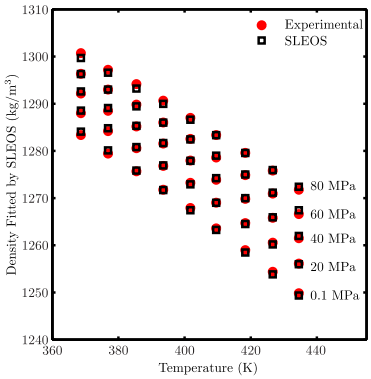

Figure I.3: Results of the fitting of the SLEOS to the PVA experimental densities.